Preparation of Novel Nanometer-Dispersed Semicrystalline/Amorphous Polymer Composites using Supercritical Carbon Dioxide

（超臨界二酸化炭素を用いた新規半結晶性/非晶性高分子ナノコンポジットの調製）

January 2014

Materials and Applied Chemistry Major
Graduate School of Science and Technology
Doctoral Course
Nihon University

Rui Zhu

Referee in chief:	Professor	Dr. Takashi Sawaguchi
Referee:	Professor	Dr. Hiizu Iwamura
	Professor	Dr. Masahiro Kakugo
	Professor	Dr. Shigeru Shimizu

Table of Contents

Acknowledgment

Chapter 1

General Introduction

Table of Contents

Chapter 1

General Introduction

1.1 Conventional preparation methods of polymer composites

The blending of two or more polymers with different characteristics is one of the most important techniques used to prepare new materials with novel features not found in any current constituent polymer. Preparation of polymer composite can be accomplished by:

(1) mechanical mixing

(2) dissolution in co-solvent followed by film casting, freeze or spray drying

(3) latex blending

(4) fine powders mixing

(5) use of monomer(s) as solvent for another blend component followed by polymerization as in interpenetrating polymer networks (IPNs), manufacture

(6) various other methods of IPN technology

In general, the miscibility of different polymers is so limited that conventional methods such as melt processing or casting from solution have been successfully employed only in a few cases, e.g., the polystyrene (PS)/poly(vinyl methyl ether) blend [1]. Especially, nanometer dispersed semicrystalline/amorphous polymer composites cannot be blended using conventional methods because the amorphous polymer is excluded from the crystalline regions during the crystal growth process [2].

1.2 Preparation of polymer composites using supercritical carbon dioxide

Supercritical carbon dioxide ($scCO_2$) is a fluid state of carbon dioxide where it is held at or above its critical temperature and critical pressure. Carbon dioxide usually behaves as a gas in air at standard temperature and pressure (STP), or as a solid called dry ice when frozen. If the temperature and pressure are both increased from STP to be at or above the critical point for carbon dioxide, it can adopt properties midway between a gas and a liquid. More specifically, it behaves as a supercritical fluid above its critical temperature (31.1 ºC) and critical pressure (7.38 MPa), expanding to fill its container like a gas but with a density like that of a liquid.

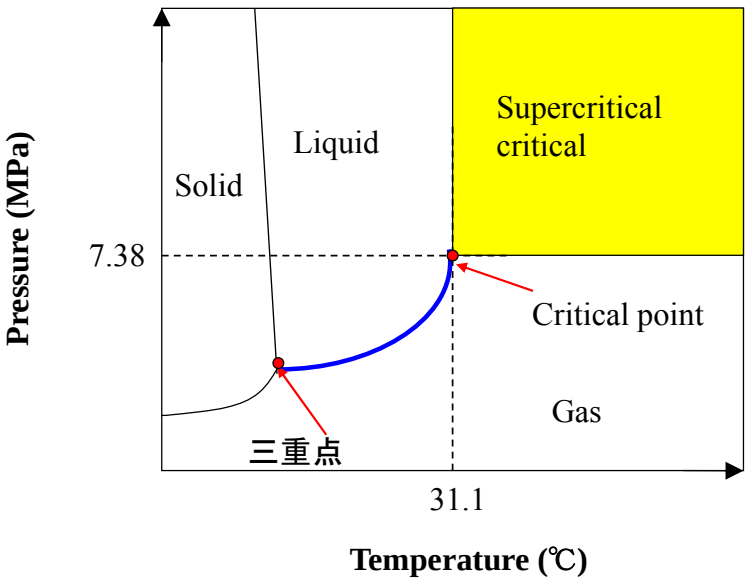

Figure 1-1 Carbon dioxide pressure-temperature phase diagram.

$ScCO_2$ is a good solvent for many small molecules [3], and although it is a good swelling agent for most polymers, it is a very poor solvent for them, even at extremely high pressure [4]. The density of supercritical fluids (SCFs) and thus their solvent strength is continuously tunable from gas-like to liquid-like by changing pressure and temperature. This provides them with the ability to control the degree of polymer swelling as well as the partitioning of small molecule penetrates between the swollen polymer phase and the fluid phase [5,6]. The low viscosity and near-zero surface tension of SCFs allow for fast mass transfer of penetrates into a swollen polymer. $ScCO_2$ has been used to impregnate polymers with different additives [7] and because CO_2 is a gas at ambient conditions, the removal and recovery of the solvent from final product are extremely easy.

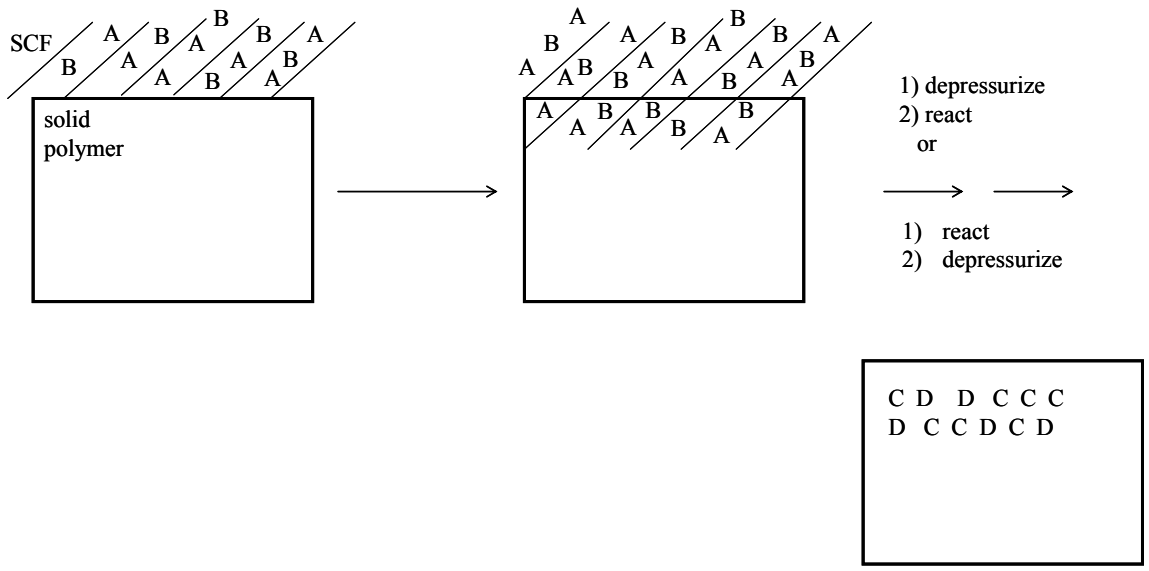

Figure 1-2 Diagram of polymer composite preparation using $scCO_2$.

A synthetic method for producing new polymer composites using supercritical carbon dioxide ($scCO_2$) has been developed by Watkins and McCarthy [8]. The general objective of this program is summarized in figure 1-1; reagents (A and B) are infused into a solid polymer as a SCFs solution where they are induced to react and form products (C and D). The reaction can be run either in the presence of the SCFs solution or subsequent to removal of the solution by depressurization.

1.3 Current situation of polymer composites using supercritical carbon dioxide

A series of new polymer composites have been prepared using $scCO_2$ since Watkins and McCarthy developed the method [8]. These new composites are showed in table 1-1. Here, some representative examples are introduced. PS composites of semicrystalline and glassy polymer substrates such as polyethylene (PE), bisphenol-A polycarbonate, poly(oxymethylene), nylon 66, poly(4-methyl-l-pentene), and poly(chlorotrifluoroethylene) w ere also successfully synthesized [8-10]. Kung *et al*. reported that mechanical properties such as Young's modulus and the yield stress of high-density polyethylene (HDPE)/PS composites obtained using $scCO_2$ could be controlled by composition [11]. In addition, they showed that the mechanical properties of the HDPE/PS composite prepared by using $scCO_2$ were superior to a HDPE/PS blend prepared by means of the conventional melt-mixing process. Ultra-high-molecular-weight polyethylene (UHMWPE)/methacrylate polymer composites prepared with various hydrophobic methacrylate monomers featuring alkyl side chains of varying lengths in place of the styrene and the controlled preparation of copolymer blends of alky methacrylates within a UHMWPE substrate have also been reported [12-14]. UHMWPE was also blended with biodegradable polymers – polycaprolactone (PCL) successfully [15]. Moreover, semi-interpenetrating polymer networks (IPNs) of UHMWPE with PMMA-co-poly(ethylene glycol) dimethacrylate (PEGDMA) were prepared through $scCO_2$

Table 1-1 Polymer composites prepared using $scCO_2$

Polymer Composite	Processing Conditions	Analytical Techniques	Reference
HDPE/PS	4h, 10MPa, 40℃	DSC, Mass difference, FTIR, TEM	8,11,19,20
PCTFE/PS	4h, 24MPa, 40℃	DSC, FTIR, TEM	8,21,11,19,20
		Mass difference	
		energy dispersive X-ray	
PS/PVME (poly(vinyl methyl ether))	0-35MPa, 0-200℃	SANS	22
PE/PVAc	0.5h, 6MPa, 80℃	ATR-FTIR, XPS, DMA	17
		Protein Adsorption test	
PVC/PS	12h, 12MPa, 35℃	SEM, DSC, DMA	23
UHMWPE/PMMA	16h, 21MPa, 120℃	DSC, TMAFM	12
PP/PS	14h, 10-20MPa, 120℃	TEM, DSC, DMA,	9
		Universal Tensile Tester	
LDPE/PS	24h, 9-16MPa, 35℃	SEM, Universal Tensile Tester	24
PS/PET	—	—	21
PS/PC	160℃	DSC, CP/MAS, NMR, WAXD	25
		Gravimetric sorption apparatus	
PVP/PEG	4MPa(0-5h), 80MPa(0-0.5h), 35℃	ATR-FTIR	26

facilitated impregnation of (methyl methacrylate) MMA and ethylene glycol dimethacrylate (EGDMA) monomers into UHMWPE [16]. The mechanical properties of polymer composites prepared using the $scCO_2$ method can be controlled by using a combination of the substrate and monomer.

The author's laboratory have already succeeded in obtaining micro-phase-separated polymer composites of polyethylene (PE)/poly(vinyl acetate) (PVAc) and syndiotactic polystyrene (sPS)/poly(methyl methacrylate) (PMMA), even though they are immiscible and thus could not have been obtained using conventional methods [17,18]. The PE/PVAc composite features a biocompatible surface and could be used to fabricate medical devices. The sPS/PMMA composite was blended at the nanometer level, and thus, favorable mechanical properties are expected.

1.4 Scope of the research

There are two purposes in this research work:

1. Preparation of novel nanocomposites that can not be obtained using conventional methods.

2. Control of the bulk and surface properties of these nanocomposites.

To achieve these purposes, firstly, polypropylene (PP) and PE that are the most used polyolefin were selected as polymer substrates. Next is the selection of appropriate monomer. The monomer should meet three conditions below:

a. It can be dissolved in $scCO_2$.

b. Corresponding polymer can not be dissolved in $scCO_2$.

c. Corresponding polymer possesses different properties comparing with the polymer substrate.

According to these three conditions, MMA and octamethylcyclotetrasiloxane (D4) were selected as monomers. MMA and D4 can be easily dissolved in $scCO_2$. Corresponding polymers PMMA and polydimethylsiloxane (PDMS) can not be dissolved in $scCO_2$ in this study, although PDMS is considered as one of polymers that are the most easily dissolved in $scCO_2$. PMMA is an amorphous polymer having high optical properties, good chemical resistance, and high tensile strength. PDMS is an inorganic polymer possessing excellent

thermal stability, dielectric properties, and excellent flame retardant. It is also widely known owing to its extremely low glass transition temperature, flexibility and their hydrophobic surface properties [27-30]. PMMA and PDMS possess different properties comparing with polyolefin substrates, and new materials with novel features are expected by blending polyolefin substrates with PMMA or PDMS.

Three kinds of novel polymer nanocomposites (iPP/PMMA, LLDPE/PMMA, LLDPE/PDMS) were prepared using the above-mentioned methods. And then, the connection between constituent content of polymer composites and process parameters such as initial pressure, polymerization time, and soaking temperature was studied, which would allow the control of bulk and surface properties.

Chapter 2 introduces the preparative methods of polymer composites and instrumental analyses used in this study.

In **Chapter 3,** the composites comprising iPP and PMMA were prepared using $scCO_2$. The preparation, microstructure, crystallinity, and thermodynamic and mechanical properties of the iPP/PMMA composites are reported in detail. The microstructure of the iPP/PMMA composites was investigated using transmission electron microscopy (TEM), atomic force microscopy (AFM), and small-angle X-ray scattering (SAXS), and these measurements yielded consistent results. iPP and PMMA were blended at the nanometer level through the supercritical impregnation of a methyl methacrylate (MMA) monomer and an initiator into

the amorphous interlamellar regions of a iPP substrate, followed by *in situ* polymerization of the MMA monomers. The results of wide-angle X-ray diffraction (WXRD) and differential scanning calorimetry (DSC) showed that PMMA did not affect the crystallinity, the enthalpy of melting the iPP crystal, nor the top temperature of the iPP crystal melting, but it did reduce the starting temperature at which the iPP crystal melting. The dynamic viscoelastic analysis (DVA) and tensile tests were used to measure the mechanical properties of the composite including storage modulus, yield stress, fracture stress and strain. It was determined that these properties depended on the composition of the composite and are dependent on the initial pressure of CO_2. The DVA results also showed that the iPP and PMMA were somewhat thermodynamically miscible.

Chapter 4 demonstrates the thermal stabilities of iPP/PMMA composites. The microstructure was investigated using SAXS and TEM. The crystallinity was analyzed by DSC and WXRD. The mechanical properties were evaluated by DVA. When the iPP/PMMA composites were annealed at 140 °C, although the iPP crystal grew, the nano-structure can be remained. When the iPP/PMMA composites were annealed at 190 °C, PMMA migrated by diffusion from the amorphous region of iPP, then macroscopic domain structure was formed, and the nanostructure cannot be remained.

Chapter 5 demonstrates the preparation of nanometer dispersed LLDPE/PMMA polymer pseudo-interpenetrating networks (pseudo-IPNs) using $scCO_2$. These pseudo-IPNs were

formed by the complicated entanglement of the amorphous chain of LLDPE and PMMA chains through controlling the mass gain of PMMA. SAXS measurement showed that LLDPE and PMMA were blended at the nanometer level. The thermodynamic miscibility and thermal stability of pseudo-IPNs were evaluated by DVA and SAXS. The results showed that the LLDPE and PMMA were somewhat thermodynamically miscible, and the structure of LLDPE/PMMA composite with a high mass gain was not easily broken when annealed at temperatures higher than T_m of LLDPE ($T_{m,LLDPE}$). DVA also showed that they retain high storage modului at temperatures beyond the LLDPE melting transition. Further, the extent of the storage modulus can be controlled through controlling the mass gain of PMMA.

Chapter 6 demonstrates the preparation of LLDPE/PDMS composite with a hydrophobic surface. Results of X-ray photoelectron spectroscopy (XPS) and attenuated total reflection Fourier-transform infrared spectroscopy (ATR-FTIR) indicated that PDMS was located on the surface of the LLDPE substrate. Scanning electron microscope-energy dispersive X-ray (SEM-EDX) measurement provided the depth information indicating that PDMS existed in the LLDPE substrate. Water contact angle measurement revealed that the hydrophobicity of PE had been improved from 94º to 105º by incorporating PDMS. The microstructure and mechanical properties of the composite were also investigated by SAXS, WAXD, DSC, DVA, and tensile tests.

Finally, **Chapter 7** gives the general conclusions drawn from Chapter 3 to 6, points out that

the originality of this research, explains the main problems remaining in future in regard to the preparation of semicrystalline/amorphous polymer composites using $scCO_2$.

1.5 References

[1] C. C. Han, B. J. Bauer, J. C. Clark, Y. Muroga, Y. Matsushita, M. Okada, Q. Tran-cong, T. Chang, *Polymer* **1988**, 29, 2002.

[2] Polymer Blend; S. Akiyama, T. Inoue, T. Nishi, Eds. CMC Publishing: Tokyo, **1981**; p 56.

[3] Y. Kamiya, K. Mizoguchi, K. Terada, Y. Fujiwara, J. S. Wang, *Macromolecules* **1998**, 31, 472.

[4] G. Rindfleisch, T. P. DiNoia, M. A. McHugh, *J. Phys. Chem.* **1996**, 100, 15581.

[5] J. J. Shim, K. P. Johnston, *AIChE. J.* **1989**, 35, 1097.

[6] J. J. Shim, K. P. Johnston, *AIChE. J.* **1991**, 37, 607.

[7] R. B. Yoganathan, R. Mammucari, N. R. Foster, *Polymer reviews* **2010**, *50*, 144.

[8] J. J. Watkins, T. J. McCarthy, *Macromolecules* **1994,** *27*, 4845.

[9] D. Li, Z. Liu, B. Han, L. Song, G. Yang, T. Jiang, *Polymer* **2002**, *43*, 5363.

[10] J. J. Watkins, T. J. McCarthy, *Macromolecules* **1995**, *28*, 4067.

[11] E. Kung, A. J. Lesser, T. J. McCarthy, *Macromolecules* **1998**, *31*, 4160.

[12] J. Zhang, A. J. Busby, C. J. Roberts, X. Chen, M. C. Davies, S. J. B. Tendler, S. M. Howdle, *Macromolecules* **2002**, *35*, 8869.

[13] A. J. Busby, J. Zhang, A. Naylor, C. J. Roberts, M. C. Davies, S. J. B. Tendler, S. M. Howdle, *J. Mater. Chem.* **2002**, *13*, 2838.

[14] A. Naylor, S. M. Howdle, *J. Mater. Chem.* **2005**, *13*, 2838.

[15] A. J. Busby, J. Zhang, C. J. Roberts, E. Lester, S. M. Howdle, *Adv. Mater.* **2005**, *17*, 364.

[16] A. Naylor, P. S. Timashev, A. B. Solov'eva, N. A. Erina, S. Kotova, A. J. Busby, V. K. Popov, S. M. Howdle, *Adv. Mater.* **2008**, *20*, 575.

[17] T. Hoshi, T. Sawaguchi, T. Konno, M. Takai, K. Ishihara, *Polymer* **2007**, *48*, 1573.

[18] T. Sawaguchi, Y. Muroga, H. Ishikawa, T. Hoshi, T. Hagiwara, S. Yano, *Kobunshi Ronbunshu* **2005**, *62*, 251.

[19] E. Kung, A. J. Lesser, T. J. McCarthy, *Polym. Prepr. (Am. Chem. Soc., Div. Polym. Chem.)* **1997**, *38*, 462.

[20] J. J. Watkins, T. J. McCarthy, *Polym. Prepr. (Am. Chem. Soc., Div. Polym.Chem.)* **1994**, *35*, 699.

[21] D. Li, B. X. Han, H. K. Yan, *Chin. Chem. Lett.* **1999**, *10*, 871.

[22] J. J. Watkins, G. D. Brown, V. S. RamachandraRao, M. A. Pollard, T. P. Russell, *Macromolecules* **1999**, *32*, 7737.

[23] X. Dai, Z. Liu, B. Han, G. Yang, X. Zhang, J. He, J. Xu, M. Yao, *Macromol. Rapid Commun.* **2002**, *23*, 626.

[24] D. Li, B. Han, *Ind. Eng. Chem. Res.* **2000**, *39*, 4506.

[25] S. Kato, Y. Tsujita, H. Yoshimizu, T. Kinoshita, J. S. Higgins, *Polymer* **1997**, *38*, 2807.

[26] O. S. Fleming, K. L. A. Chan, S. G. Kazarian, *Polymer* **2006**, *47*, 4649.

[27] J. Riffle, I. Yilgor, A. Banthia, G. Wilkes, J. McGrath, *Organic Coatings Applied Polymer Science Proceedings* 1981, **46**, 397.

[28] I. Yilgor, Jr WP. Steckle, E. Yilgor, R. Freelin, J. Riffle, *Journal of Polymer Science, Part A Polymer Chemistry* 1989, **27,** 3673.

[29] S. Garin, L. Lecamp, B. Youssef, C. Bunel, *Eur. Polym. J.* 1999, **35**, 473.

[30] S. Hou, Y. Chung, C. Chan, P. Kuo, *Polymer* 2000, **41,** 3263.

Chapter 2

Methodology

Table of Contents

Chapter 2

Methodology

2.1 Materials

A polyolefin (isotactic polypropylene or linear low-density polyethylene) substrate was prepared from a commercially obtained pellet (Mitsui Chemical, Inc., Tokyo, Japan) by hot pressing at 190 °C or 170 °C. The substrate was cut into pieces with dimensions of 20 × 20 × 0.5 mm^3, extracted with acetone for 24 h in a Soxhlet extractor to remove impurities in the substrate, and dried in vacuo at room temperature. Methyl methacrylate (MMA) and acetone were purchased, and used without further purification, from Wako Pure Chemical Industries, Ltd., Tokyo, Japan, and Kanto Chemical Co., Tokyo, Japan, respectively. 2,2'-Azobis(isobutyronitrile) (AIBN) was purchased from Kanto Chemical Co., Inc., Japan, and used after recrystallization from methanol. Octamethylcyclotetrasiloxane (D4), hexamethyldisiloxane and sulfuric acid were purchased from Tokyo Chemical Industry Co., Ltd., Japan; Acros Organics, France; and Kanto Chemical Co., Tokyo, Japan, respectively, and used without further purification. Carbon dioxide (CO_2) with a purity of 99.5% was provided by Tomoe Shokai Co., Tokyo, Japan, and used as received.

2.2 Preparation of polymer composites using $scCO_2$

Samples were prepared in an apparatus consisting of a 50 mL stainless steel vessel, magnetic stirrer, constant-temperature air bath (Model SCF-Sro, JASCO Co., Tokyo, Japan), thermocouple, and pressure gauge. The pressure gauge comprised a transducer (Model PTX1400, Druck Japan Co., Tokyo, Japan) and an indicator, which had a precision of ±0.2% in the pressure range of 0–40 MPa. The polyolefin substrate was suspended in the vessel by means of a wire mesh to ensure that no part of the substrate was in contact with the monomer solution or the vessel wall. The polyolefin substrate, monomer, and initiator were placed in the vessel, which was then sealed [1]. The vessel was then flushed by CO_2 at atmospheric pressure. After the system reached thermal equilibrium, the vessel was pressurized up to a specific CO_2 pressure using a CO_2 delivery pump (Model SCF-Get, JASCO Co., Tokyo, Japan). The polyolefin substrate was soaked for 1 h. The vessel was then pressurized to the last specific pressure (to compensate for the drop in pressure due to dissolution of the monomer and initiator), heated to the reaction temperature (80 °C), and held for a specific time. The vessel was then cooled to 10 °C and gradually returned to ambient pressure. After extracting the sample with acetone or chloroform for 24 h to remove unreacted reagents and the surface poly(methyl methacrylate) (PMMA) or polydimethylsiloxane (PDMS) using a Soxhlet extractor, the polymer composite was dried in vacuo at room temperature. The mass

gain was calculated using the following equation:

$$\text{Mass gain (wt\%)} = \frac{W_t - W_0}{W_0} \times 100 \quad (1)$$

where W_0 is the initial weight of polyolefin substrate and W_t is the weight of polymer composite sheet after drying. The density of the polymer substrate was calculated using the following equation:

$$\text{Density (g/cm}^3\text{)} = \frac{W_t}{L^2 \times T} \quad (2)$$

where L is the average length of the four sides and T is the thickness of the polymer composite sample. The length and thickness were measured at room temperature.

2.3 Characteristic of polymer composites

2.3.1 Transmission electron microscopy

Transmission electron microscopy (TEM) micrographs were recorded using a JEOL JEM-100CX transmission electron microscope at an accelerating voltage of 100 kV. RuO_4 was used to stain the composite specimens, which were cut into ultra-thin sections at room temperature using an ultramicrotome.

2.3.2 Atomic force microscopy

Atomic force microscopy (AFM) experiments were performed using a Nanoscope IIIa-controlled Dimension 3000 AFM (Digital Instrument, Santa Barbara, CA). Commercial silicon cantilever probes, with a nominal tip radius of less than 10 nm (Nanoscope Olympus, 160 μm cantilever length and spring constant ranging 12-103 N m^{-1}), were employed just under their fundamental resonance frequencies of about 300 kHz. Height and phase images were acquired simultaneously under ambient conditions. Scan rates were set at 2 Hz for all

images.

2.3.3 Small-angle X-ray scattering

Small-angle X-ray scattering (SAXS) experiments were carried out using synchrotron radiation as the X-ray source at the Photon Factory of the High Energy Accelerator Organization at Tsukuba, Ibaragi, Japan. The wavelength of the X-rays was 0.1488 nm and the scattered intensity was detected using a one-dimensional position-sensitive proportional counter (PSPC) with 512 channels that was located about 2 m from the sample. The set-up was calibrated on a sample of expanded chicken collagen, which gave a set of sharp diffractions corresponding to a Bragg spacing of 653 Å. The details of the instrumentation and procedure are described elsewhere [2].

2.3.4 Wide-angle X-ray diffraction

Wide-angle X-ray diffraction (WXRD) experiments were performed at 20 °C using a Panalytical X'Pert Pro diffractometer. The Cu Kα radiation (wavelength, λ = 0.154 nm) was

generated at 45 kV and 40 mA. All samples were scanned at a rate of 3 °/min between 10° and 40° in reflectance mode. The crystallinity was determined by assuming that the total diffraction within a certain region of reciprocal space is independent of the state of aggregation of the material. The crystallinity, Xc, expressed as the mass fraction of the crystalline component, is then given as

$$Xc = \frac{Ac}{Ac + Aa} \quad (3)$$

where Aa is the area under the peaks corresponding to the amorphous region and Ac is the area remaining under the crystalline peaks [3].

2.3.5 Differential scanning calorimetry

The thermal behavior of the composite was measured using differential scanning calorimetry (DSC) (Seiko Instruments, Inc., DSC6100). The instrument was calibrated using known standards: indium (T_m = 165.8 °C) and zinc (T_m = 419.5 °C). The sample (2–3 mg) was packed into aluminum DSC sample pans with the lid tightly crimped. Measurements were taken between −50 and 200 °C at a scanning rate of 10 °C/min under a nitrogen gas flow.

2.3.6 Dynamic viscoelastic analysis

The dynamic viscoelastic properties of the composite were measured in a tensile mode, using a dynamic viscoelastic analysis (DVA-220, IT Keisoku Seigyo Company, Japan) with a chuck distance of 10 mm and a frequency of 10 Hz. The storage modulus (E'), loss modulus (E") and loss tangent (tan δ) were measured as a function of temperature, using a heating rate of 5 °C/min.

2.3.7 Tensile test

The tensile tests were carried out using a screw-driven model Intesco Co. tensile machine (IM-20ST). The grip interval was 10 mm. All samples were deformed at 20 °C at a strain rate of 100 %/min.

2.3.8 Attenuated total reflection Fourier-transform infrared spectroscopy

To analyze the functional groups on the surface of polymer composite, the attenuated total reflection Fourier-transform infrared spectroscopy (ATR-FTIR) spectra were measured using a FTIR spectrophotometer (PerkineElmer Spectrum One) equipped with a universal ATR sampling accessory. All the measurements were performed under identical conditions (number of scans: 8, resolution: 4 cm^{-1}, 5 points).

2.3.9 X-ray photoelectron spectroscopy

To evaluate the chemical structure of the samples and assess the near-surface composition of the polymer composite, X-ray photoelectron spectroscopy (XPS) was conducted on an AXIS-HSi (Shimadzu/Kratos, Kyoto, Japan) employing Mg Kα excitation radiation (1253.6 eV). The take-off angles of the photoelectron for each atom were fixed at 30° or 90°.

2.3.10 Scanning electron microscope-energy dispersive X-ray

To evaluate the silicon concentration, scanning electron microscope (SEM) (Hitachi S-3000N) and energy dispersive X-ray (EDX) (Hitachi S-3000N, 132-10) analyses of the

cross sections of the polymer composite were performed. The polymer composite was cut normally in an ultramicrotome (Leica EM UC6) at –160°C and then sputter coated with a thin layer of Pt–Pd to improve the electrical conductivity. In all measurements, the acceleration voltage was 15 kV.

2.3.11 Water contact angle

The hydrophilicity of the sample surface was characterized on the basis of water static contact angle measurements. The contact angle with water was measured at room temperature (21°C) by a sessile drop method using a contact angle goniometer. The data shown are an average of three different measurements.

2.3.12 Gel permeation chromatograph

The molecular weight was determined by GPC (TOSOH HLC-8220GPC) with a TOSOHTSK gel GMHxL-G3000HxL-G2000HxL column system. The molecular weight was calibrated using poly(methyl methacrylate) standards. Tetrahydrofuran was used as an eluent,

and the measurement was performed at 40 °C.

2.4 References

[1] J. Zhang, A. J. Busby, C. J. Roberts, X. Chen, M. C. Davies, S. J. B. Tendler, S. M. Howdle, *Macromolecules* **2002**, *35*, 8869.

[2] Y. Muroga, H. Tagawa, Y. Hiragi, T. Ueki, M. Kataoka, Y. Izumi, Y. Amemiya, *Macromolecules* **1988**, *21*, 2756.

[3] A. J. Ryan, J. L. Stanford, W. Bras, T. M. W. Nye, *Polymer* **1997**, *38*, 759.

Chapter 3

Microstructure and Mechanical Properties of Isotactic Polypropylene/Poly(methyl methacrylate) Composite using Supercritical Carbon Dioxide

Table of Contents

Chapter 3

Microstructure and Mechanical Proper ties of Isotactic Polypropylene/Poly(methyl methacrylate) Composite using Supercritical Carbon Dioxide

3.1 Introduction

Isotactic polypropylene (iPP) is one of the largest volume polyolefins in the plastics industry. It has many desirable physical properties including low density, high melting temperature, high tensile modulus, and excellent chemical resistance [1]. Combined with its low cost, these properties make iPP ideal for a variety of applications including appliances, packaging, textiles, reinforcing fibers, monofilaments, films, automotive parts, reusable containers of various types, and other durable items for home and garden use. Additionally, the ranges of applications for iPP can also be extended by various physical treatments, for example, thermal treatment and plastic deformation [2–6].

Table 1-1 Production of plastics.

(Unit 1000 t)

2004	2005	2006	2007	2008	2009	2010	2011	2012
3,238	3,240	3,166	3,232	3,089	2,805	2,684	2,834	2,605
2,908	3,063	3,049	3,087	2,869	2,411	2,467	2,448	2,390
2,153	2,151	2,146	2,162	1,797	1,668	1,602	1,529	1,331
1,824	1,734	1,745	1,749	1,594	1,240	1,265	1,275	1,168
720	684	686	698	685	500	572	565	472

However, iPP has the disadvantages such as low surface energy, lack of chemical functionalities, difficulty in dyeing. Moreover, when a polymer composite of iPP with other polymers is prepared, phase separation occurs, and a macro domain structure is formed because of the crystal growth of iPP from the melt or soluble state [7]. The properties of iPP such as storage modulus, yield stress, fracture stress and strain could be changed through the

blending of another amorphous polymer into the amorphous phases of iPP to meet various needs. Poly(methyl methacrylate) (PMMA) is an amorphous polymer having high optical properties, good chemical resistance, and high tensile strength. The present study establishes a method to prepare a new nanocomposite material with PMMA dispersed on a nanometer scale in the amorphous phase of iPP. iPP and PMMA have quite different physical properties and cannot be sufficiently blended using conventional methods. In this study, $scCO_2$ is used as a processing medium to facilitate effective impregnation of methyl methacrylate (MMA) monomer into the amorphous phase of iPP, followed by radical-initiated in situ polymerization.

To date, although there is extensive work in the area of semicrystalline/amorphous polymer composites (such as polyethylene/amorphous polymer composites) prepared in $scCO_2$, the study of iPP as a polymer substrate is rather limited. Additionally, changes of melting temperature of substrate polymer after blending with an amorphous polymer, thermodynamic miscibility of respective component, and thermal stability of the composites haven't been evaluated. In this study, the details of the preparation of an iPP/PMMA composite are firstly reported. We investigate the microstructure of the composite by combining transmission electron microscopy (TEM), atomic force microscopy (AFM), and small-angle X-ray scattering (SAXS). The crystallinity of the composite was investigated by wide-angle X-ray diffraction (WXRD), and the melting temperature and enthalpy of crystal were determined by

differential scanning calorimetry (DSC). The mechanical properties of the composite were analyzed by means of dynamic viscoelastic analysis (DVA) and tensile tests. The thermodynamic miscibility was evaluated by DSC and DVA.

3.2 Experimental section

The iPP substrate (20 × 20 × 0.5 mm^3), MMA monomer (2 g), and AIBN initiator (0.03 g) were placed in the vessel, which was then sealed [8]. The vessel was then flushed by CO_2 at atmospheric pressure. After the system reached thermal equilibrium (35°C), the vessel was pressurized up to a specific CO_2 pressure using a CO_2 delivery pump. The iPP substrate was soaked for 1 h. The vessel was then pressurized to the last specific pressure, heated to the reaction temperature (80 °C), and held for 24 h to ensure that the polymerization of MMA was complete. The vessel was then cooled to 10 °C and gradually returned to ambient pressure. After treating the product sample with acetone for 24 h to remove unreacted reagents and the surface PMMA using a Soxhlet extractor, the iPP/PMMA composite was dried in *vacuo* at room temperature.

The molecular weight of PMMA produced inside and outside iPP substrate was determined by a gel permeation chromatograph (GPC) with THF as the mobile phase. The PMMA produced inside of iPP substrate was separated using the method as follows. The iPP/PMMA composite was dissolved in hot xylene. The precipitate (iPP) was produced by precipitation by addition of acetone and removed by filtration. The remaining solution was rotary evaporated to isolate the PMMA.

A reference sample was also prepared for SAXS and other analyses from the solution as

follows: equal masses of iPP and PMMA were dissolved in xylene at reflux temperature and the solution was poured into methanol to obtain the precipitate, which was vacuum-dried under heat. The obtained precipitate was shaped into a sheet following the same process as was used for the iPP substrate.

3.3 Results and discussion

3.3.1 Preparation of iPP/PMMA composite in $scCO_2$

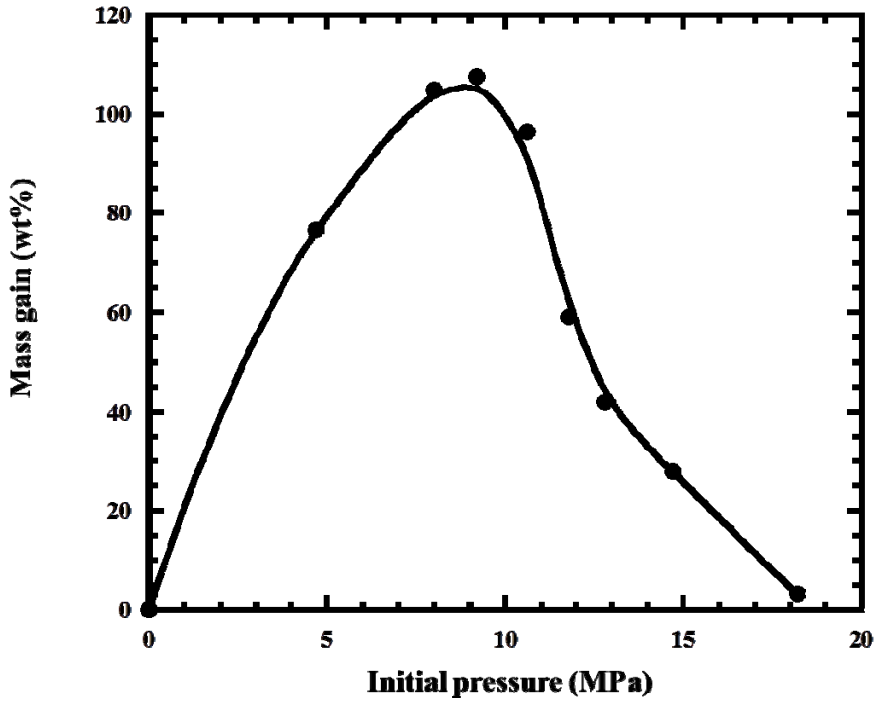

Figure 3-1 Effect of initial pressure on the mass gain of PMMA into iPP substrate after polymerization.

Figure 3-1 shows the effect of the initial pressure of CO_2 on the mass gain of PMMA into the iPP substrate after polymerization. The mass gain initially increases in correlation with the initial pressure, reaching a maximum of 109 wt% when the initial pressure of CO_2 is about 9 MPa, and then decreases with further increases in the initial pressure. Therefore, the mass

gain of the PMMA sample can be controlled by modulating the initial pressure of CO_2. These results are similar to those obtained in our previous study [9].

$ScCO_2$ is a good swelling agent and generally a poor solvent for most polymers. Impregnation of $scCO_2$ starts on the surface of the substrate followed by gradual permeation into the inner substrate. The swelling kinetics of CO_2 into the polymer matrix depends on both the temperature and pressure [10,11]. Differing from other polymers, PMMA possesses the swelling properties in CO_2 that depend on the temperature and pressure [12]. When the initial pressure of CO_2 is low, both the solubility of MMA and the swelling of the amorphous iPP region are low, resulting in insufficient generation of PMMA in the iPP substrate. An increase in the initial pressure results in improved solubility of MMA, and swelling of the amorphous iPP region, which results in an increase in the mass gain with higher initial pressures. However, the partition coefficient of MMA in CO_2 becomes larger than that in iPP substrate at even higher pressures. Additionally, at high pressure, the rate of the decomposition of AIBN is relatively slow [13,14]. A combination of these factors explains the mass gain decreases with increasing initial pressures over 9 MPa (see Figure 3-1).

We also notes that after incorporation of PMMA, the dimensions (length, thickness) of the specimens have grown significantly from their initial substrate dimensions while retaining their original square shape (the lengths of four sides are almost same even after the polymerization). Figure 3-2 shows the changes in length, thickness, and density of the

iPP/PMMA composites as a function of the mass gain of PMMA. As expected, the higher the PMMA incorporation, the larger the final dimensions. Interestingly, although the dimensions show a nearly linear growth up until 75 wt%, the growth significantly slows after 75 wt%. iPP and PMMA have densities of 0.881 g/cm^3 and 1.19 g/cm^3, respectively, and the iPP/PMMA composites with a mass gain of 75 wt% and 109 wt% have densities of 0.910 g/cm^3 and 0.960 g/cm^3, respectively. This demonstrates a significant increase in the density of the composites above 75 wt%, which is due to the constriction of the dimensions with increasing mass gain at this point. In addition, the interactions between the chains of generated PMMA occur gradually, after which the density of the iPP/PMMA composite is closer to the density of PMMA.

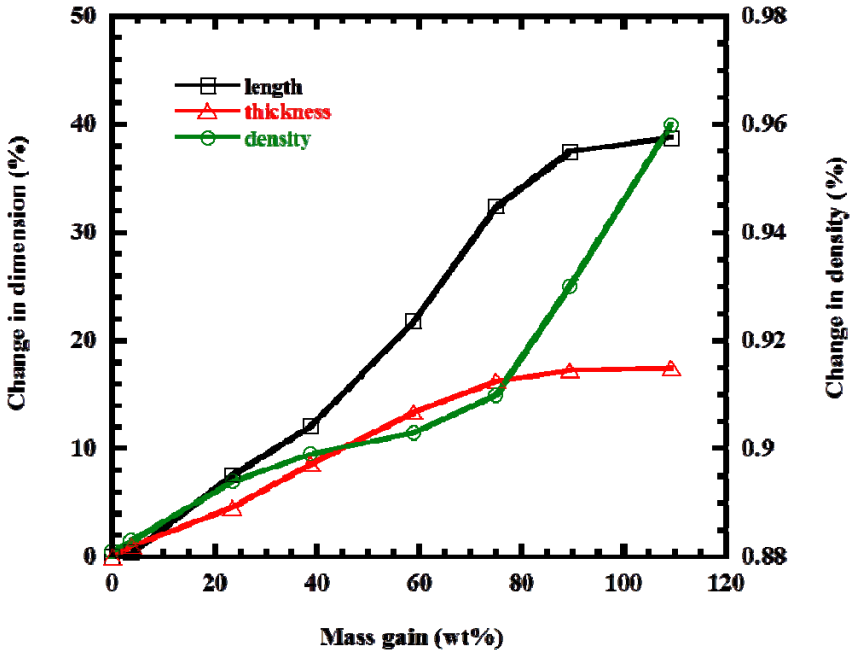

Figure 3-2 Changes in length, thickness, and density of iPP/PMMA composites as a function of the mass gain of PMMA.

GPC measurements indicate the molecular weight of PMMA produced inside of iPP substrate is higher than that produced outside of iPP substrate. PMMA from a 75 wt% iPP/PMMA composite exhibited a M_w = 62.3 × 10^4 with a PDI (M_w/M_n) = 1.9. The corresponding PMMA produced outside of iPP substrate exhibited a M_w = 5.8 × 10^4 with a PDI = 2.5. PMMA from a 109 wt% iPP/PMMA composite exhibited a M_w = 84.8 × 10^4 with a PDI = 1.6. The corresponding PMMA produced outside of iPP substrate exhibited a M_w = 6.5 × 10^4 with a PDI = 2.7. These results are similar to those obtained in the literature [15].

3.3.2 Microstructure analyses of the iPP/PMMA composite

Figure 3-3 displays TEM micrographs of the reference sample (iPP/PMMA = 100/100) and iPP/PMMA composite (mass gain: 109 wt%; iPP/PMMA = 100/109). The dark portions in the micrographs are iPP domains and the light portions are PMMA domains. In the reference sample (a and d), large PMMA domains of micron scale were formed in the iPP substrate and the phase boundary was clear. Conversely, in the iPP/PMMA composite prepared by $scCO_2$ (b, c, and e), the PMMA domains are finely dispersed within the iPP substrate on a nanometer scale and the phase boundary was ambiguous. Nevertheless, when the micrographs of both the reference sample and iPP/PMMA composite are magnified (d and e), numerous streaks

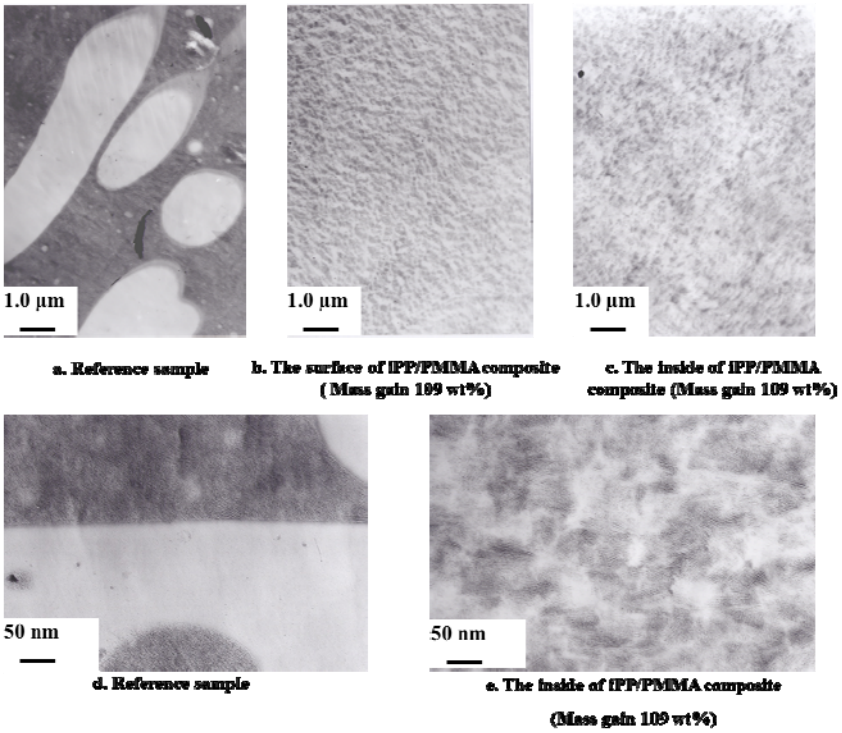

Figure 3-3 TEM images of reference sample and iPP/PMMA composite (mass gain: 109 wt%).

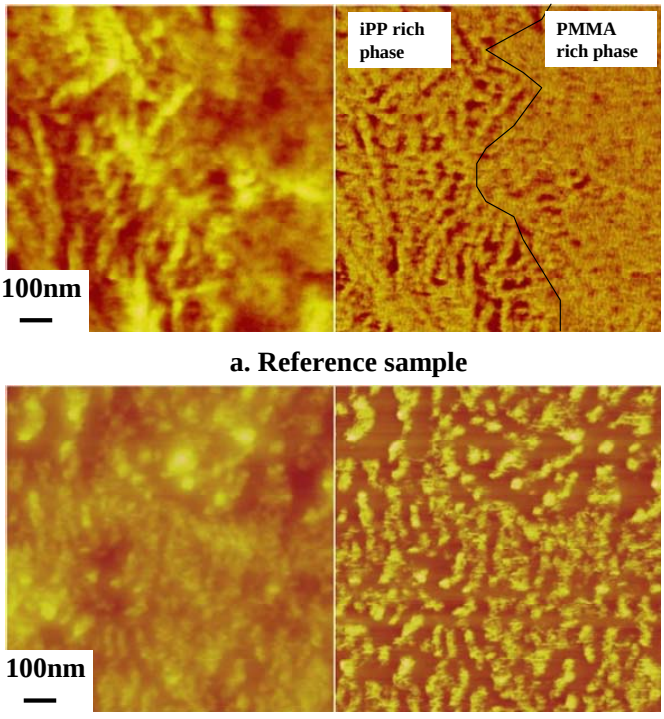

Figure 3-4 AFM height (left) and phase (right) images of reference sample and iPP/PMMA composite (mass gain: 109 wt%).

are evident. These streaks signify lamellar crystal of iPP. This indicates that some portions of the original crystalline phases of iPP are preserved throughout the preparation process.

Figure 3-4 shows the AFM height and phase images of the reference sample and the iPP/PMMA composite (mass gain: 109 wt%). From the height images, it can be seen that the surface of the reference sample is rougher than that of the iPP/PMMA composite. This may indicate that the $scCO_2$ impregnation assists in producing a more homogeneous internal structure of the polymer. The height image of the iPP/PMMA composite also differs from that of the reference sample due to the presence of a granular-shaped feature. This change in topography is likely due to the incorporation of PMMA into iPP, which results in a change in the internal structure of the iPP. In the phase images, a strong contrast of bright and dark regions was observed for all samples. This is consistent with the fact that iPP and the composite are semicrystalline polymers consisting of crystalline and amorphous phases with different moduli. The bright portions are attributed to the stiffer materials whereas the dark portions are attributed to the softer materials [16,17]. In the reference sample, the left side shows a strong contrast of bright and dark regions, which is attributed to the crystalline and amorphous phases of iPP. Conversely, the right side shows only bright regions, which are attributed to PMMA. The phase boundary is clear. In contrast, in the iPP/PMMA composite, the phase boundary is ambiguous and the amorphous regions of iPP expand, as a result of the polymerization of PMMA within the amorphous regions.

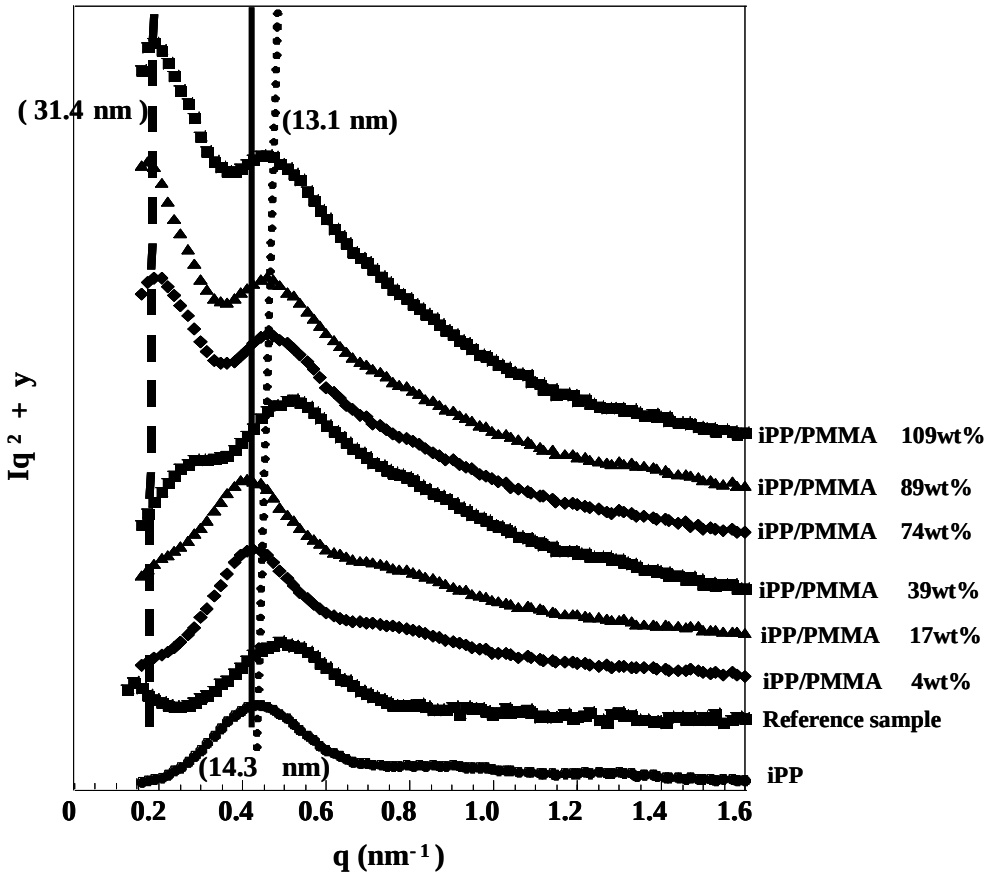

Figure 3-5 Plots of Lorenz-corrected SAXS intensity Iq^2 vs. q of reference sample and iPP/PMMA composites.

Assuming that the morphology is globally isotropic but locally lamellar, the microstructural periodicity of the iPP/PMMA composite and reference sample can be obtained from unoriented SAXS patterns. Figure 3-5 plots the scattering data in the form of the Lorenz-corrected SAXS intensity, Iq^2, versus the scattering vector, q, where I is the scattering intensity and q is defined by

$$q = \frac{4\pi}{\lambda}\sin\frac{\theta}{2} \qquad (1)$$

where λ is the wavelength of the X-ray, and θ is the scattering angle. The iPP sample shows

both first- and second-order reflections, which are assigned to the long period corresponding to the sum of thickness of a crystalline layer, iPPc, and an amorphous layer, iPPa, in semicrystalline lamellae. This shows that the interface between the crystalline and amorphous regions is sharp, so the application of a two-phase model is appropriate. The Bragg spacing was estimated from the maximum q^* using the relation $d_1 = 2\pi/q^*$. The magnitude, d_1, of 14.3 nm for iPP, estimated from $q^* = 0.439$ nm^{-1}, is comparable with the reported value of 15.3 nm [18].

First- and second-order reflections are also observed in the reference sample. In this case, the scattering intensity for a q smaller than 0.3 nm^{-1} tends to increase as q decreases, which indicates the presence of large domains in the reference sample. These results are reasonable since the phases of iPP and PMMA in the reference sample are macroscopically separated, as is shown in figure 3-3a, and so the microstructure of iPP would remain intact.

In the iPP/PMMA composite, the SAXS profiles gradually change with increases in the mass gain of PMMA: The first-order reflection (approximately $q = 0.4$ nm^{-1}) tends to shift to a larger q and both intensities of the first- and second-order (approximately q = 0.8 nm^{-1}) reflection tend to become weaker, and the second-order reflection even disappears finally (This can be seen clearly in Figure 11). In the iPP/PMMA composite with a mass gain of 17 wt%, a shoulder appears in a q range around 0.3 nm^{-1}, which becomes a bump as the mass gain of PMMA increases up to a maximum of q of ~0.20 nm^{-1} at 109 wt% mass gain, which

corresponds to a dimension of ~31 nm. From these results, it is evident that MMA and AIBN, dissolved in $scCO_2$, are impregnated into the amorphous phase of iPP and subsequently polymerized in situ to form new phases consisting of polymerized PMMA embedded in amorphous phases of iPP. The structures of the rest of the amorphous phases and crystalline phases of iPP are unchanged or only slightly modified, as shown in Figure 3-6.

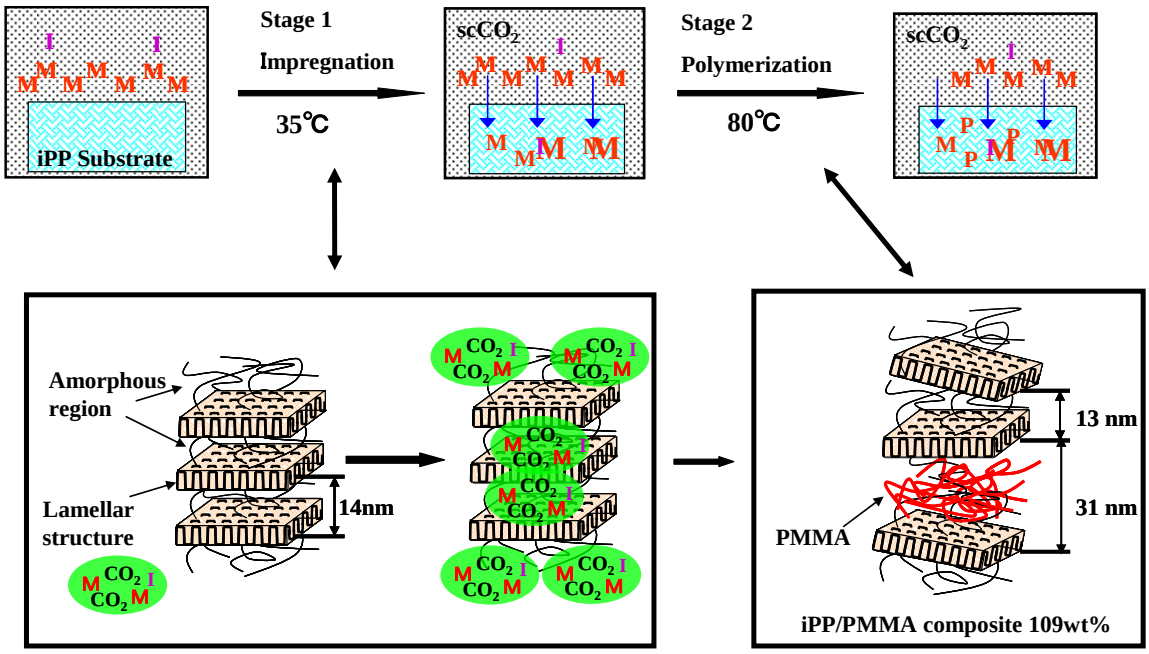

Figure 3-6 Formation mechanism model of iPP/PMMA composite (M: Monomer (MMA); P: (PMMA); I: Initiator (AIBN)).

Based on the results of TEM, AFM, and SAXS analyses, the mechanism of the formation of the iPP/PMMA composite was established (Figure 3-6). In stage 1, the monomer and initiator were dissolved in $scCO_2$ and impregnated into the amorphous interlamellar regions of iPP substrate. In stage 2, after reaching the polymerization temperature, the monomer

polymerized within the amorphous interlamellar regions of iPP substrate. The polymerization of monomer led to the imbalance of the partition coefficient of monomer within and outside of the iPP substrate. The monomer outside of the iPP substrate thus permeated into the amorphous regions of the iPP substrate, and the polymerization reaction was continuous. As a result, iPP and PMMA were effectively blended at the nanometer level.

3.3.3 Crystallinity of the iPP/PMMA composite

Figure 3-7 shows the WXRD patterns of PMMA, iPP, and iPP/PMMA composites. It can be seen that the WXRD patterns of both the iPP and iPP/PMMA composite present the characteristic peaks for the (110), (040), (130), (111), and (041) planes of the well-known α-form (monoclinic phase) [4,6,19,20]. The angular positions of the diffraction peaks of the crystalline iPP are almost identical for original iPP substrate and for the iPP/PMMA composite, indicating that the crystal forms are not changed upon the addition of PMMA. However, the amorphous regions of the iPP/PMMA composite increased with the mass gain of PMMA, which indicates that the overall crystallinity decreases with increases in the mass gain of PMMA (figure 3-8). The reduction in sample crystallinity is due to dilution as a result of the addition of PMMA to the amorphous iPP regions, and the resultant increase in the size

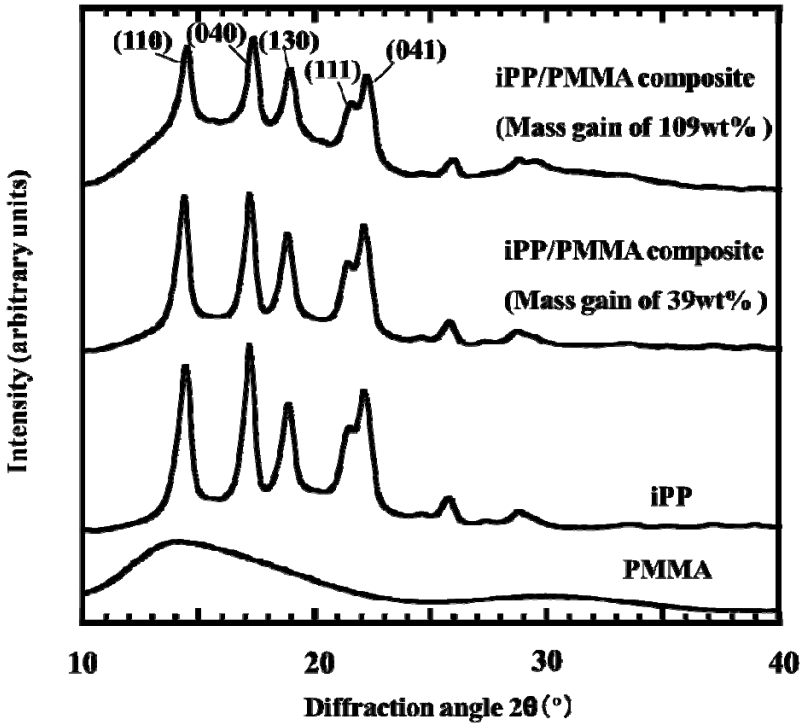

Figure 3-7 WXRD patterns of PMMA, iPP, and iPP/PMMA composites.

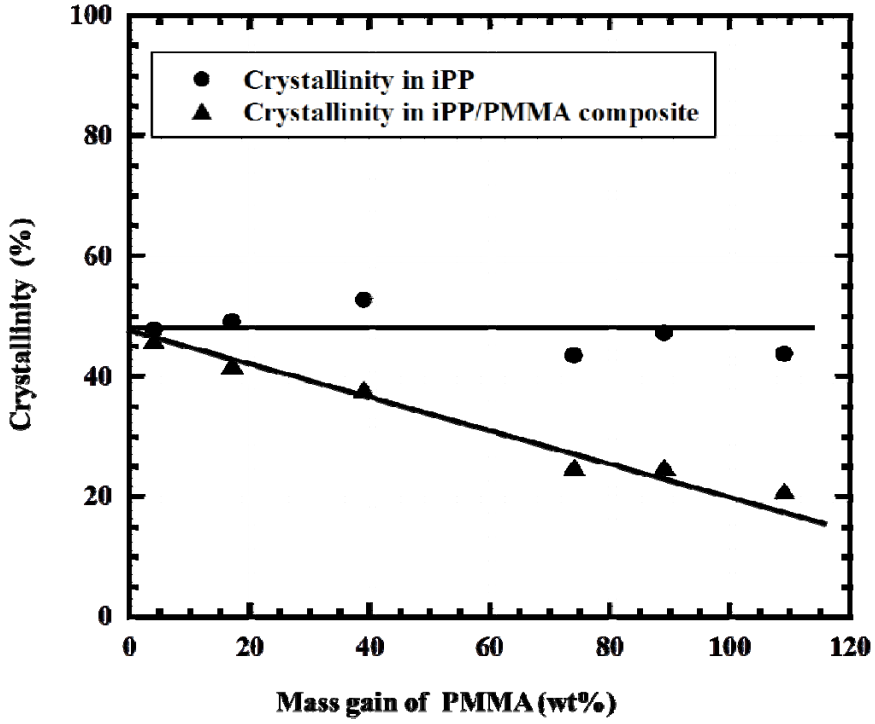

Figure 3-8 Relationship between crystallinity and mass gain of PMMA.

of the amorphous regions. Percent crystallinity in iPP, X_{iPP}, was calculated as follows:

$$X_{iPP}\,(\%) = \frac{X_{iPP/PMMA}}{W_{iPP}} \qquad (2)$$

where X_{iPP} is the crystallinity of iPP/PMMA composite assumed to be dependent only on the crystalline regions of iPP, $X_{iPP/PMMA}$ is the crystallinity of the iPP/PMMA composite, and W_{iPP} is the weight fraction of iPP. X_{iPP} does not change, although $X_{iPP/PMMA}$ decreases according to an increase in the mass gain of PMMA. The total amount of crystalline iPP remains unchanged. These results indicate that the MMA polymerizes solely within the amorphous regions of the polymer.

3.3.4 Thermodynamic and mechanical properties of the iPP/PMMA composite

Differential scanning calorimetry, shown in figure 3-9, confirmed the WXRD data. In iPP/PMMA composites, strong iPP melting endotherms were observed. The melting endotherms reveal that the composite preparation does not affect the crystalline region of the iPP substrate. Further, the melting endotherm peaks became broad and shallow with increasing mass gain of PMMA. This is due entirely to dilution of the crystalline regions by the addition of PMMA to amorphous iPP regions. Although the top temperature of the melting endotherm peaks (T_{m2}) was not significantly affected by the mass gain of PMMA, the

starting temperature of melting endotherm peaks (T_{m1}) decreased with the mass gain of PMMA, as shown in figure 3-10. Generally, a decrease in T_{m1} is caused by changes in the kinds of crystals, or crystallinity of the sample. However, the WXRD data confirmed that the crystal types and crystallinity are independent of the addition of PMMA (figures 3-7 and 3-8). It is possible that the decrease in T_{m1} can be explained by the formation mechanism of the iPP/PMMA composite, as was discussed in microstructure analyses. From the SAXS profiles, slight changes in the lamellar structure can be postulated. Figure 3-11 shows the corresponding relationship between the SAXS profiles and lamellar models. In iPP, both the first- and second-order reflections are evident. In the iPP/PMMA composite with a mass gain of 17 wt%, a shoulder appears at a q of ~0.3 nm^{-1}, which corresponds to a relatively large dimension of ~21 nm. Because the mass of PMMA is relatively low, most of the iPP lamellar structures are retained, and the first- and second-order reflections can still be observed, although they are weak. However, in the iPP/PMMA composite with a mass gain of 109 wt%, a strong peak appears at a q of ~ 0.2 nm^{-1}, which corresponds to a larger dimension of ~31 nm, and the first-order reflection is weaker, while the second-order reflection is not observed. As the amount of crystal is constant, the formation of new lamellar structures causes the reflections originating from the iPP lamellar to weaken or even disappear. The changes of T_{m1} and T_{m2} are attributed to changes in the microstructure; as the volume of the amorphous regions of iPP increase, melting the crystal is more facile, so T_{m1} decreases with the mass gain

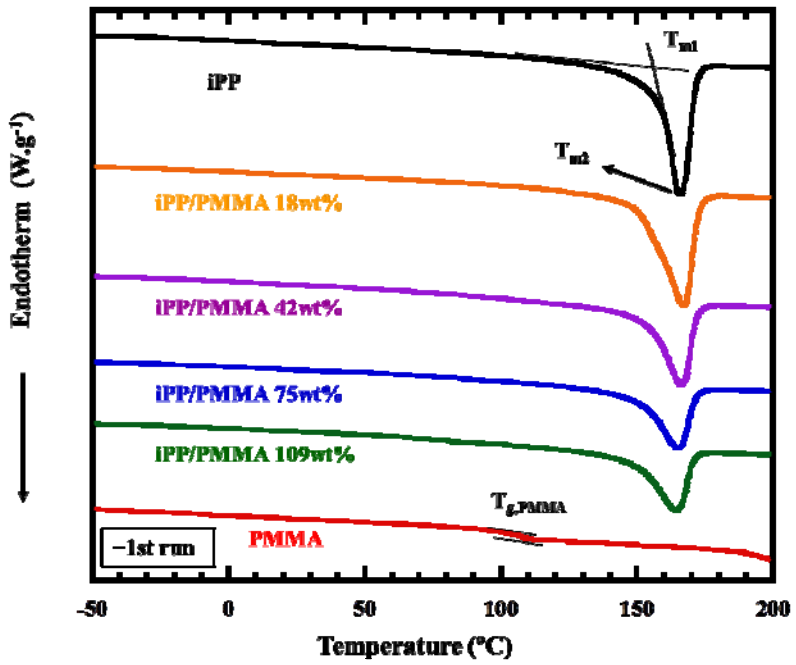

Figure 3-9 DSC thermograms of iPP, PMMA, and iPP/PMMA composites.

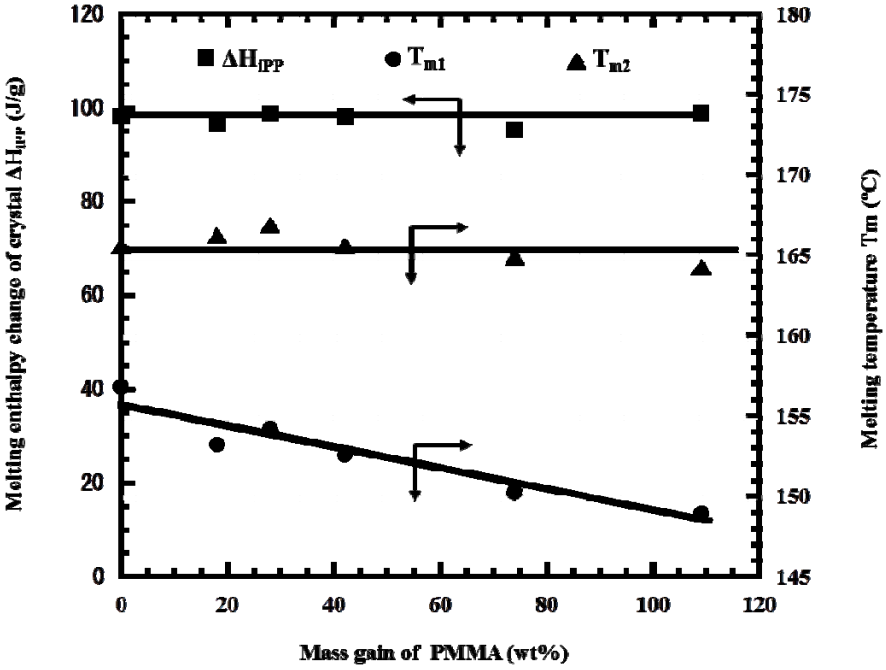

Figure 3-10 Relationship between the changes of melting enthalpy and of iPP crystal (ΔH_{iPP}), melting temperature of iPP/PMMA composite (T_m) and mass gain of PMMA .

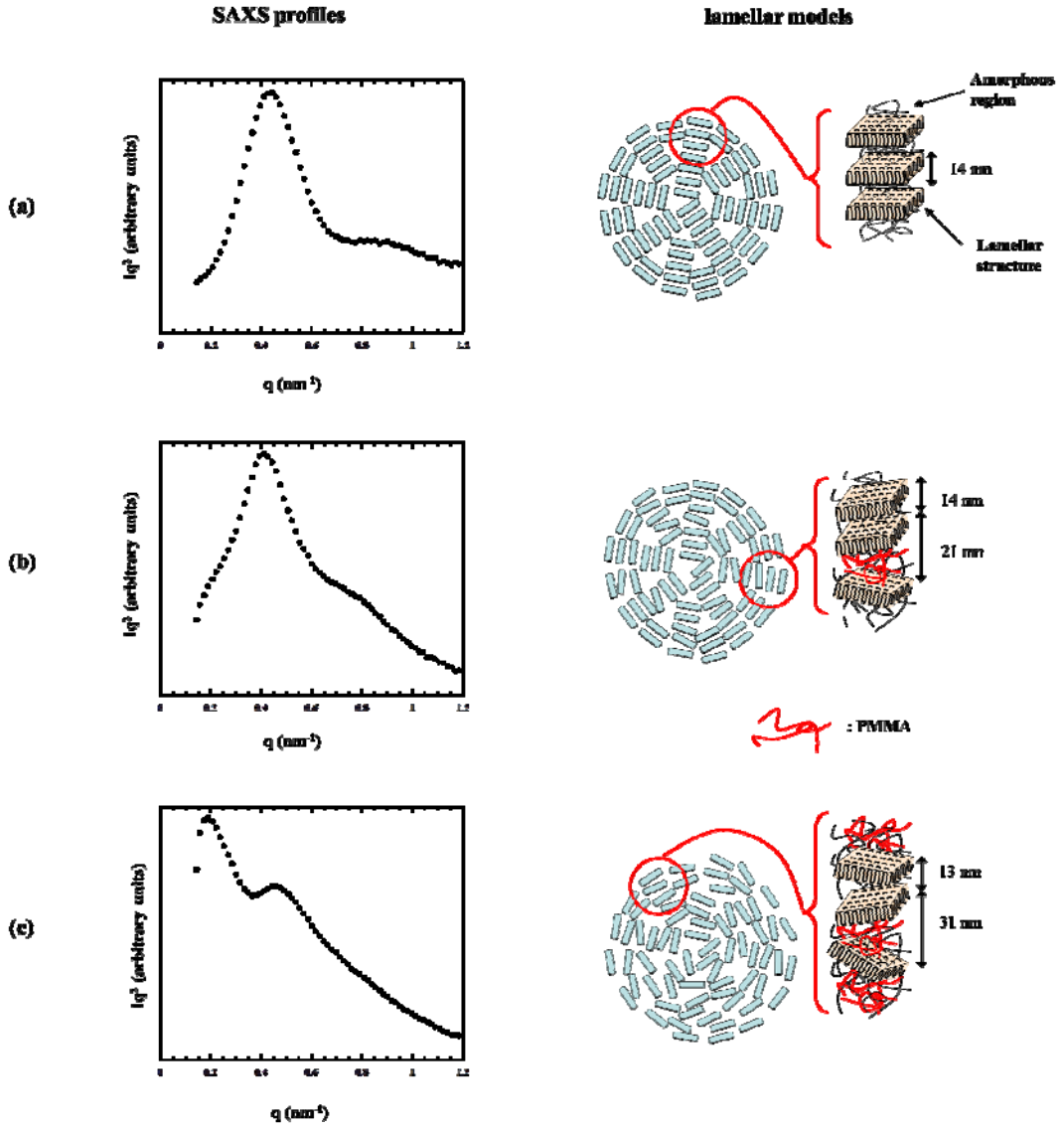

Figure 3-11 Corresponding relationship between SAXS profiles and lamellar models ((a): iPP; (b): iPP/PMMA composite 17 wt%; (c): iPP/PMMA composite 109 wt%).

of PMMA. However, because the amorphous regions of iPP were slightly modified by PMMA, T_{m2} did not change significantly with the mass gain of PMMA. Accordingly, the enthalpy change of the melting of the iPP crystal, ΔH_{iPP}, was calculated as follows:

$$\Delta H_{iPP} = \frac{\Delta H_{iPP/PMMA}}{W_{iPP}} \quad (6)$$

where $\Delta H_{iPP/PMMA}$ is the enthalpy change of the melting of the iPP/PMMA composite crystal, which was assumed to be dependent only on the crystalline regions of iPP. The relationship between ΔH_{iPP} and the mass gain of PMMA is shown in figure 3-10. It is evident that ΔH_{iPP} is constant with the mass gain of PMMA. This is further confirmation that the total amount of iPP crystal does not change upon the addition of PMMA, which is in accord with the results of WXRD. These results indicate that although the addition of PMMA does not affect the enthalpy change of the melting of the iPP crystal nor the top temperature of iPP crystal melting, it did reduce the temperature at which the iPP crystal begins to melt.

The measurement of dynamic viscoelastic behavior is an effective method of evaluating

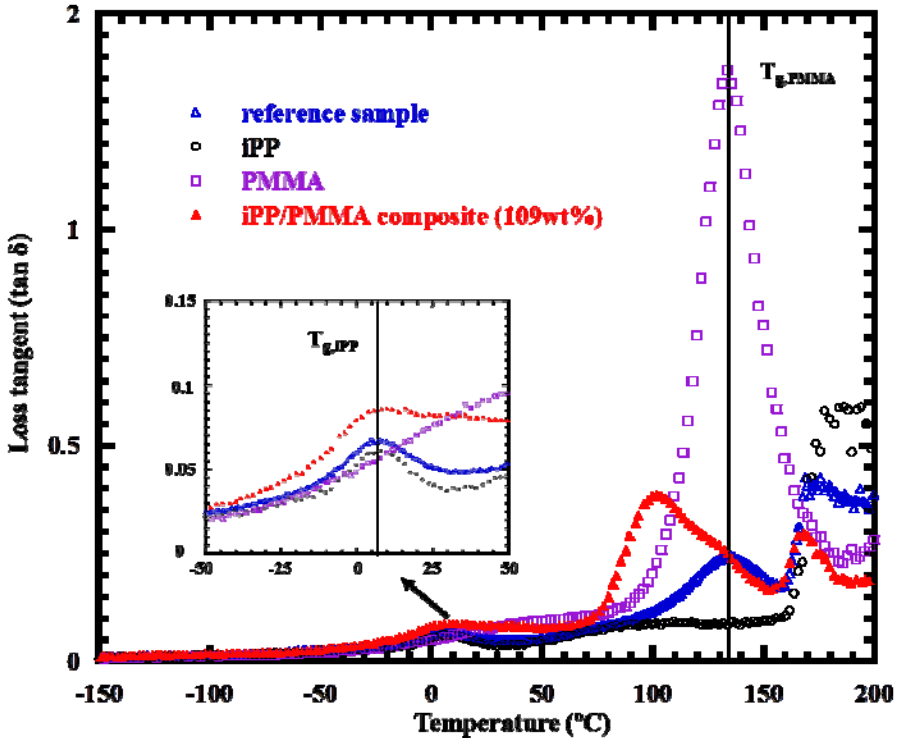

Figure 3-12 Temperature dispersion curves of the loss tangent (tan δ) for original iPP, PMMA, reference sample, and iPP/PMMA composites.

the miscibility of two components through the determination of the glass transition temperature, T_g, of the respective components. Figure 3-12 shows the temperature dispersion curves of the loss tangent (tan δ) for iPP, PMMA, the reference sample, and the iPP/PMMA composites. For iPP, the α-relaxation peak appeared at ~0 °C corresponding to the T_g of the iPP amorphous chain ($T_{g,\mathrm{iPP}}$). For PMMA, the α-relaxation peak appeared at ~130 °C, which corresponds to the T_g of the PMMA chain ($T_{g,\mathrm{PMMA}}$). Because iPP and PMMA are immiscible, the peaks in the reference sample correspond to those of iPP and PMMA. The analysis of the iPP/PMMA composite also showed the three peaks which correspond to $T_{g,\mathrm{iPP}}$, $T_{g,\mathrm{PMMA}}$ and T_m of iPP ($T_{m,\mathrm{iPP}}$). The two peaks corresponding to $T_{g,\mathrm{iPP}}$ and $T_{g,\mathrm{PMMA}}$ are shifted with respect to each other: The $T_{g,\mathrm{iPP}}$ peak ($T_{g1,\mathrm{iPP/PMMA}}$) was shifted towards a higher temperature, while the $T_{g,\mathrm{PMMA}}$ peak ($T_{g2,iPP/\mathrm{PMMA}}$) shifted towards a lower temperature. Further, the shifting extent increased with increasing the mass gain of PMMA. This is also observed in DSC thermograms (figure 3-13). Although it is hard to see the $T_{g,\mathrm{iPP}}$ by DSC, the $T_{g,\mathrm{PMMA}}$ component can be observed in the enlargement of DSC. With increasing the mass gain of PMMA, the $T_{g,\mathrm{PMMA}}$ was shifted towards a lower temperature. These results imply that, using this method, the iPP and PMMA polymers were somewhat thermodynamically miscible [21].

Figure 3-14 shows the temperature dispersion curves of the storage modulus (E') of iPP, PMMA, the reference sample, and the iPP/PMMA composites. At temperatures lower than $T_{g2,\mathrm{iPP/PMMA}}$, the E' of the iPP/PMMA composite was larger than that of iPP. Conversely, at

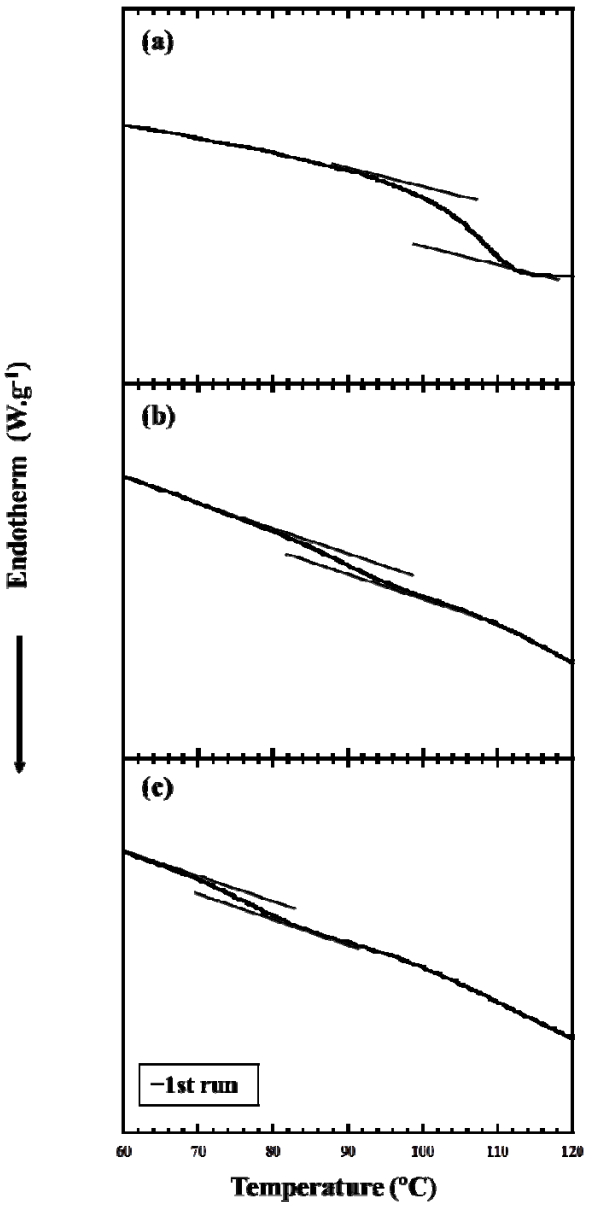

Figure 3-13 The enlargement of DSC thermograms of PMMA and iPP/PMMA composites. (a) iPP/PMMA; (b) iPP/PMMA 75 wt%; (c) PMMA 109 wt%.

temperatures higher than $T_{g,\text{PMMA}}$, the E' of the iPP/PMMA composite was smaller than that of iPP. Therefore, the change of E' occurs between the $T_{g2,\text{iPP/PMMA}}$ and $T_{g,\text{PMMA}}$. The temperature dependence of E' can be explained via the mobility of the polymer chain. At temperatures lower than $T_{g2,\text{iPP/PMMA}}$, the chain mobility of the amorphous regions of iPP was

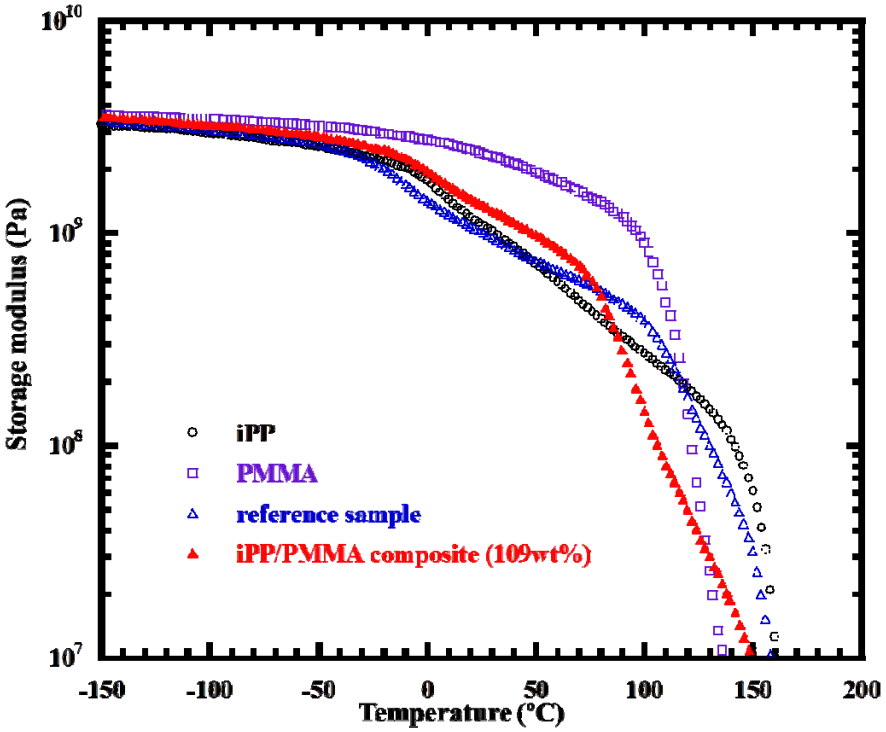

Figure 3-14 Temperature dispersion curves of the storage modulus (E') for original iPP, PMMA, reference sample, and iPP/PMMA composite (mass gain: 109 wt%).

prevented by the glassy PMMA generated in the amorphous regions. The E' of PMMA was larger than that of iPP at temperatures lower than $T_{g2,\text{iPP/PMMA}}$. Therefore, the lowered mobility of the amorphous iPP chains resulted in the E' of the iPP/PMMA composite being higher than that of iPP. At temperatures higher than $T_{g,\text{PMMA}}$, the amorphous regions of iPP/PMMA composite increased to more than that of iPP to allow micro-Brownian motion of the PMMA. Therefore, the E' of PMMA decreased quickly so that the E' of the iPP/PMMA composite was smaller than that of iPP. Similarly, the changes of E' of iPP/PMMA composites can be also explained via the mobility of the polymer chain. Namely, the E' of iPP/PMMA composite can be controlled through the mass gain of PMMA.

Table 3-2 Results of tensile tests.

Sample name	Yield stress (MPa)	Fracture stress (MPa)	Fracture strain (%)
iPP	31	30	1290
iPP /PMMA composite (17 wt%)	34	36	1000
iPP /PMMA composite (28 wt%)	37	35	860
iPP /PMMA composite (59 wt%)	38	33	90
iPP /PMMA composite (74 wt%)	38	33	55
iPP /PMMA composite (109 wt%)	38	34	30
reference sample	—	27	4
PMMA	—	42	5

Table 3-1 lists the results of the tensile test at 20 °C. In the reference sample, a macro-phase separation was induced because iPP and PMMA are immiscible. The conversion of the sample to a macro-phase separated structure was usually had a deleterious effect on its mechanical properties. However, the yield stress of the iPP/PMMA composites is considerably higher than that of iPP. Further, it increased gradually with the mass gain of PMMA and reached a plateau at a mass gain of 59 wt%. The fracture stress of the iPP/PMMA composites is also improved as compared to that of iPP. In addition, the fracture strain decreased rapidly with the mass gain of PMMA. Therefore, nanometer-sized PMMA generated in the amorphous regions significantly affected the mechanical properties of iPP/PMMA composite, which can be controlled through the mass gain of PMMA.

3.4 Conclusion

A composite composed of iPP and PMMA was prepared by *in situ* polymerization of MMA in the presence of iPP in $scCO_2$. PMMA was generated in the amorphous regions between the crystalline lamellae of iPP. PMMA generated in the amorphous region of iPP did not affect its crystallinity, the enthalpy of melting the iPP crystal, nor the top temperature of iPP crystal melting, but it did reduce the starting temperature of iPP crystal melting. Experimental evidence demonstrates that the iPP and PMMA were blended at the nanometer level, and achieved thermodynamic miscibility to some extent. PMMA generated in the amorphous regions of iPP substrate significantly affected the viscoelastic and mechanical properties of the iPP/PMMA composite. At temperatures lower than $T_{g2,\text{iPP/PMMA}}$, the E' of the iPP/PMMA composite was larger than that of iPP. At temperatures higher than $T_{g,\text{PMMA}}$, the E' of the iPP/PMMA composite was smaller than that of iPP. Mechanical properties such as yield stress, fracture stress and strain can be controlled by changing the mass gain of PMMA.

3.5 References

[1] *Polymer Handbook*; J. Brandrup, E. H. Immergut, E. A. Grulke, A. Abe, D. R. Bloch, Eds.; Wiley-Interscience: New York, **1999**; p 159.

[2] W. O´Kane, R. J. Young, A. J. Ryan, *J. Macromol. Sci., Physics* **1995**, *B34*, 427.

[3] L. Poussin, Y. A. Bertin, J. Parisot, C. Brassy, *Polymer* **1998**, *39*, 4261.

[4] D. Ferrer-Balas, M. L. Maspoch, A. B. Martinez, O. O. Santana, *Polymer* **2001**, *42*, 1697.

[5] M. Aboulfaraj, C. G´Sell, B. Ulrich, A. Dahoun, *Polymer* **1995**, *36*, 731.

[6] R. Seguela, E. Staniek, B. Escaig, B. Fillon, *J. App. Polym. Sci.* **1999**, *71*, 1873.

[7] *Polymer Blend*; S. Akiyama, T. Inoue, T. Nishi, Eds.; CMC Publishing: Tokyo, **1981**; p 56.

[8] J. Zhang, A. J. Busby, C. J. Roberts, X. Chen, M. C. Davies, S. J. B. Tendler, S. M. Howdle, *Macromolecules* **2002**, *35*, 8869.

[9] T. Sawaguchi, Y. Muroga, H. Ishikawa, T. Hoshi, T. Hagiwara, S. Yano, *Kobunshi Ronbunshu* **2005**, *62*, 251.

[10] L. N. Nikitin, E. E. Said-Galiyev, R. A. Vinokur, A. R. Khokholov, M. O. Gallyamov, K. Schaumburg, *Macromolecules* **2002**, *35*, 934.

[11] J. R. Royer, J. M. DeSimone, S. A. Khan, *Macromolecules* **1999**, *32*, 8965.

[12] S. M. Sirard, K. J. Ziegler, I. C. Sanchez, P. F. Green, K. P. Johnston, *Macromolecules*

2002, *35*, 1928.

[13] J. M. Desimone, Z. Guan, C. S. Elsbernd, *Science* **1992**, *257*, 945.

[14] Z. Guan, J. R. Combes, Y. Z. Menceloglu, J. M. DeSimone, *Macromolecules* **1993**, *26*, 2663.

[15] E. Kung, A. J. Lesser, T. J. McCarthy, *Macromolecules* **1998**, *31*, 4160.

[16] G. Bar, Y. Thomann, M. H. Whangbo, *Langmuir* **1998**, *14*, 1219.

[17] B. B. Sauer, R. S. McLean, R. R. Thomas, *Langmuir* **1998**, *14*, 3045.

[18] A. R. Berens, G. S. Huvard, R. W. Korsmeyer, F. W. Kunig, *Journal of Applied Polymer Science* **1992**, *46*, 231.

[19] G. Natta, P. Corradini, Inst. Ind. *Nuovo Cimento* **1960**, *15*, 40.

[20] G. Natta, M. Peraldo, Corradini, P. *Mat. e nat.* **1959**, *26*, 14.

[21] *Polymer Alloys and Blends*; A. U. Leszek, Ed.; Hanser: New York, **1989**; p 4.

Chapter 4

Thermal Stability of Isotactic Polypropylene/Poly(methyl methacrylate) Composite using Supercritical Carbon Dioxide

Table of Contents

Chapter 4

Thermal Stability of Isotactic Polypropylene/Poly(methyl methacrylate) Composite Prepared in Supercritical Carbon Dioxide

4.1 Introduction

Since the new polymer composites prepared using supercritical carbon dioxide ($scCO_2$) are forcibly blended, their thermal stability will become a problem when they are in actual use or processing. However, thermal stability of these composites has not been evaluated to date. In this chapter, the author studied the thermal stability of polymer composites prepared in $scCO_2$ using an isotactic polypropylene/poly(methyl methacrylate) (iPP/PMMA) composite. So the iPP/PMMA composite was selected, it facilitates analysis because of the glass transition temperature of iPP ($T_{g,\mathrm{iPP}}$) < the glass transition temperature of PMMA ($T_{g,\mathrm{PMMA}}$) < the temperature of iPP crystal melting ($T_{m,\mathrm{iPP}}$). The annealing temperature could be selected between $T_{g,\mathrm{iPP}}$ and $T_{g,\mathrm{PMMA}}$, and $T_{g,\mathrm{PMMA}}$ and $T_{m,\mathrm{iPP}}$, at which the chain mobility of iPP and PMMA will be divided easily. (The $T_{g,\mathrm{iPP}}$ $T_{g,\mathrm{PMMA}}$ and $T_{m,\mathrm{iPP}}$ can be obtained from figure 4-1.) Moreover, the microstructure, crystallinity, thermal behavior, and mechanical properties of iPP/PMMA composite have been discussed in chapter 3. PMMA is generated in the amorphous region between the crystalline lamellae of iPP, and doesn't affect the crystallinity of iPP. The iPP and PMMA are blended at the nanometer level and achieved thermodynamic miscibility to some extent. Mechanical properties such as yield stress, fracture stress, strain, and viscoelasticity can be controlled by changing the mass gain of PMMA. The author annealed the iPP/PMMA composite at 140 °C and 190 °C for different period of times, and investigated the effect of annealing on microstructure by small-angle X-ray scatting (SAXS)

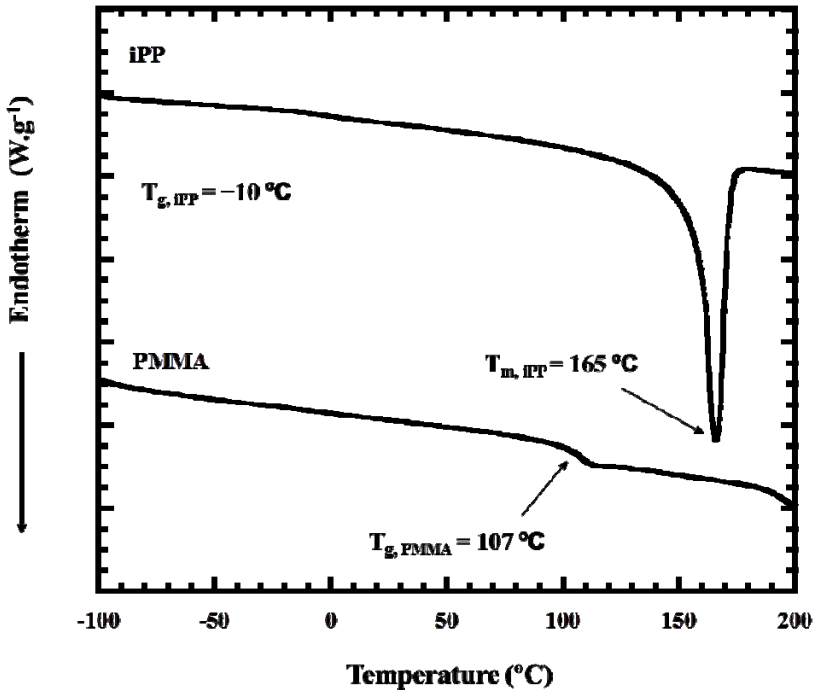

Figure 4-1 DSC thermograms of iPP and PMMA.

and transmission electron microscopy (TEM), crystallinity by wide-angle X-ray diffraction (WXRD), thermal behavior by differential scanning calorimetry (DSC), and mechanical properties by dynamic viscoelastic analyzer (DVA).

4.2 Experimental section

The iPP and iPP/PMMA composites with different mass gain of PMMA were annealed in a *vacuo* oven at 140 and 190 °C for 1, 5, 20 min. The accuracy of the *vacuo* oven was ± 2 °C. When the required annealing time was reached, the samples were quickly removed from the *vacuo* oven and quenched in ice water for 1 min. And then these samples were stored at ambient temperature. For comparison, original iPP was also annealed at 140 and 190 °C for 1, 5, 20 min.

4.3 Results and discussion

4.3.1 Annealing at 140 °C

The effect of annealing on microstructure was investigated by SAXS measurement. Figure 4-2, 4-3, 4-4 plot the scattering data in the form of the Lorenz-corrected SAXS intensity, Iq^2, versus the scattering vector, q, where I is the scattering intensity and q is defined by

$$q = \frac{4\pi}{\lambda}\sin\frac{\theta}{2} \quad (1)$$

where λ is the wavelength of the X-ray, and θ is the scattering angle. The iPP sample shows an obvious first-order peak, which is assigned to the long period corresponding to the sum of thickness of a crystalline layer, iPPc, and an amorphous layer, iPPa, in semicrystalline lamellae. The Bragg spacing was estimated from the maximum q^* using the relation $d_1 = 2\pi/q^*$. The magnitude, d_1, of 143 Å for iPP, estimated from $q^* = 0.439$ Å^{-1}, is comparable with the reported value of 153 Å [1]. In the iPP/PMMA composite, the SAXS profiles gradually change with increases in the mass gain of PMMA: A new reflection appears in a q range around 0.02 Å^{-1}, which corresponds to a dimension of ~314 Å. This is because MMA and AIBN, dissolved in $scCO_2$, are impregnated into the amorphous phase of iPP and subsequently polymerized *in situ* to form new phases consisting of polymerized PMMA

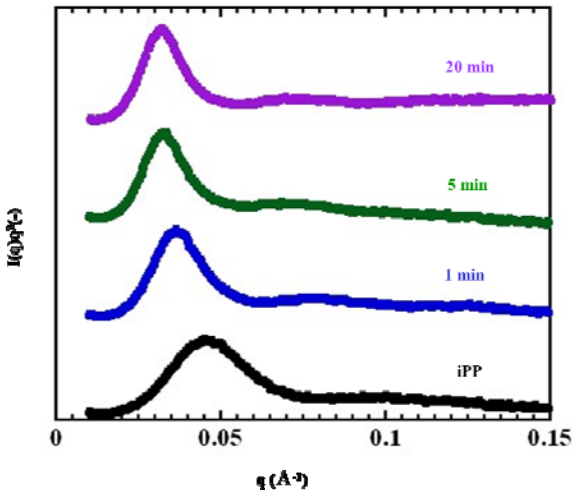

Figure 4-2 Lorentz-corrected SAXS plofiles of iPP and iPP annealed at 140 °C for 1, 5, 20 min.

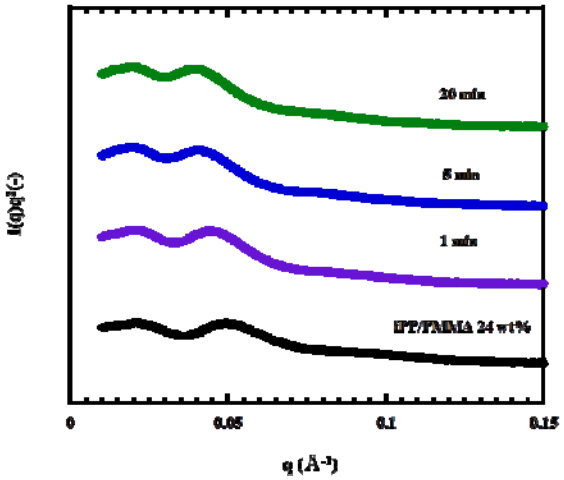

Figure 4-3 Lorentz-corrected SAXS plofiles of iPP/PMMA 24 wt% and iPP/PMMA 24 wt% annealed at 140°C for 1, 5, 20 min.

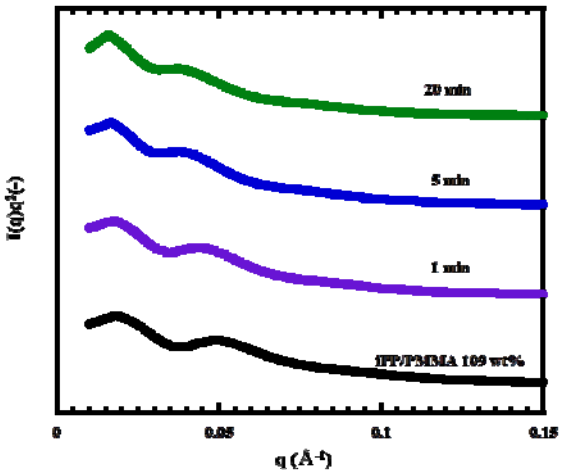

Figure 4-4 Lorentz-corrected SAXS plofiles of iPP/PMMA 24 wt% and iPP/PMMA 109 wt% annealed at 140 °C for 1, 5, 20 min.

embedded in amorphous phases of iPP. The existence of original iPP's long period in iPP/PMMA composite means that some structures of rest of the amorphous phases and crystalline phases of iPP are unchanged or only slightly modified. With an increase in the mass gain of PMMA, the intensity of the first-order reflection tends to become weaker, and the intensity of the first-order reflection tends to become stronger. This implies that the unchanged or only slightly modified amorphous phases of iPP becomes less and less.

First-order peak is also observed in the iPP that were annealed at 140 °C for different times. However, it tends to shift to a smaller q with increases in the annealing time, corresponding to a larger long period. Moreover, the peak of iPP annealed at 140 °C become much sharper. These results imply that the crystal growth of iPP happens with annealing at 140 °C and the iPPc becomes thicker. In the iPP/PMMA composite, the new reflection peak is also observed to shift to a smaller q with increases in the annealing time, besides the shift of peak from original iPP's long period. The difference is that the shift of peak from original iPP's long period is much easier than that of new reflection peak. This indicates the existence of PMMA is not conducive to the increases of iPPc's thinkness. These results also illustrate the nano-structure can be maintained when the iPP/PMMA composites are annealed at 140 °C.

Figures 4-5, 4-6 and 4-7 show the DSC thermograms of iPP, iPP/PMMA composites, and them annealed at 140 °C for 1, 5, 20 min. The main melting temperature is always close to 165 °C. The shapes of the endotherm of the untreated samples seem to be simple, but, after

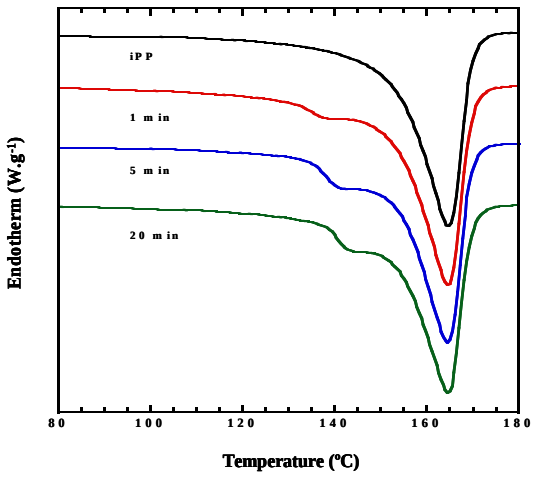

Figure 4-5 DSC thermograms of iPP, and iPP annealed at 140 °C for 1, 5, 20 min.

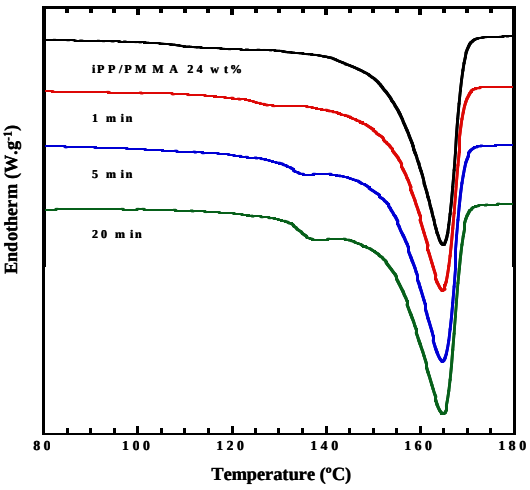

Fig 4-6 DSC thermograms of iPP/PMMA 24 wt%, and iPP/PMMA 24 wt% annealed at 140 for 1, 5, 20 min.

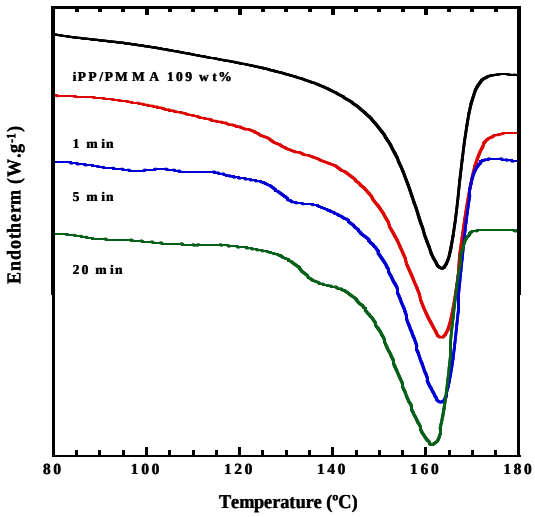

Figure 4-7 DSC thermograms of iPP/PMMA 109 wt%, and iPP/PMMA annealed at 140 °C for 1, 5, 20 min.

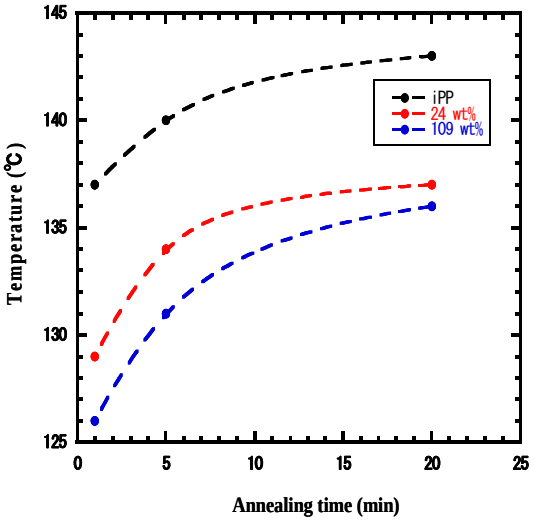

Figure 4-8 Relation between the top temperature of small crystals and annealing time at 140 °C .

annealing, some shoulders appear on the lower temperature side, indicating small crystals were generated by the heat treatment [2-4]. With increasing the annealing time, the shoulders shift to a higher temperature, due to the small crystal growth. The top melting temperatures of small crystal were shown in figure 4-8. A lower top melting temperature is observed with an increase in the mass gain of PMMA. The top melting temperature corresponds to the size of small crystal, meaning the size of small crystal is smaller in the iPP/PMMA composite with a high mass gain of PMMA when these composites are annealed at 140 °C. This is because the free volume is relative narrow in the iPP/PMMA composite with a high mass gain of PMMA, the new generated small crystals exclude mutually, leading to a small size of small crystal.

Figures 4-9, 4-10, 4-11 show the WXRD patterns of iPP, iPP/PMMA composites, and them annealed at 140 °C for 1, 5, 20 min. The results on untreated samples and all annealed samples exhibit only the monoclinic α form of iPP [5-8]. However, some changes such as relative intensities of peaks and a better separation between 111 and 041 peaks are also observed. These derive from the thermodynamic molecular motion ability of iPP molecular chain. Percent crystallinity in iPP, X_{iPP}, was calculated as follows:

$$X_{iPP}\,(\%) = \frac{X_{iPP/PMMA}}{W_{iPP}} \qquad (2)$$

where X_{iPP} is the crystallinity of iPP/PMMA composite assumed to be dependent only on the crystalline regions of iPP, $X_{iPP/PMMA}$ is the crystallinity of the iPP/PMMA composite, and W_{iPP} is the weight fraction of iPP. Figure 4-12 shows the variation of crystallinity versus the

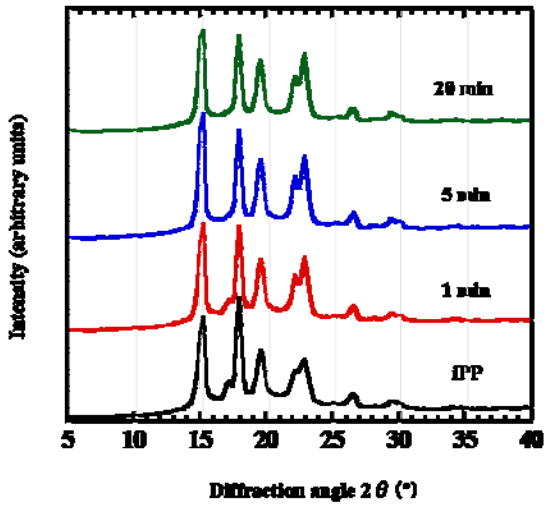

Figure 4-9 WXRD patterns of iPP and iPP annealed at 140 °C for 1, 5, 20 min.

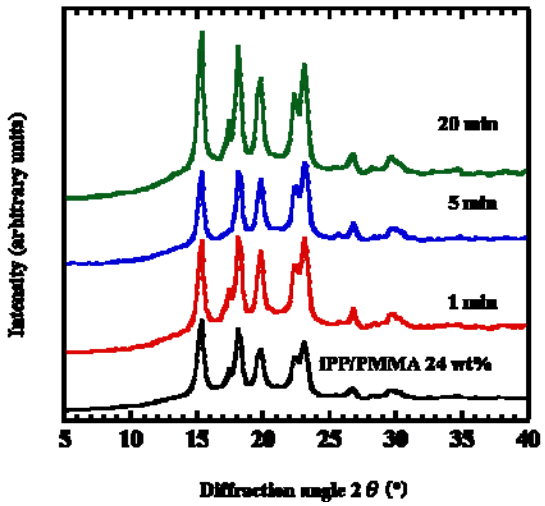

Figure 4-10 WXRD patterns of iPP/PMMA 24wt%, and iPP/PMMA 24 wt% annealed at 140 °C for 1, 5, 20min.

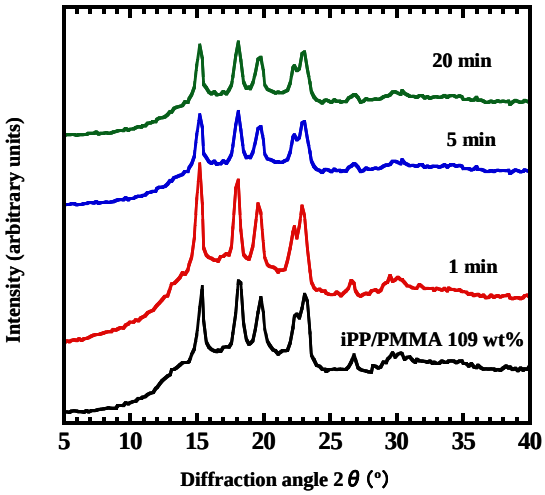

Figure 4-11 WXRD patterns of iPP/PMMA 24wt%, and iPP/PMMA 24 wt% annealed at 140 °C for 1, 5, 20 min.

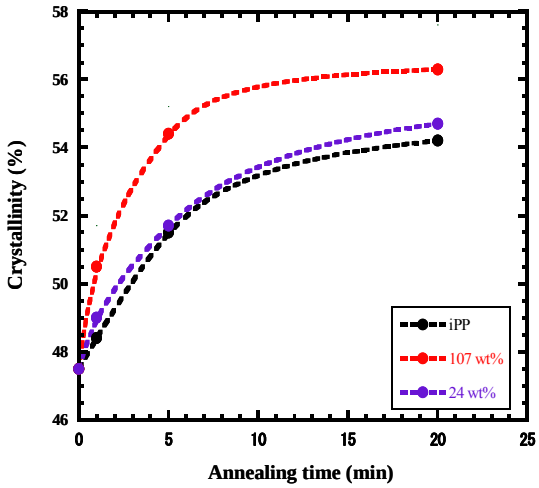

Figure 4-12 Relation between crystallinity and annealing time at 140 °C.

annealing time at 140 °C. The crystallinity rapidly increases in correlation with annealing time in 5 min, and then tends to slow. As it was predicted and expected that crystallization is assisted at the interface [9-12], because the more interfaces are formed with an increase in the mass gain of PMMA, the crystallization rate is in proportion to the mass gain of PMMA.

4.3.2 Annealing at 190 °C

Figures 4-13, 4-14 and 4-15 show the Lorentz-corrected SAXS profiles of original iPP, iPP/PMMA composites, and them annealed at 140 °C for 1, 5, 20 min. The first-order peak from long period is observed in the iPP that were annealed at 190 °C for different times. It tends to shift to a larger q with increases in the annealing time, corresponding to a smaller long period. Moreover, the peak of iPP annealed at 190 °C become much broader. A possible reason is that when iPP is annealed at 190 °C, the crystal melts, and the amorphous chains entangle mutually, so that the crystallization becomes difficult in the quenching process.

In the iPP/PMMA composites with mass gain of PMMA 24 wt% and 109 wt%, after annealing at 190 °C for 1 min, the new reflection peaks disappear, instead, the scattering

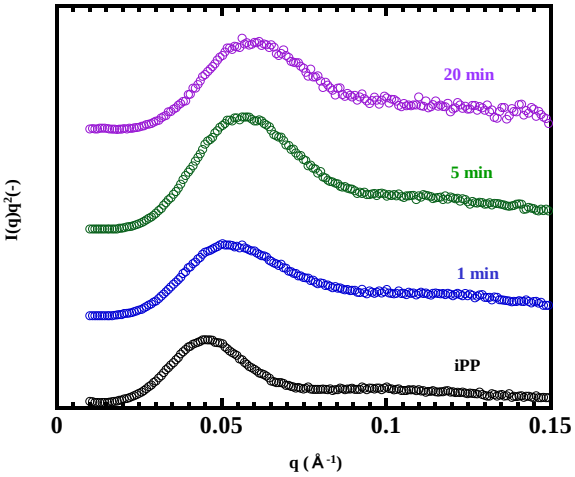

Figure 13 Lorentz-corrected SAXS plofiles of iPP and iPP annealed at 190°C for 1, 5, 20 min.

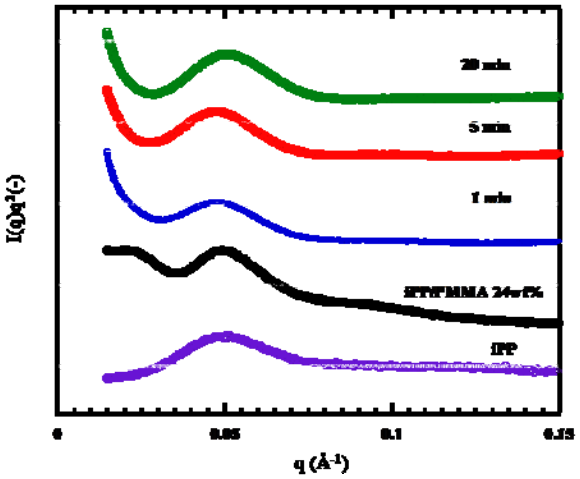

Fig 4- 14 Lorentz-corrected SAXS plofiles of iPP, iPP/PMMA composite 24wt% and iPP/PMMA composite 24wt%annealed at 190°C for 1, 5, 20 min.

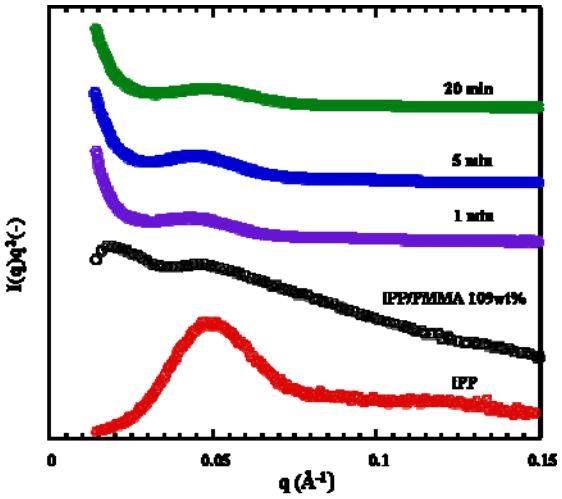

Figure 4-15 Lorentz-corrected SAXS plofiles of iPP, iPP/PMMA composite 109wt% and iPP/PMMA composite 109wt% annealed at 190°C for 1, 5, 20 min.

intensity for a q smaller than 0.015 $Å^{-1}$ tends to increase as q decreases, which indicates the presence of large domains. When the iPP/PMMA composite was annealed at a temperature higher than $T_{m,iPP}$, PMMA was considered to have migrated by diffusion from the amorphous region of iPP and a macroscopic domain structure was formed. Moreover, as same as in iPP, the first-order peak showed a tendency to shift to a larger q with increases

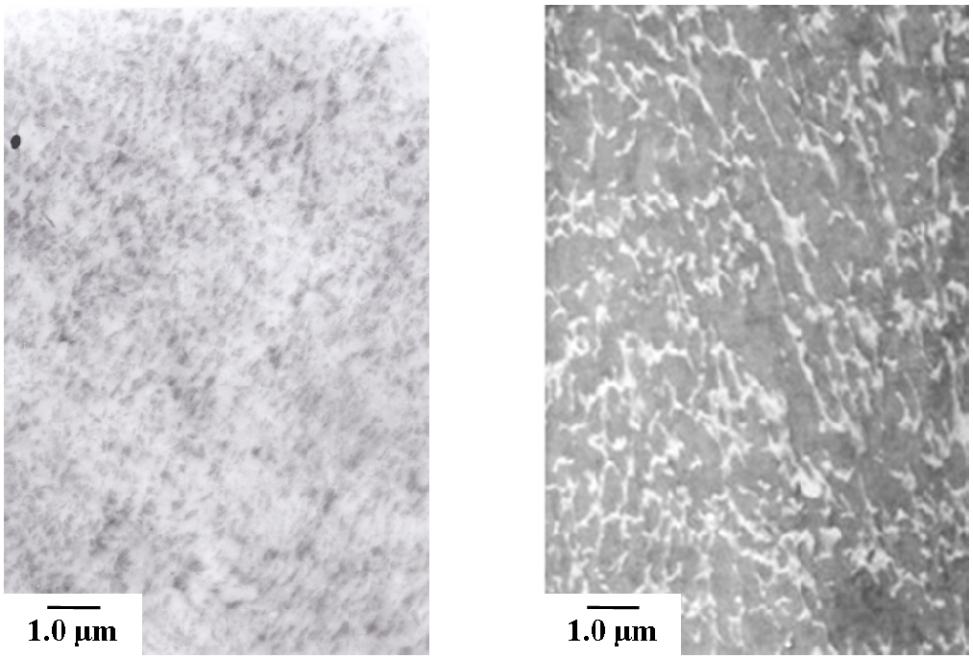

Figure 4-16 TEM images of iPP/PMMA 109 wt% (a) and iPP/PMMA 109 wt% annealed at 190 for 1min (b).

in the annealing time. Transmission images confirmed the SAXS data as shown in figure 4-16. The dark and light portions in the micrographs are due to iPP and PMMA domains, respectively. In the iPP/PMMA composite with a mass gain of 109 wt%, the PMMA domains are finely dispersed within the iPP substrate on a nanometer scale and the phase

boundary was ambiguous. Conversely, in the iPP/PMMA composite with a mass gain of 109 wt% annealed at 190 °C for 1 min, PMMA domains of micron scale were formed in the iPP substrate and the phase boundary was clear. These results indicate that when the iPP/PMMA composite was annealed at 190 °C, a macroscopic domain structure was formed, and the nano-structure could be remained.

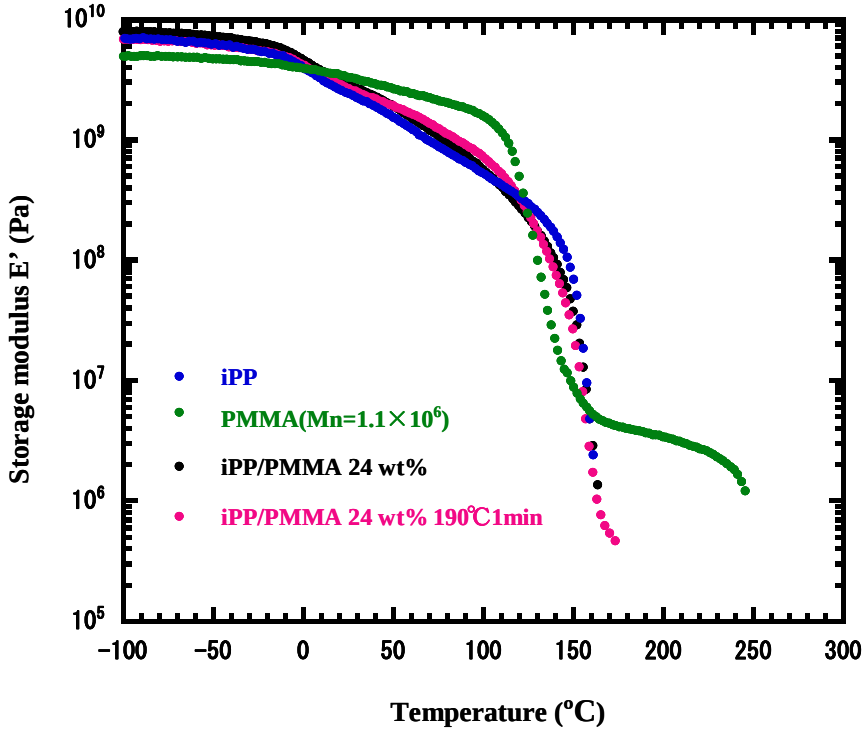

Figure 4-17 Temperature dispersion curves of the storage modulus (E') for iPP, PMMA, iPP/PMMA composite 24 wt%, and iPP/PMMA composite 24 wt% annealed at 190 °C for 1min.

The results of DVA are in accord with SAXS and TEM data. In figure 4-17, 4-18, the results for DVA are represented as a function of temperature for original iPP, iPP/PMMA composites, and them annealed at 190 °C for 1 min. The temperature dependencies of the storage modulus (E') of iPP alone show features characteristic of a semicrystalline polymer: a slow decrease in E' throughout the temperature region between -20 and 165 °C.

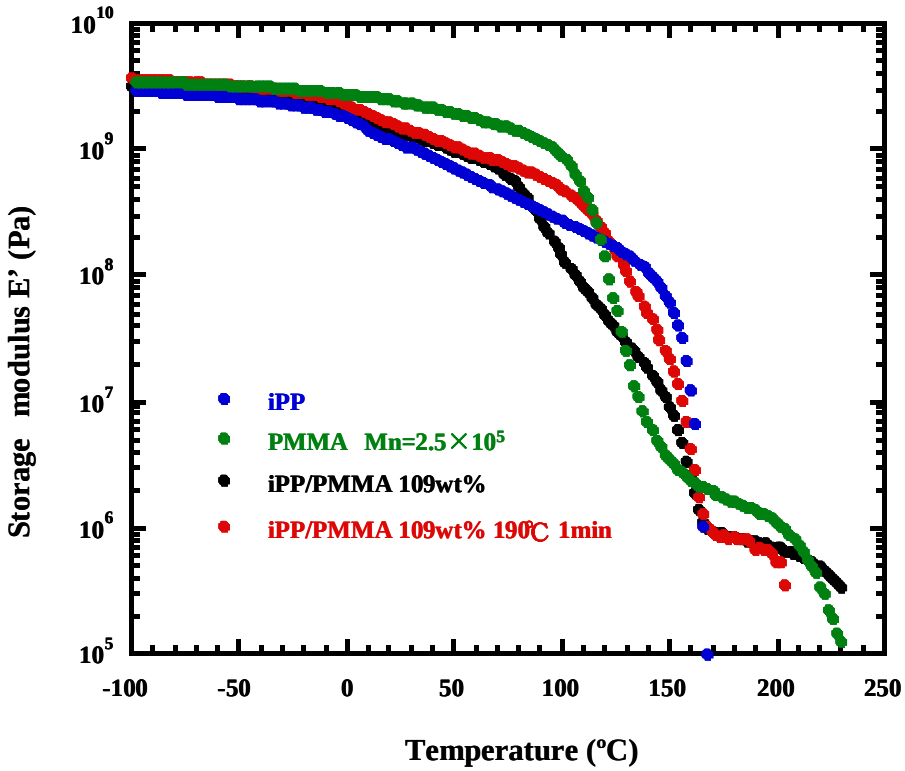

Figure 4-18 Temperature dispersion curves of the storage modulus (E') for iPP, PMMA, iPP/PMMA composite 109 wt%, and iPP/PMMA composite 109 wt% annealed at 190 °C for 1min.

At T ≈ 165 °C, the crystalline phase of iPP melts, which is seen as a marked decrease in the modulus. In the iPP/PMMA composites, with increasing mass of PMMA, new plateaus appeared, and the melting break temperature shifted to a higher temperature. After annealing at 190 °C for 5 min, the iPP/PMMA composites showed a poor storage modulus, indicating the macroscopic domain structure was formed.

4. 4 Conclusions

In summary, we have evaluated the thermal stability of iPP/PMMA composite using $scCO_2$. When the iPP/PMMA composites were annealed at 140 °C, although iPP crystal grew, the nano-structure remained. When the iPP/PMMA composites were annealed at 190 °C, PMMA migrated by diffusion from the amorphous region of iPP, then macroscopic domain structure was formed, and the nanostructure cannot be remained.

4.5 References

[1] A. R. Berens, G. S. Huvard, R. W. Korsmeyer, F. W. Kunig, *J. Appl. Polym. Sci.* **1992**, 46, 231.

[2] W. J. O'Kane, R. J. Young, A. J. Ryan, W. Bras, G. E. Derbyshire, G. R. Mant, *Polymer* **1994**, *35*, 1352.

[3] L. Poussiin, Y. A. Bertin, J. Parisot, C. Brassy, *Polymer* **1998**, *39*, 4261.

[4] T. Hoshi, T. Sawaguchi, R. Matsuno, T. Konno, M. Takai, K. Ishihara, *J. Supercritical Fluids* **2008**, *44*, 391.

[5] D. Ferrer-Balas, M. L. Maspoch, A. B. Martinez, O. O. Santana, *Polymer* **2001**, *42*, 1697.

[6] R. Seguela, E. Staniek, B. Escaig, B. Fillon, *J. Appl. Polym. Sci.* **1999**, *71*, 1873.

[7] G. Natta, P. Corradini, *Nuovo Cimento, Suppl.* **1960**, *15*, 40.

[8] G. Natta, M. Peraldo, P. Corradini, *Rand. Accad. Naz. Lincei* **1959**, *26*, 14.

[9] W. Shi, F. Chen, Y. Zhang, C. C. Han, *ACS Macro Lett.* **2012**, *1*, 1086.

[10] X. Zhang, Z. Wang, X. Dong, C. C. Han, *J. Chem. Phys.* **2006**, *125*, 024907(1-10).

[11] M. K. Mitra, M. Muthukumar, *J. Chem. Phys.* **2010**, *132*, 184908(1-6).

[12] Y. Ma, L. Zha, W. Hu, G. Reiter, C. C. Han, *Phys. Rev. E* **2008**, *77*, 061801(1-5).

Chapter 5

Preparation of Linear Low-Density Polyethylene/ Poly(methyl methacrylate) Composite using Supercritical Carbon Dioxide

Table of Contents

Chapter 5

Preparation of Linear Low-Density Polyethylene/ Poly(methyl methacrylate) Composite using Supercritical Carbon Dioxide

5.1 Introduction

Phase dispersion crosslinking synergism, or synthesis of interpenetrating polymer networks (IPNs) is an effective method for improving the properties of polymeric materials. Several groups have prepared semi-IPNs using supercritical carbon dioxide ($scCO_2$). Han et al. showed that semi-IPNs of crosslinked poly(methyl methacrylate) (PMMA) within a silicone rubber matrix and crosslinked PS in a polypropylene matrix could be prepared in $scCO_2$ [1,2]. Howdle et al. prepared semi-IPNs of ultra-high-molecular-weight polyethylene (UHMWPE) with PMMA-co-poly(ethylene glycol) dimethacrylate (PEGDMA) through $scCO_2$ facilitated impregnation of MMA and ethylene glycol dimethacrylate (EGDMA) monomers into UHMWPE, and this composite remains mechanically strong even at temperatures above the melting temperature (T_m) of UHMWPE [3]. These composites have all been extended to the preparation of semi-IPNs by incorporating crosslinking agents or IPNs if the substrate is a crosslinked polymer.

In previous studies, LLDPE/PMMA composites were prepared using different compatibilizers but these composites display phase separation on the micron scale and do not offer desirable mechanical properties [4-6]. In chapter 5, the author describes the preparation of linear low-density polyethylene (LLDPE)/PMMA pseudo-IPNs using $scCO_2$ as a swelling agent, where the term “pseudo-IPNs” is used because there is no real

chemical crosslinking in LLDPE/PMMA composites. The pseudo-IPNs were formed by the complicated entanglement of the amorphous chain of LLDPE and PMMA chains through controlling the mass gain of PMMA using $scCO_2$, a technique not found in a literature survey. This work aimed to: (1) prepare LLDPE/PMMA pseudo-IPNs with nanometer dispersion; (2) prove the formation of LLDPE/PMMA pseudo-IPNs; (3) study the features of the pseudo-IPNs using $scCO_2$.

The author investigated the microstructure of LLDPE/PMMA pseudo-IPNs by small-angle X-ray scattering (SAXS). The crystallinity of the composite was investigated by wide-angle X-ray diffraction (WXRD) and differential scanning calorimetry (DSC). The mechanical properties of the composite were analyzed by means of dynamic viscoelastic analysis (DVA) and tensile tests. The molecular weight of PMMA was determined by gel permeation chromatograph (GPC).

5.2 Experimental Section

The LLDPE substrate, MMA monomer (2 g), and AIBN initiator (0.03 g) were placed in the vessel, which was then sealed. The vessel was then flushed by CO_2 at atmospheric pressure. After the system reached thermal equilibrium (40 °C), the vessel was pressurized a specific CO_2 pressure using a CO_2 delivery pump. The LLDPE substrate was soaked for 1 h. The vessel was then pressurized to the last specific pressure heated to the reaction temperature (80 °C), and held for 24 h to ensure that the polymerization of MMA was complete. The vessel was then cooled to 10 °C and gradually returned to ambient pressure. After extracting the unreacted reagents and the surface PMMA from the sample with acetone for 24 h on a Soxhlet extractor, the LLDPE/PMMA composite was dried in *vacuo* at room temperature.

5.3 Results and Discussion

5.3.1 Preparation of LLDPE/PMMA composite in $scCO_2$

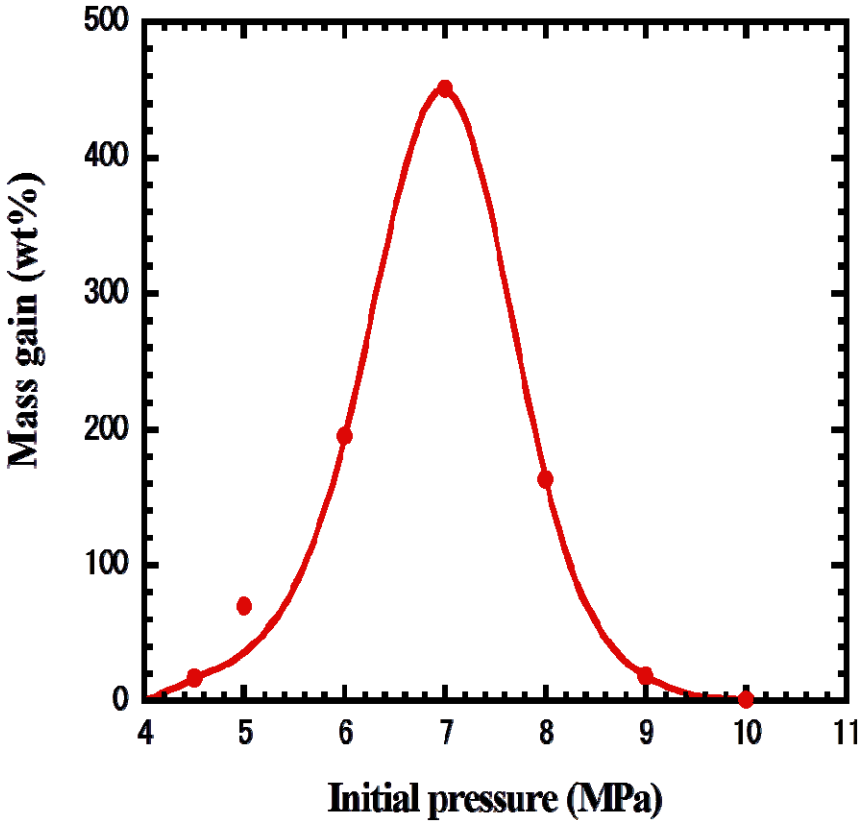

Figure 5-1 Effect of initial pressure on the mass gain of PMMA into LLDPE after polymerization.

Figure 5-1 shows the effect of the initial pressure of CO_2 on the mass gain of PMMA into the LLDPE substrate after polymerization. The mass gain initially increases in correlation with the initial pressure, reaching a maximum of 450 wt% when the initial

pressure of CO_2 is about 7 MPa, and then decreases with further increases in the initial pressure. Therefore, the mass gain of the PMMA sample can be controlled by modulating the initial pressure of CO_2.

$ScCO_2$ is a good swelling agent and generally a poor solvent for most polymers. Impregnation of $scCO_2$ starts on the surface of the substrate followed by gradual permeation into the inner substrate. The swelling kinetics of CO_2 into the polymer matrix depends on both the temperature and pressure [7,8]. Differing from other polymers, PMMA possesses the swelling properties in CO_2 that depend on the temperature and pressure [9]. When the initial pressure of CO_2 is low, both the solubility of MMA and the swelling of the amorphous LLDPE region are low, resulting in insufficient generation of PMMA in the LLDPE substrate. An increase in the initial pressure results in improved solubility of MMA, and swelling of the amorphous LLDPE region, which results in an increase in the mass gain with higher initial pressures. However, the partition coefficient of MMA in CO_2 becomes larger than that in LLDPE substrate at even higher pressures. Additionally, at high pressure, the rate of the decomposition of AIBN is relatively slow [10,11]. A combination of these factors explains the mass gain decreases with increasing initial pressures over 7 MPa.

5.3.2 Microstructure analyses of the LLDPE/PMMA composite

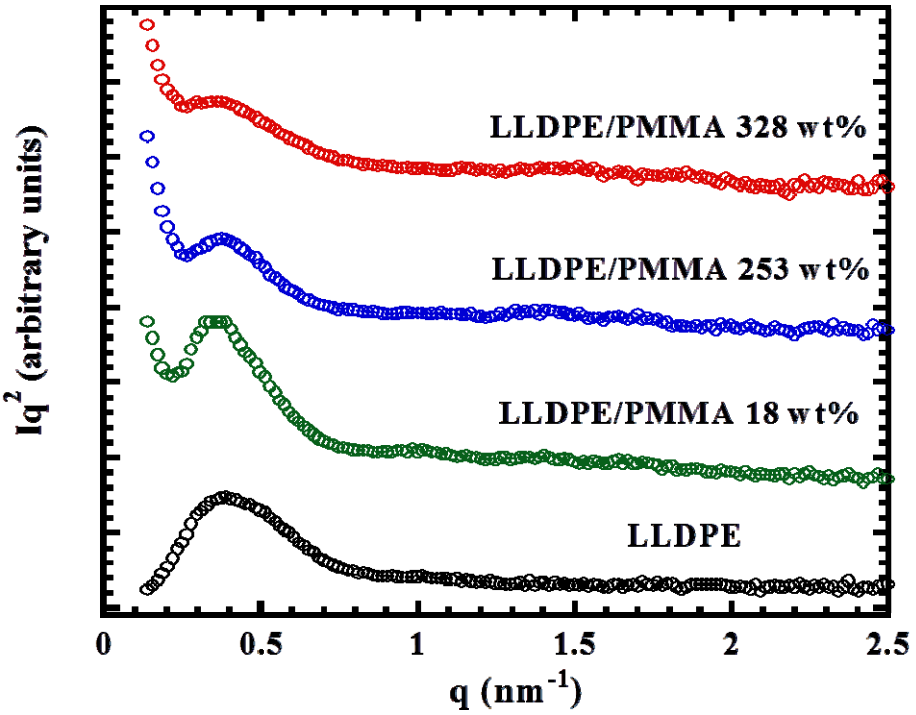

Figure 5-2 Lorentz-corrected small-angle X-ray scattering plofiles of LLDPE and LLDPE/PMMA composite.

SAXS is a powerful tool for probing the detailed microstructure of semicrystalline/amorphous composites [12,13]. The morphological parameters in the lamellar level, such as the long period, can be deduced from the one-dimensional correlation function or the interphase distribution function. Figure 5-2 shows the Lorentz-corrected SAXS profiles of original LLDPE and LLDPE/PMMA composites. In the original LLDPE, the scattering vector q of the peak top was 0.390 nm^{-1} (calculated 16.1 nm Bragg spacing). This peak was due to the long period of the lamellar structure [14,15].

In the LLDPE/PMMA composite, enhanced scattering intensity was observed through the lower scattering vector q ($q < 0.3$ nm^{-1}), while the peak from the long period of LLDPE became progressively weaker with increasing mass of PMMA. This enhanced scattering intensity was not observed for the original LLDPE. The enhanced scattering intensity of the LLDPE/PMMA composite depended on the mass gain, which is consistent with the generation of small-angle scattering from extensive disruption of the crystalline layer upon incorporation of PMMA into the polymer composites.

5.3.3 Crystallinity of the LLDPE/PMMA composite

Figure 5-3 shows the WXRD patterns of LLDPE and LLDPE/PMMA composites. It can be seen that the WXRD patterns of both the LLDPE and LLDPE/PMMA composite present the characteristic peaks for the (110), (200) planes [16]. The angular positions of the diffraction peaks of the crystalline LLDPE are almost identical for original LLDPE substrate and for the LLDPE/PMMA composite, indicating that the crystal forms are not changed upon the addition of PMMA. However, the amorphous regions of the LLDPE/PMMA composite increased with the mass gain of PMMA, which indicates that the overall crystallinity decreases with increases in the mass gain of PMMA (Figure 5-4).

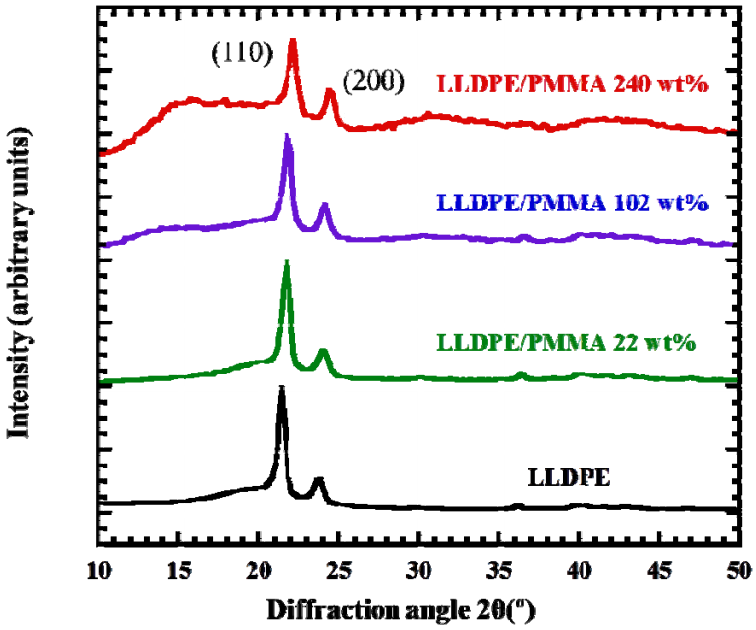

Figure 5-3 WXRD patterns of LLDPE, and LLDPE/PMMA composites.

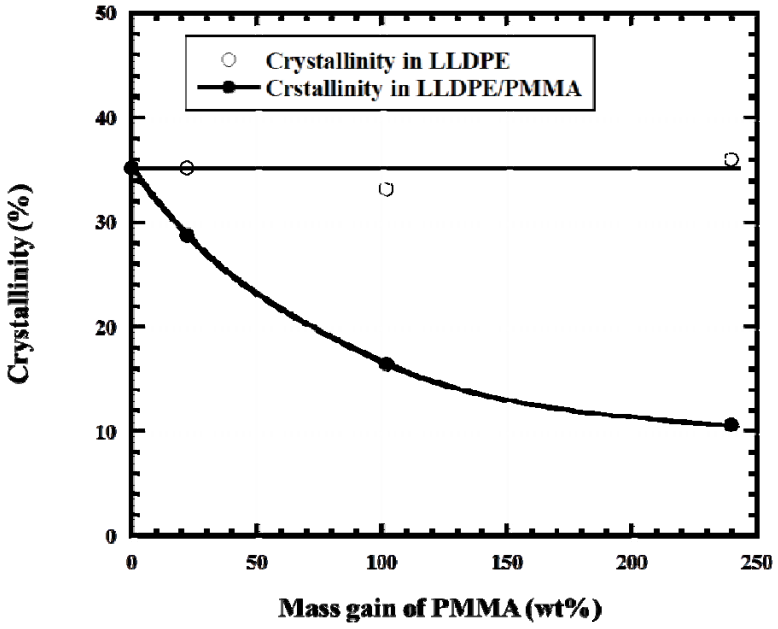

Figure 5-4 Relationship between crystallinity and mass gain of PMMA.

The reduction in sample crystallinity is due to dilution as a result of the addition of PMMA to the amorphous LLDPE regions, and the resultant increase in the size of the amorphous regions. Percent crystallinity in LLDPE, X_{LLDPE}, was calculated as follows:

$$X_{LLDPE}\,(\%) = \frac{X_{LLDPE/PMMA}}{W_{LLDPE}} \qquad (2)$$

where X_{LLDPE} is the crystallinity of LLDPE/PMMA composite assumed to be dependent only on the crystalline regions of LLDPE, $X_{LLDPE/PMMA}$ is the crystallinity of the LLDPE/PMMA composite, and W_{LLDPE} is the weight fraction of LLDPE. X_{LLDPE} does not change, although $X_{LLDPE/PMMA}$ decreases according to an increase in the mass gain of PMMA. The total amount of crystalline LLDPE remains unchanged. These results indicate that the MMA polymerizes solely within the amorphous regions of the polymer.

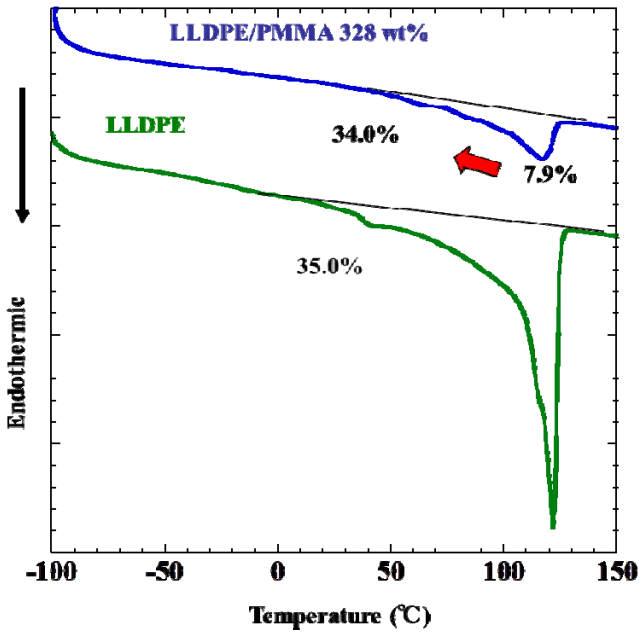

Figure 5-5 DSC thermograms of LLDPE, LLDPE/PMMA composite 328wt%.

Differential scanning calorimetry, shown in Figure 5-5, confirmed the WAXD data. In LLDPE/PMMA composites, strong LLDPE melting endotherms were observed. The melting endotherms reveal that the composite preparation does not affect the crystalline region of the LLDPE substrate. Further, the melting endotherm peaks became broad and shallow with increasing mass gain of PMMA. This is due entirely to dilution of the crystalline regions by the addition of PMMA to amorphous LLDPE regions.

5.3.4 Mechanical properties of the LLDPE/PMMA composite

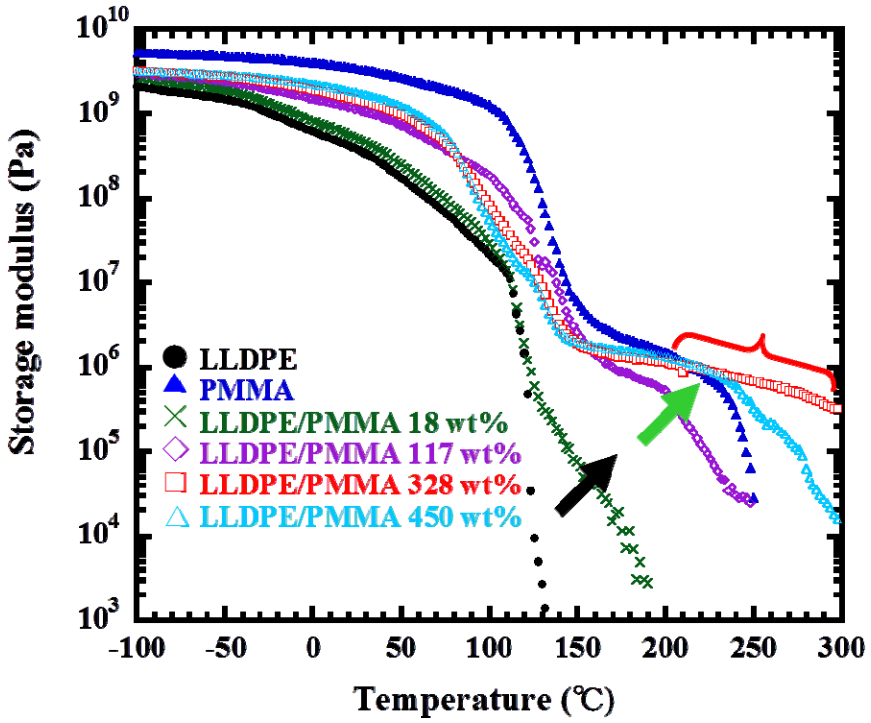

Figure 5-6 Temperature dispersion curves of the storage modulus (E').

DVA is a sensitive technique that measures the mechanical response of materials by monitoring property changes with respect to temperature and/or frequency of oscillation. In Figure 5-6, the results for DVA are represented as a function of temperature for original LLDPE and LLDPE/PMMA composites. The temperature dependencies of the storage modulus (E') of LLDPE alone show features characteristic of a semicrystalline polymer: a slow decrease in E' throughout the temperature region between -20 and 120 °C. At T ≈ 120 °C, the crystalline phase of LLDPE melts, which is seen as a marked decrease in the modulus. In the LLDPE/PMMA composites, with increasing mass of PMMA, new plateaus appeared, and the melting break temperature shifted to a higher temperature. In particular, the LLDPE/PMMA composite at 328 wt% shows a remarkable plateau that extends to 300 °C. We attribute these plateaus to the formation of pseudo-IPNs by a complicated entanglement of the amorphous chain of LLDPE and PMMA chains. The detailed reason will be explained in 5.3.5.

Table 5-1 lists the results of the tensile test at 20 °C. In the solution blend, a macro-phase separation was induced because LLDPE and PMMA are immiscible. The conversion of the sample to a macro-phase separated structure was usually had a deleterious effect on its mechanical properties. However, the yield stress of the LLDPE/PMMA composites is considerably higher than that of LLDPE. Further, it increased gradually with the mass gain of PMMA. The fracture stress of the

LLDPE/PMMA composites is also improved as compared to that of LLDPE. In addition, the fracture strain decreased rapidly with the mass gain of PMMA. Therefore, nanometer-sized PMMA generated in the amorphous regions significantly affected the mechanical properties of LLDPE/PMMA composite, which can be controlled through the mass gain of PMMA.

Table 5-1 Stress and strain of LLDPE/PMMA disperse system.

	Yield Stress(MPa)	Fracture Stress(MPa)	Fracture Strain(%)
LLDPE	7.4	8.7	776
LLDPE:PMMA=100:18	10.8	9.8	740
LLDPE:PMMA=100:34	9.2	9.3	666
LLDPE:PMMA=100:44	15.6	14.7	175
LLDPE:PMMA=100:117	23.0	21.0	21
LLDPE:PMMA=100:126	—	26.5	12
LLDPE:PMMA=100:227	—	31.5	10
PMMA	—	42.0	3
Solution Blend(LLDPE:PMMA=100:100)	—	7.3	2

(Gauge length:10mm, Cross-head speed:10mm/min, Measured at 21℃)

5.3.5 Thermodynamic miscibility and thermal stability of LLDPE/PMMA pseudo-IPNs

In figure 5-6, some new plateaus appeared with increasing mass of PMMA. We attribute these plateaus to the formation of pseudo-IPNs by a complicated entanglement of the amorphous chain of LLDPE and PMMA chains. To support this explanation, some doubts must be solved:

1) Whether these new plateaus are from PMMA?

2) Whether crosslinking of MMA or reaction between MMA and LLDPE happened?

3) How are the thermodynamic miscibility and thermal stability of pseudo-IPNs?

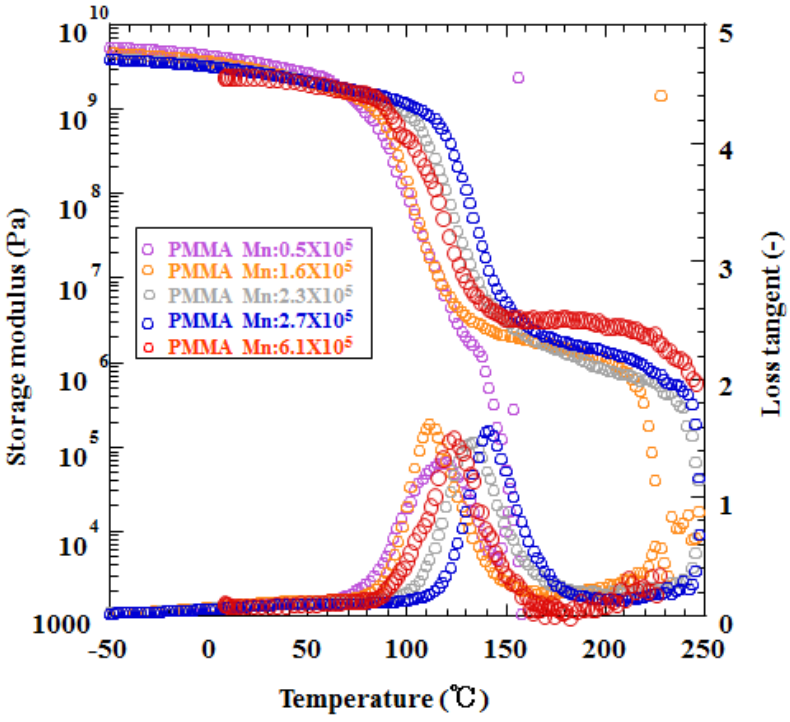

Figure 5-7 DVA curves of different molecular weight of PMMA.

Figure 5-7 show the DVA curves of different molecular weight of PMMA. In PMMA with M_n = 0.5×10^4, the break appears at about 120 °C. With increasing the molecular weight of PMMA, new plateaus appeared, and the break temperature shifted to a higher temperature. These plateaus are from the entanglement of amorphous chain of PMMA. However, when the M_n is increased to 20×10^4, the break temperatures collected at about 250 °C, and no further increase. This may be attributed to the saturation of the entanglement, namely, the maximal number of entanglement points achieved.

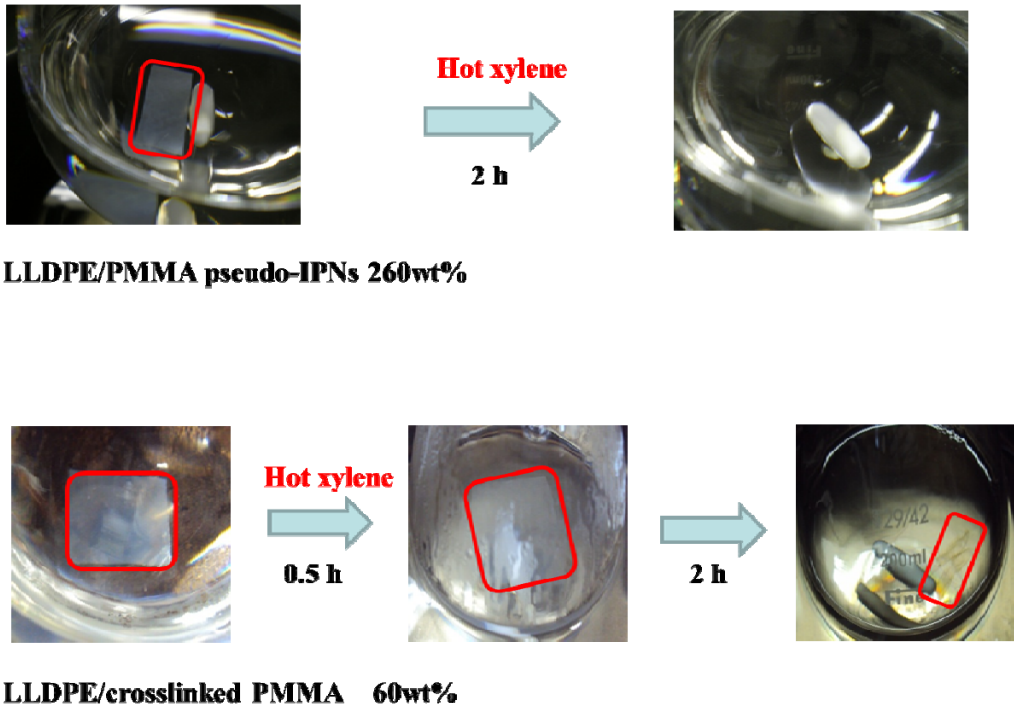

Figure 5-8 Pictures of swelling experiment of LLDPE/PMMA pseudo-IPNs and LLDPE/crosslinked PMMA.

In general, the plateaus in figure 5-6 are considered to be an effect of crosslinking, but no crosslinking agents were added and the polymer substrate was not crosslinked either. To further illustrate this point, we prepared a reference sample LLDPE/crosslinked PMMA using the same method, and then a swelling experiment was carried out. In figure 5-8, it is clearly seen that the LLDPE/PMMA pseudo-IPNs was dissolved in hot xylene after 2 h, and the LLDPE/crosslinked PMMA only swelled and wasn't dissolved in hot xylene. In addition, the molecular weight of LLDPE after DVA measurement was also the same as that of original LLDPE. These results illustrate no crosslinking took place in the preparation of LLDPE/PMMA pseudo-IPNs or any measurement.

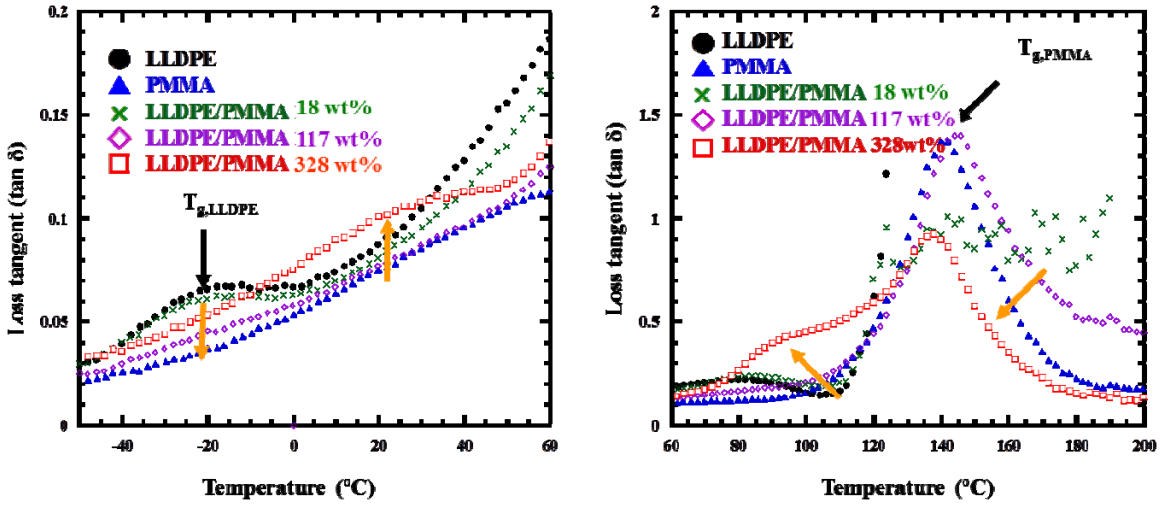

Figure 5-9 Temperature dispersion curves of the loss tangent (tan δ).

The thermodynamic miscibility of LLDPE and PMMA was evaluated by DVA. Figure 5-9 shows the temperature dispersion curves of the loss tangent (tan δ) for LLDPE, PMMA,

and the LLDPE/PMMA composites. For LLDPE, the α-relaxation peak appeared at ~ -20 °C corresponding to the T_g of the LLDPE amorphous chain ($T_{g,LLDPE}$). For PMMA, the α-relaxation peak appeared at ca. 140 °C, which corresponds to the T_g of the PMMA chain ($T_{g,PMMA}$). The LLDPE/PMMA composite showed the three peaks which correspond to $T_{g,LLDPE}$, $T_{g,PMMA}$ and the T_m of LLDPE ($T_{m,LLDPE}$). The two peaks corresponding to $T_{g,LLDPE}$ and $T_{g,PMMA}$ are shifted with respect to each other, with the $T_{g,LLDPE}$ peak shifted towards a higher temperature and the $T_{g,PMMA}$ peak shifted towards a lower temperature. Furthermore, the extent of the shifts increased with increasing mass of PMMA. These results imply that, using this method, the LLDPE and PMMA polymers were somewhat thermodynamically miscible [17].

The thermal stability of LLDPE/PMMA composites was evaluated by the following method. LLDPE/PMMA composites with different mass gains of PMMA were annealed at 170 °C for 5 min, and their microstructure and mechanical properties were investigated by SAXS and DVA methods, respectively. The results are shown in figure 5-10 and figure 5-11. After annealing at 170 °C for 5 min, a new peak was observed in the LLDPE/PMMA composite of 18 wt%, which derived from LLDPE. In contrast, the LLDPE/PMMA composite of 328 wt% showed almost no changes. The reason for this difference in behavior is that when the LLDPE/PMMA composite with a low mass gain of PMMA was

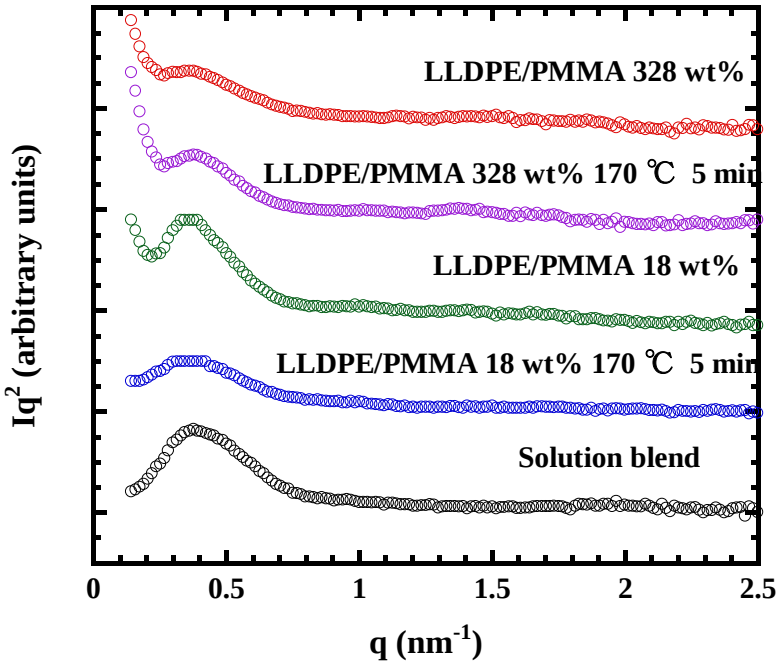

Figure 5-10 Lorentz-corrected small-angle X-ray scattering plofiles.

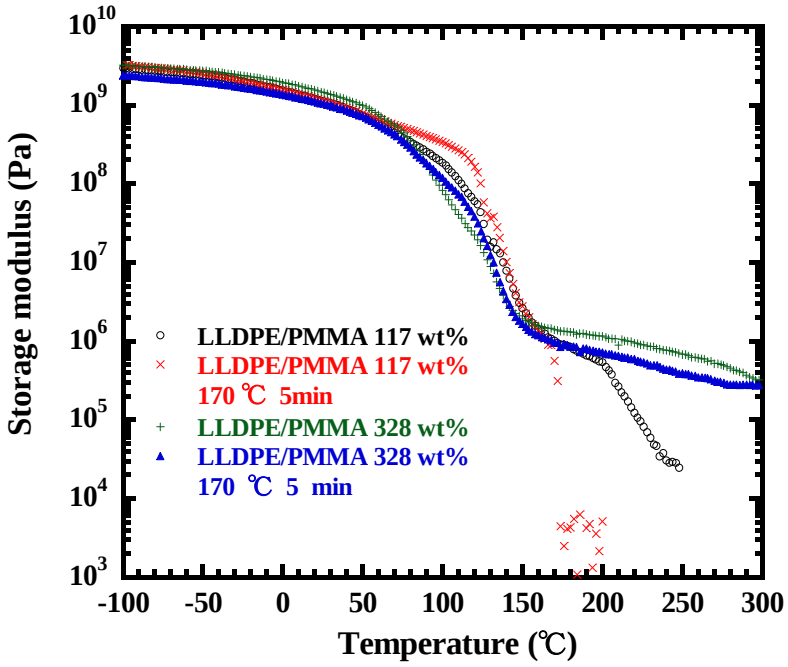

Figure 5-11 Temperature dispersion curves of the storage modulus (E').

annealed at a temperature higher than $T_{m,LLDPE}$, PMMA migrated by diffusion from the amorphous region of LLDPE and a macroscopic domain structure was formed. On the contrary, when the mass gain of PMMA was high, a complicated entanglement between PMMA and the amorphous chains of the lamellar structure was formed, so PMMA could not easily migrate by diffusion from the amorphous region of LLDPE. Therefore, the nano-structure of this composite was retained after annealing. The results of DVA are in accord with SAXS data. The LLDPE/PMMA composite at 18 wt% annealed at 170 °C was not studied because its melting break is below 170 °C. In contrast, the LLDPE/PMMA composite at 117 wt% could be used to evaluate the thermal stability. After annealing at 170 °C for 5 min, the LLDPE/PMMA composite at 117 wt% showed a poor storage modulus while there was almost no change in the LLDPE/PMMA composite at 328 wt%. To further confirm the thermal stability, a longer annealing time and different temperatures are necessary and this is the subject of ongoing investigations.

5.3.6 Formation mechanism of LLDPE/PMMA pseudo-IPNs

To explain the formation reason of LLDPE/PMMA pseudo-IPNs, the investigation of molecular weight of PMMA produced inside LLDPE is necessary. We found out the

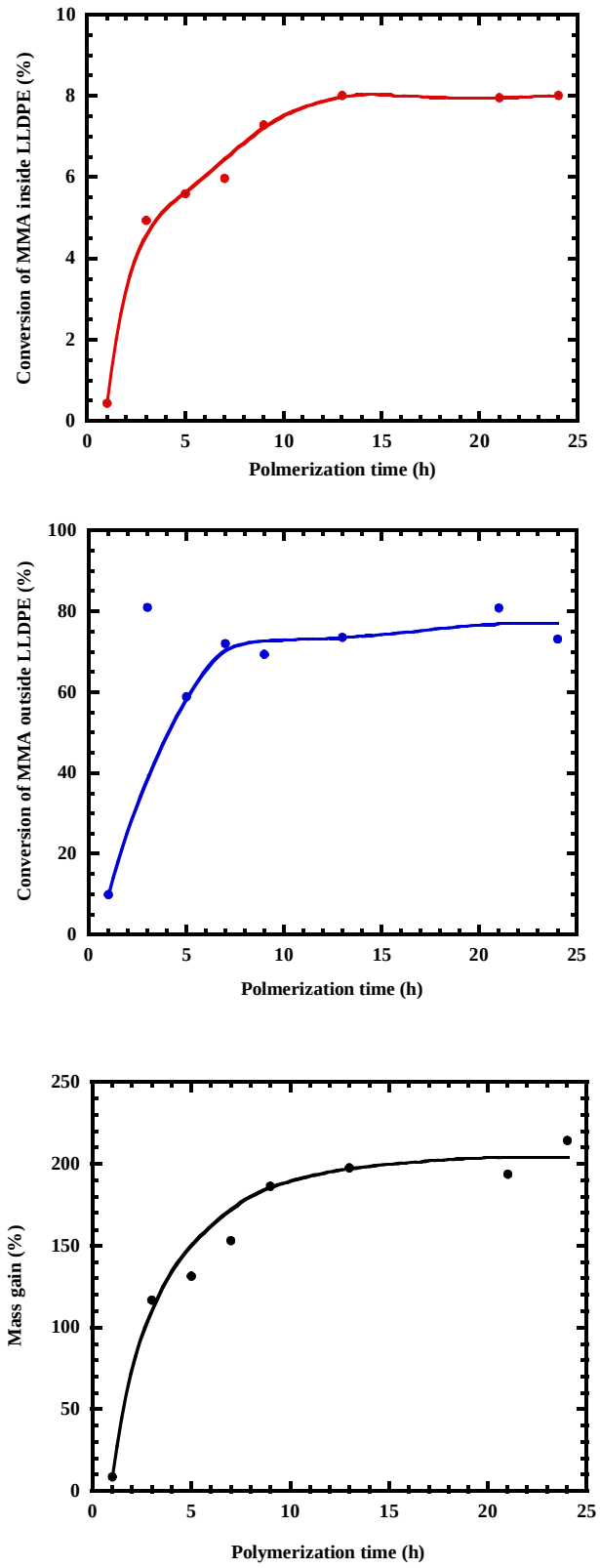

Figure 5-12 Effect of polymerization time on the mass gain of the PMMA into LLDPE and monomer conversion.

molecular weight of PMMA produced inside LLDPE is higher than that produced outside LLDPE. Although similar results were obtained in the literature and our paper [13,18], there is no explanation until now. We investigated the effect of polymerization time on the mass gain of PMMA and monomer conversion (initial pressure is 6MPa). The results were shown in figure 5-12. An obvious mass gain by successive addition was observed until 13 h, and then it remained almost constant. Consistent with this, the conversion of MMA produced inside LLDPE reached a constant value of about 8 % at 13 h. However, the amount of the conversion of MMA produced outside LLDPE reached the constant value at 7 h, a time shorter than that outside LLDPE. This maybe is because the cessation reaction outside LLDPE is rapid.

Figure 5-13 shows GPC curves of PMMA inside and outside LLDPE. Two peaks are observed in the molecular weight of PMMA produced outside LLDPE. Further, with increases in polymerization, the left peak gradually weakened, and the right peak gradually increased. This phenomenon is related to abnormal properties of PMMA in $scCO_2$ [19]. In the primary stage of polymerization, thousands of molecular weight of PMMA corresponding to the left peak is considered to be generated. Because of its insolubility in $scCO_2$, it precipitates out from $scCO_2$. Then unpolymerized MMA is impregnated into the amorphous region of PMMA, and polymerized in narrow regions. In the narrow region, because the mobility of MMA radicals is lowered by the entanglement of amorphous chain,

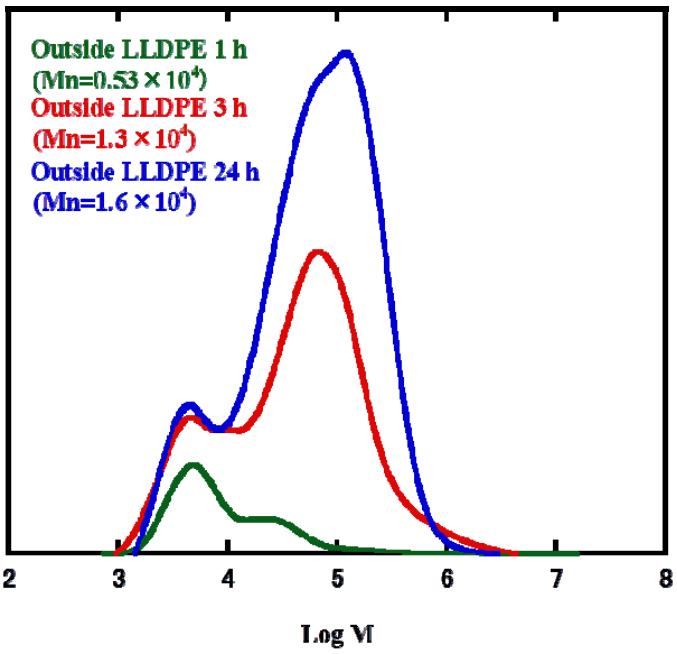

a. Outside LLDPE

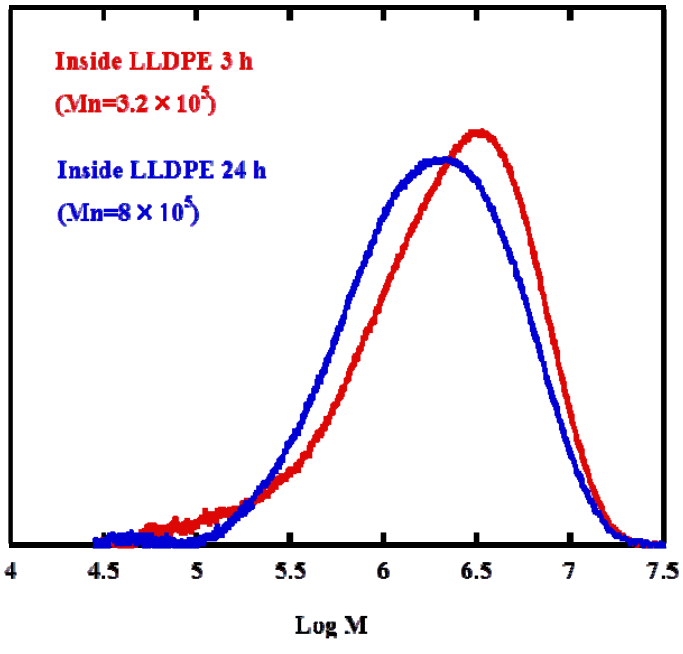

b. Inside LLDPE

Figure 5-13 Effect of polymerization time on the mass gain of the PMMA into LLDPE and monomer conversion.

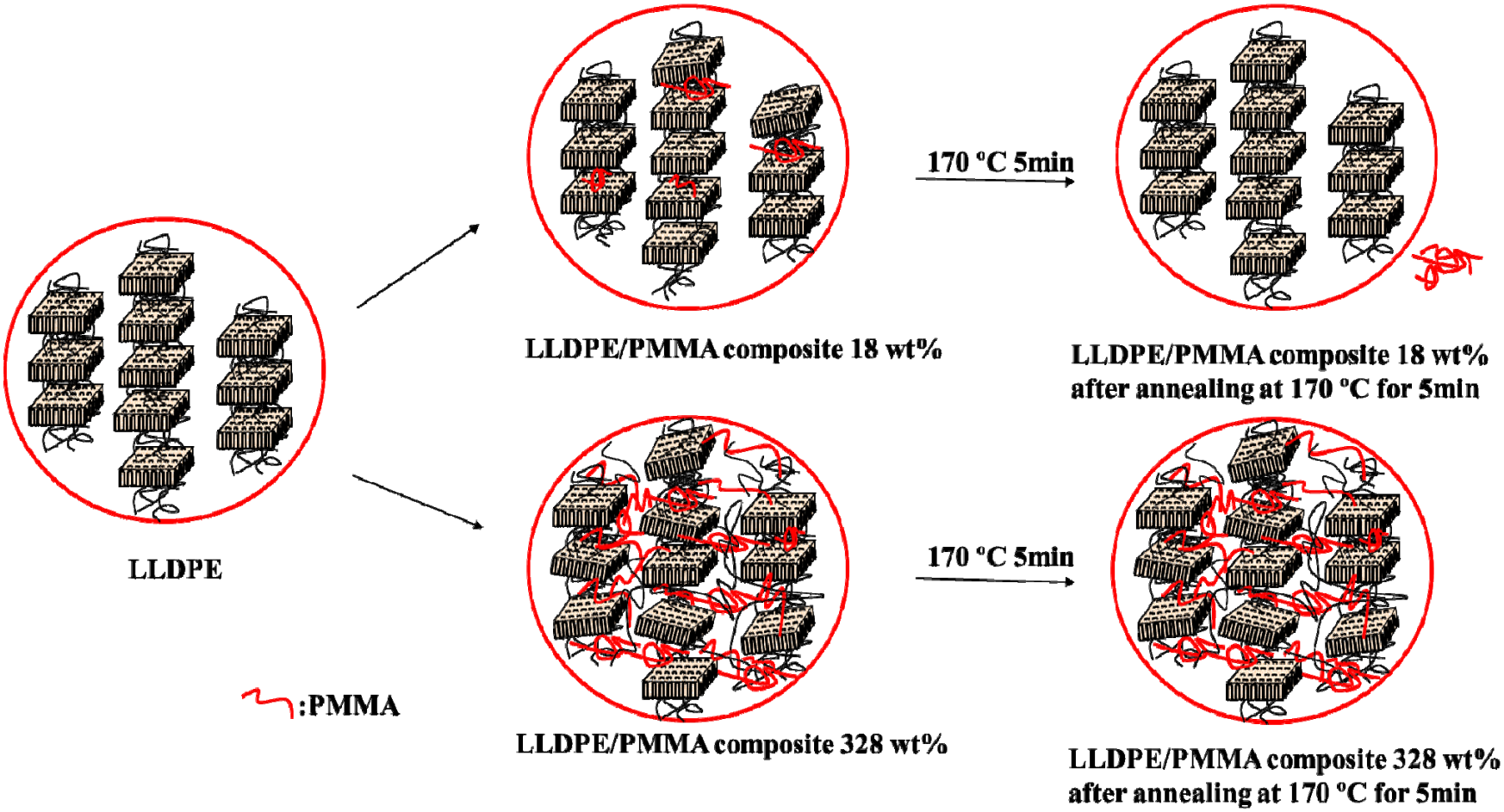

Figure 5-14 The forming mechanism of LLDPE/PMMA pseudo-IPNs.

the cessation reaction is prevented so that the PMMA of relatively high molecular weight is generated. As regards PMMA inside LLDPE, it was polymerized in a much narrower region. Therefore, the hundreds of thousands of molecular weight and only one peak is observed in figure 5-13b.

On the basis of the above results, the mechanism for the formation of pseudo-IPNs is shown in Figure 5-14. In LLDPE/PMMA composites with a low mass gain, the generated PMMA is dispersed in the amorphous region of LLDPE. When annealed at temperatures higher than $T_{m,LLDPE}$, the PMMA migrates by diffusion from the amorphous region of LLDPE and pseudo-IPNs are not formed. In LLDPE/PMMA composites with a high mass gain, the generated PMMA forms a new successive phase and entangles with the amorphous chain of LLDPE. This structure is not easily broken when annealed at temperatures higher than $T_{m,LLDPE}$, and therefore pseudo-IPNs are formed. It should be pointed out that there is no distinct boundary between low and high mass gain. Pseudo-IPNs are gradually formed with increasing mass gain of PMMA.

5.4 Conclusions

In summary, we have demonstrated that LLDPE/PMMA pseudo-IPNs with nanometer dispersion can be prepared in $scCO_2$. These pseudo-IPNs are formed by the complicated entanglement of the amorphous chain of LLDPE and PMMA chains. Since the formation of pseudo-IPNs structures restricts the movement of the LLDPE and PMMA chains, this composite retains a high storage modulus at temperatures beyond the LLDPE melting transition. It was also demonstrated that PMMA generated in the amorphous region of iPP did not affect its crystallinity, and the mechanical properties such as storage modulus, yield stress, fracture stress and strain can be controlled through controlling the mass gain of PMMA.

5.5 References

[1] Z. M. Liu, J. Q. Wang, G. Y. Yang, B. X. Han, *Chin. Chem. Lett.* 2002, **9**, 683.

[2] D. Li, Z. Liu, B. Han, L. Song, G. Yang, T. Jiang, *Polymer* 2002, **43**, 5363.

[3] A. Naylor, P. S. Timashev, A. B. Soloveva, N. A. Erina, S. Kotova, A. J. Busby, V. K. Popov, S. M. Howdle, *Adv. Mater.* 2008, **20**, 575

[4] H. Zhao, B. Huang, *Macromol. Chem. Phys.* 1998, **199**, 307.

[5] H. Zhao, T. Tang, Z. Wang, B. Huang, *J. Appl. Polym. Sci.* 1999, **71**, 967.

[6] T. Hoang, N. V. Giang, *Polym-Plast Technol.* 2004, **43**, 121.

[7] L. N. Nikitin, E. E. Said-Galiyev, R. A. Vinokur, A. R. Khokholov, M. O. Gallyamov, K. Schaumburg, *Macromolecules* 2002, **35**, 934.

[8] Royer, J. R.; DeSimone, J. M.; Khan, S. A. *Macromolecules* 1999, **32**, 8965.

[9] S. M. Sirard, K. J. Ziegler, I. C. Sanchez, P. F. Green, K. P. Johnston, *Macromolecules* 2002, **35**, 1928.

[10] J. M. Desimone, Z. Guan, C. S. Elsbernd, *Science* 1992, **257**, 945.

[11] Z. Guan, J. R. Combes, Y. Z. Menceloglu, J. M. DeSimone, *Macromolecules* 1993, **26**, 2663.

[12] T. Sawaguchi, Y. Muroga, H. Ishikawa, T. Hoshi, T. Hagiwara, S. Yano, *Kobunshi Ronbunshu* 2005, **62**, 251.

[13] R. Zhu, T. Hoshi, Y. Chishima, Y. Muroga, T. Hagiwara, S. Yano, T. Sawaguchi, *Macromolecules* 2011, **44**, 6103.

[14] A. J. Ryan, W. Bras, G. R. Mant, G. E. Derbyshire, *Polymer* 1994, **35**, 4537.

[15] A. J. Ryan, J. L. Stanford, W. Bras, T. M. W. Nye, *Polymer* 1997, **38**, 759.

[16] T. Hoshi, T. Sawaguchi, R. Matsuno, T. Konno, M. Takai, K. Ishihara, *J. of supercrotical fluids*, 2008, **44**, 391.

[17] A. U. Leszek, in Polymer Alloys and Blends, ed. by Hanser: New York, 1989, p 4.

[18] E. Kung, A. J. Lesser, T. J. McCarthy, *Macromolecules* 1998, **31**, 4160.

[19] S. M. Sirard, K. J. Ziegler, I. C. Sanchez, P. F. Green, K. P. Johnston, *Macromolecules* 2002, **35**, 1928.

Chapter 6

Preparation of Linear Low-Density Polyethylene/Polydimethylsiloxane Composite using Supercritical Carbon Dioxide

Table of Contents

Chapter 6

Preparation of Linear Low-Density Polyethylene/Polydimethylsiloxane Composite using Supercritical Carbon Dioxide

6.1. Introduction

Linear low-density polyethylene (LLDPE) is considered to be the most important class of thermoplastics among all polymers known thus far because of its low cost, good processability, and wide range of technical properties. Therefore, it is the most widely used polymer. However, LLDPE has a few disadvantages such as low surface energy, lack of chemical functionalities, difficulty in dyeing, and poor compatibility with synthetic polar polymers. Moreover, when a polymer composite of LLDPE and other polymers is prepared, phase separation occurs, and a macro domain structure is formed because of the crystal growth of LLDPE from the melt or soluble state [1]. Because of the stress concentration of the interface of this macro domain, only poor mechanical characteristics can be expected. It is very difficult to realize an improvement in the surface properties of LLDPE.

Polydimethylsiloxane (PDMS) is an inorganic polymer possessing excellent thermal stability, dielectric properties, and excellent flame retardant. It is also widely known for its extremely low glass transition temperature, flexibility and its hydrophobic surface properties [2-5]. These properties of PDMS make it suitable for use in different industries [6-10]. Blending LLDPE and PDMS should allow new and useful polymer products that should possess specific properties from the base polymers to be fabricated.

Several studies have been reported on the phase behavior of LLDPE/PDMS composites

[11,12]. These studies reported that LLDPE and PDMS are immiscible due to structural dissimilarity, lack of specific interaction and the difference between their surface energies. Kiran et al. prepared a LLDPE/PDMS composite by direct impregnation and blending of LLDPE and PDMS in $scCO_2$ [13]. However, this method is limited by the molecular weight of PDMS, and requires high temperatures and pressures. In this study, we prepared a LLDPE/PDMS composite using $scCO_2$ to obtain LLDPE with a highly hydrophobic surface. The microstructure and mechanical properties of this composite were evaluated. We also studied relationship between wettability and the structure of LLDPE/PDMS polymer composite. Thus, the LLDPE/PDMS composite can be applied to some fields, particularly in the biological field. For example, it can replace PDMS and become one of biochip materials. Not only the cost is reduced, but also mechanical properties of biochip could be expected.

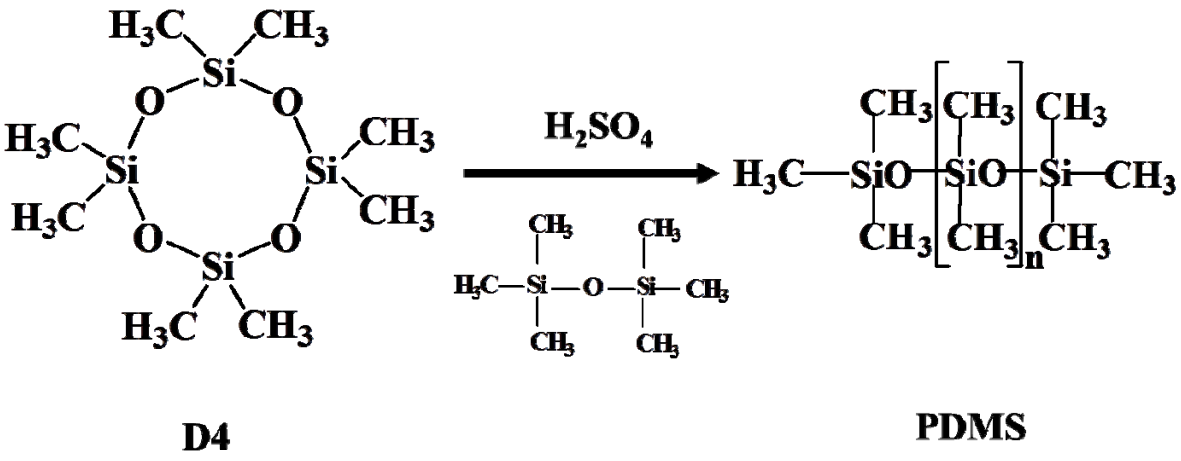

Figure 6-1 Synthetic scheme for preparation of PDMS.

The details of the preparation of LLDPE/PDMS composite are reported here. PDMS was prepared by octamethylcyclotetrasiloxane (D4). Figure 6-1 shows synthetic scheme for preparation of PDMS. This reaction belongs to cationic polymerization because of the presence of H_2SO_4 [14]. The amount of added of hexamethyldisiloxane can control the molecular weight of PDMS. The monomer (D4) was impregnated into the LLDPE substrate by $scCO_2$ and polymerized in situ in $scCO_2$. Surface properties and depth analysis of LLDPE/PDMS composite were evaluated by X-ray photoelectron spectroscopy (XPS), attenuated total reflection Fourier-transform infrared spectroscopy (ATR-FTIR), scanning electron microscope-energy dispersive X-ray (SEM-EDX), and static contact angle measurement. The microstructure and mechanical properties of LLDPE/PDMS composite were investigated by small-angle X-ray scattering (SAXS), wide-angle X-ray diffraction (WXRD), differential scanning calorimetry (DSC), dynamic viscoelastic measurements, and tensile tests.

6.2 Experimental

The LLDPE substrate, D4 (5g), hexamethyldisiloxane (0.006g) as a chain transfer agent, and sulfuric acid (0.013mL) as an initiator were placed in the vessel and sealed [15]. Air in the vessel was replaced by CO_2 at atmospheric pressure. After the system reached thermal equilibrium (35°C), the vessel was pressurized upto a CO_2 pressure of 6.0 MPa by using a CO_2 delivery pump (Model SCF-Get, JASCO Co.). The LLDPE substrate was soaked in sub-critical CO_2 for 1 h. Then the vessel was repressurized upto 6.0 MPa, and heated to the reaction temperature (80°C) for a given time. After the completion of the reaction, the vessel was cooled to 10ºC in an ice bath and gradually released to ambient pressure. The LLDPE/PDMS polymer composite was dried in vacuo at room temperature after extraction with chloroform for 24 h at 50ºC to remove unreacted reagents and the PDMS generated on the surface of the LLDPE/PDMS composite by using a Soxhlet extractor.

6.3 Results and discussion

6.3.1 Preparation of LLDPE/PDMS composite in $scCO_2$

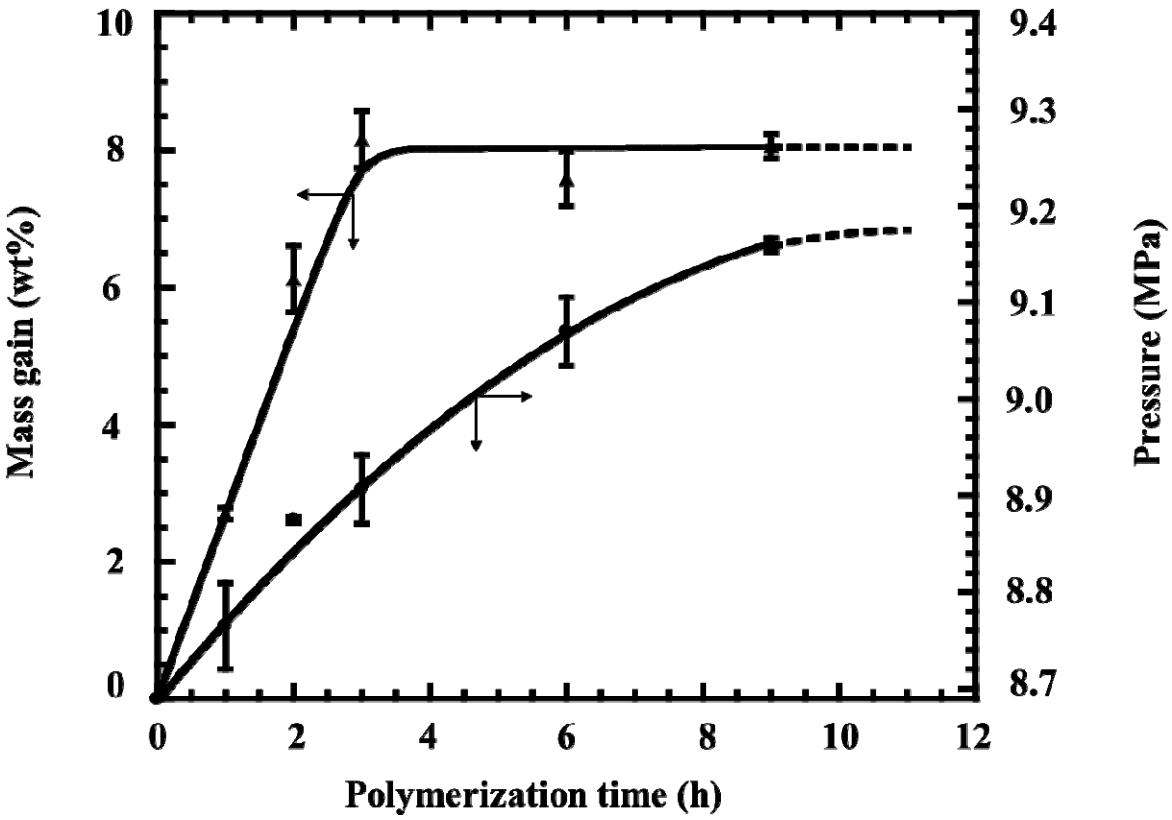

Figure 6-2 Effect of polymerization time on mass gain of PDMS into LLDPE substrate and the pressure after polymerization (triangles: mass gain; circles : pressure).

Figure 6-2 shows the effect of polymerization time on the percentage mass gain of PDMS in the LLDPE substrate and the pressure after polymerization. As expected, an obvious mass gain by successive addition was observed until 3 h, and then it remains

almost constant. Under these conditions (P < 10 MPa, T=80 °C), PDMS does not dissolve in $scCO_2$ [16,17]. When PDMS is generated on the exterior of the LLDPE substrate, the pressure increases so that the volume of the gas phase in the vessel decreases. The polymerization process can be divided into three stages. In the primary stage of polymerization (polymerization time < 3 h), the mass gain and pressure increase with polymerization time. Therefore, PDMS was polymerized both in the interior and exterior of the LLDPE substrate. The formation mechanism of the LLDPE/PDMS polymer composite is thought to be as follows: the monomer and initiator dissolve in $scCO_2$ and impregnate the amorphous interlamellar regions of the LLDPE substrate; after reaching the polymerization temperature, the monomer polymerizes within the amorphous interlamellar regions of the LLDPE substrate. Polymerization of the monomer leads to an imbalance in the partition coefficient of the monomer within and outside the LLDPE substrate. The monomer outside the LLDPE substrate then permeates into the amorphous regions of the LLDPE substrate, and polymerization continues. As a result, LLDPE and PDMS were effectively blended at the nanometer level. In the secondary stage (3 h < polymerization time < 10 h), only the pressure increases as polymerization progresses. Therefore, PDMS is only polymerized outside the LLDPE substrate. A possible reason for PDMS not being polymerized in the interior of the LLDPE substrate is that the PDMS formed on the surface of the LLDPE substrate prevents impregnation of the monomer and initiator. In the third

stage (polymerization time > 10 h), the mass gain and pressure do not increase with polymerization time. This indicates that polymerization is complete.

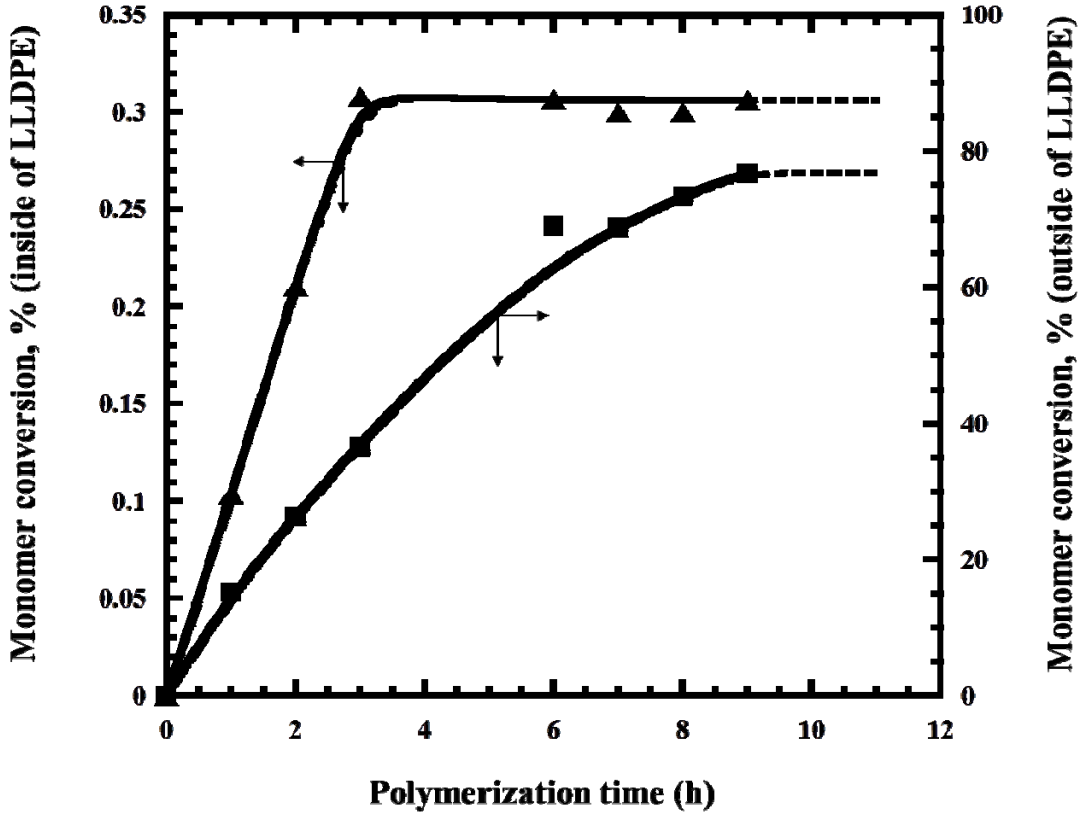

Figure 6-3 Effect of polymerization time on the monomer conversion inside and outside of LLDPE. (triangles: inside of LLDPE; circles : outside of LLDPE).

Figure 6-3 shows the effect of polymerization time on monomer conversion inside and outside LLDPE. Monomer conversion inside the LLDPE substrate increases initially and reaches a plateau after 3 h, while monomer conversion outside LLDPE becomes saturated after 10 h. This is consistent with the polymerization process being divided into three stages.

It is necessary to increase the mass gain of PDMS because it affects mechanical properties such as storage and Young's moduli, fracture stress and strain (described in section 6.3.3.3). To increase the mass gain, the amount of monomer inside the LLDPE substrate should be increased. This could be realized by changing the initial pressure or soaking time. It is considered that increasing the initial pressure will increase the solubility of the monomer in $scCO_2$ [18,19]. The amount of impregnated low-molecular weight components also depends on the soaking time, where an equilibrium value is obtained after a certain time [20]. The soaking time results in an equilibrium of the monomer concentration inside and outside the LLDPE substrate. Thus, the concentration of polymer in the substrate can be further enhanced by changing the initial pressure and soaking time.

In addition, the impregnation of $scCO_2$ starts on the surface of the substrate and then gradually progresses to the inner substrate. The role of $scCO_2$ is then to dissolve D4 and H_2SO_4 and to carry the monomer and initiator into the amorphous regions of the LLDPE substrate. The swelling kinetics of CO_2 in the polymer matrix depend on the temperature and pressure [21,22]. Therefore, controlling the penetration depth of PDMS can be achieved by controlling the diffusion and solubility of $scCO_2$ according to temperature and pressure.

6.3.2 Surface properties and depth analysis of LLDPE/PDMS composite

6.3.2.1 Surface analysis of LLDPE/PDMS polymer composite

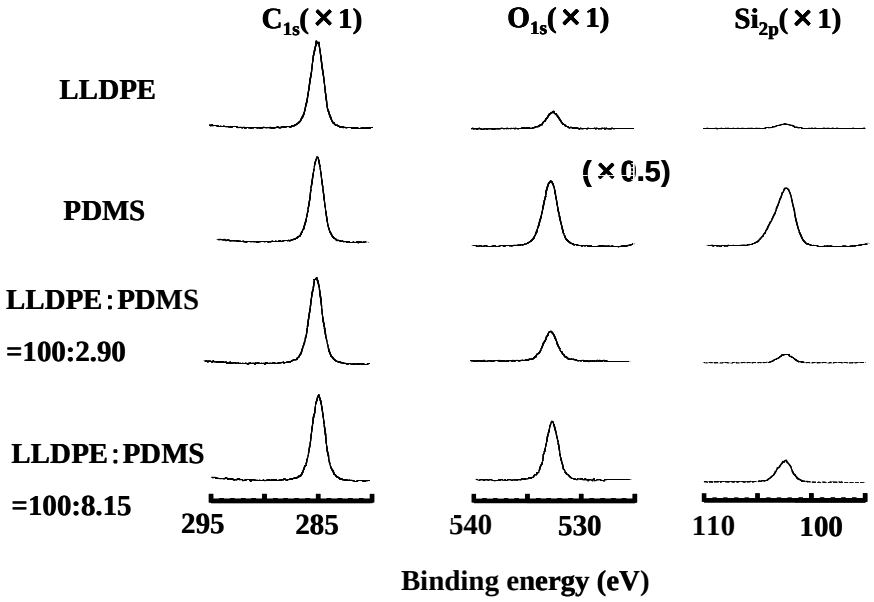

Figure 6-4 XPS charts of LLDPE, PDMS, and LLDPE/PDMS polymer composites. (Take-off angle is 90º)

Figure 6-4 shows the XPS diagrams of LLDPE, PDMS, and LLDPE/PDMS composites. In the case of LLDPE, a strong intensity is observed at 285 eV. This is attributed to the carbon atoms in the ethylene chain. In addition, two small peaks are observed at 533 and 102 eV. These peaks are attributed to the oxygen atoms and they may

arise from the oxidation or contamination of LLDPE. In PDMS, three strong peaks are observed at 285, 533, and 102 eV. These are attributed to the constituent atoms in the PDMS chain. In the LLDPE/PDMS polymer composite, except for the carbon peak of LLDPE, the strength of the oxygen and silicon peaks increases. Further, it increases with the mass gain of the LLDPE/PDMS polymer composite (this is more evident in Figure 6-6). It can be concluded that PDMS prepared by cationic polymerization was generated in the vicinity of the surface.

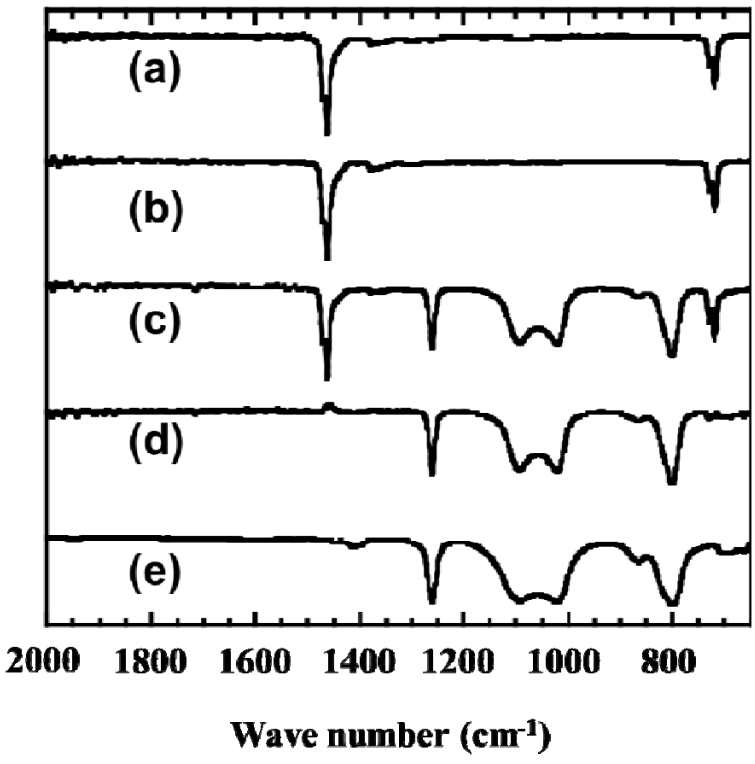

Figure 6-5 ATR-FTIR spectra of (a) original LLDPE substrate, (b) LLDPE treated with $scCO_2$, (c) LLDPE/PDMS polymer composite with a mass gain of 8.15%, (d) differential spectrum ((LLDPE/PDMS polymer blend)-(LLDPE)), and (e) PDMS.

Fig. 6-5 shows the ATR-FTIR spectra. (a) shows the spectrum of the original LLDPE substrate. (b) shows the spectrum of the LLDPE treated with $scCO_2$. It can be seen that they are almost identical. This implies that $scCO_2$ does not affect the chemical structure of LLDPE during the course of swelling [23]. (c) shows the spectrum of the LLDPE/PDMS polymer composite with a mass gain of 8.15 wt%. New peaks are observed at 800, 1021, 1093 and 1261 cm^{-1}. They are attributed to PDMS. (d) shows the differential spectrum ((PE/PDMS polymer blend)-(PE)). (e) shows the spectrum of PDMS. As expected, the differential spectrum almost corresponds to the spectrum of PDMS. The spectra confirm that PDMS was formed within the LLDPE substrate.

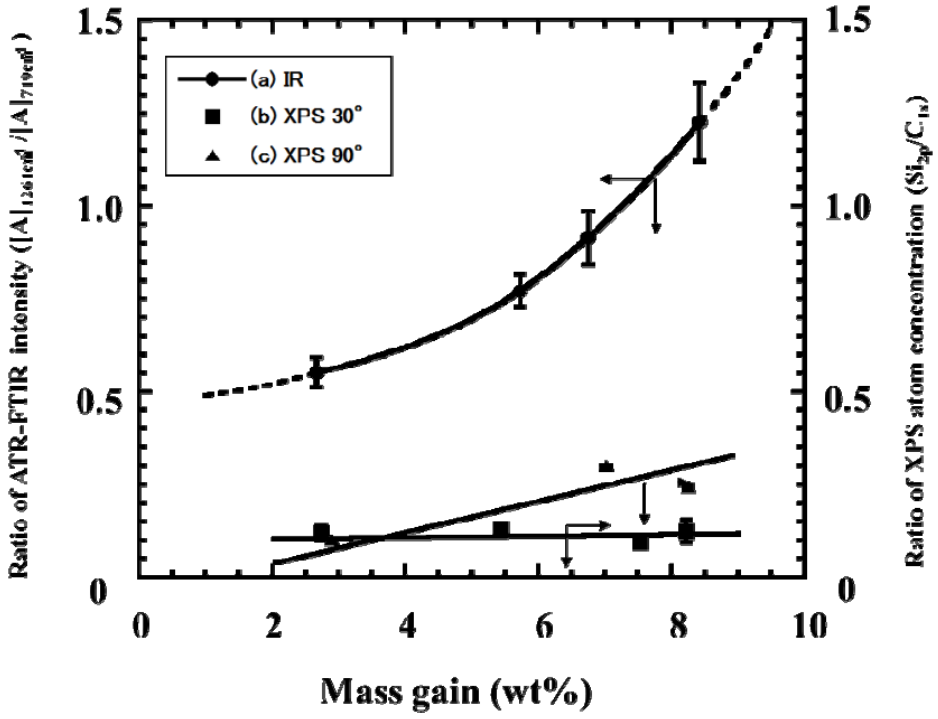

Figure 6-6 (a) Relationship between the ratio of ATR-FTIR intensities at 1261 cm^{-1} to 719 $cm^{-1}$and the mass gain of PDMS. (b) and (c) Relationship between the ratio of XPS atom concentration of silicon to carbon and the mass gain of PDMS.

In Figure 6-6, (a) shows the relationship between the ratio of ATR-FTIR intensities at 1261 cm^{-1} to 719 cm^{-1} ($[A]_{1261cm}^{-1}/[A]_{719cm}^{-1}$) and the mass gain of PDMS. The ATR-FTIR absorption at 719 cm^{-1} ($[A]_{719cm}^{-1}$) can be attributed to the methylene chain in the LLDPE substrate. The new absorption at 1261cm^{-1} ($[A]_{1261cm}^{-1}$) can be attributed to the Si-CH_3 bond in PDMS. Further, the intensity increased with the mass gain of PDMS. (b) and (c) show the relationship between the ratio of the XPS atom concentration of silicon to carbon (Si_{2p}/C_{1s}) and the mass gain of PDMS. The take-off angles of the photoelectron for each atom of (b) and (c) were 30° and 90°, respectively. In (b), the value of Si_{2p}/C_{1s} is almost constant. This implies that the amount of PDMS in the topmost surface is almost constant. Overall, the value of Si_{2p}/C_{1s} in (c) is larger than that in (b). The variation trends of curves are different in (a), (b), and (c). This can be attributed to the different measurement depths of IR and XPS (30° and 90°). These results imply that the PDMS near the surface could be controlled by the mass gain of PDMS, namely the polymerization time.

SEM-EDX analysis provides further evidence that PDMS is generated in the LLDPE substrate. The mapping micrographs detected by EDX analysis show an accumulation of silicon and carbon in the LLDPE/PDMS polymer composite. The silicon concentration confirms the strong presence of PDMS. Thus, in Figure 6-7, in the case of small mass gain (2.86 wt%), PDMS exists near surface of the LLDPE substrate. In the case of large mass gain (8.97 wt%), PDMS exists within and near surface of the LLDPE substrate, and the

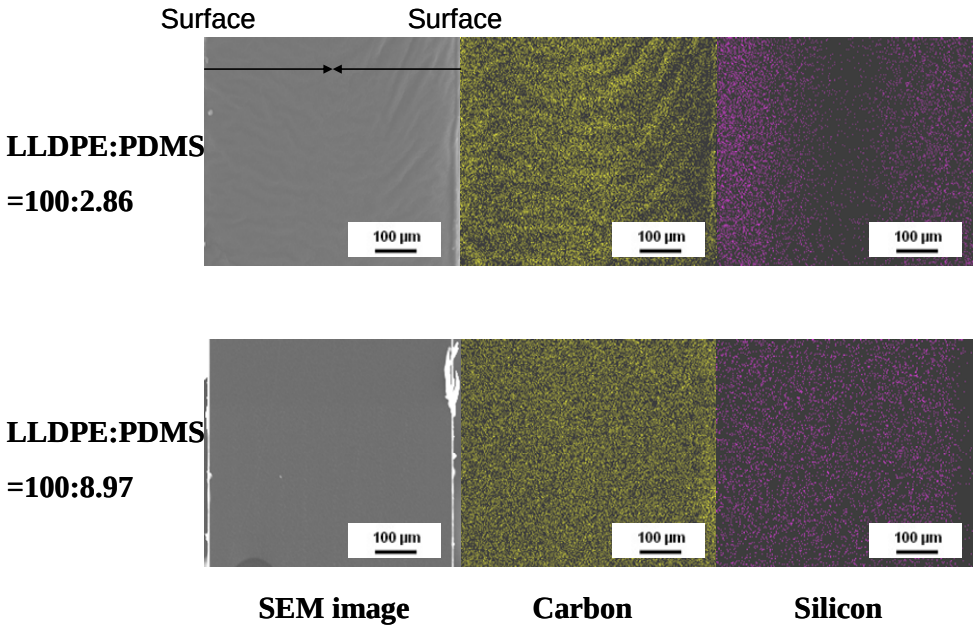

Figure 6-7 SEM micrographs of cross section of the LLDPE/PDMS composite and EDX mapping of C and Si present in the cross section of the composite.

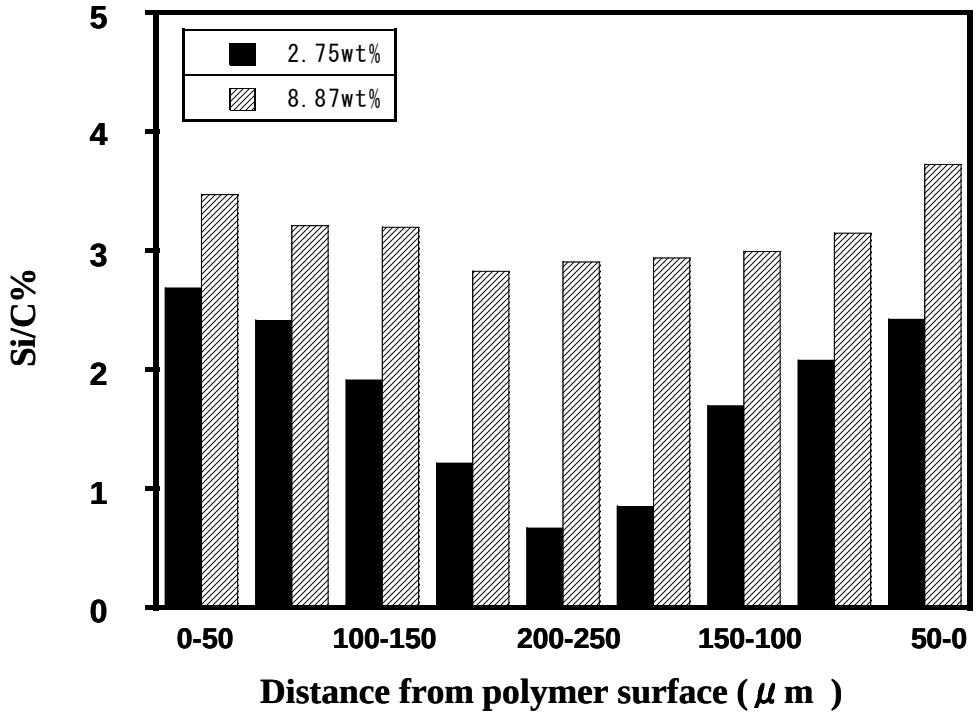

Figure 6-8 Si concentration, detected by EDX analysis, in the cross section of LLDPE/PDMS composites (mass gain: 2.75 wt% and 8.87 wt%).

LLDPE/PDMS composite approaches a uniform structure. This is more obvious in Figure 6-8. Figure 6-8 shows the relationship between the ratio of the EDX atom concentration of silicon to carbon (Si/C) and the distance from the polymer surface of LLDPE/PDMS. It is evident that relative to the surface (0–50 μm), the value of Si/C is very small in the 200-250 μm region in the case of small mass gain (2.75 wt%); however, it does not change much in the case of large mass gain (8.87 wt%). This indicates that the result shown in Figure 6-7 is correct. Structure control in the depth direction is possible depending on the control of the mass gain, that is, the polymerization time.

6.3.2.2 Surface properties of LLDPE/PDMS composite

Figure 6-9 shows the static contact angle of all the specimens. These photos were obtained by using a normal digital camera. The contact angles can be observed intuitively from these photos. For surfaces with comparable structures, a relatively high contact angle value generally implies high hydrophobicity. In table 6-1, the value of the LLDPE/PDMS polymer composite is larger than that of LLDPE, less than that of PDMS, and almost constant with changing the mass gain of PDMS. This is because only the PDMS that is at a depth of 0.2–3 nm affects the hydrophobicity [24]. These results imply that the

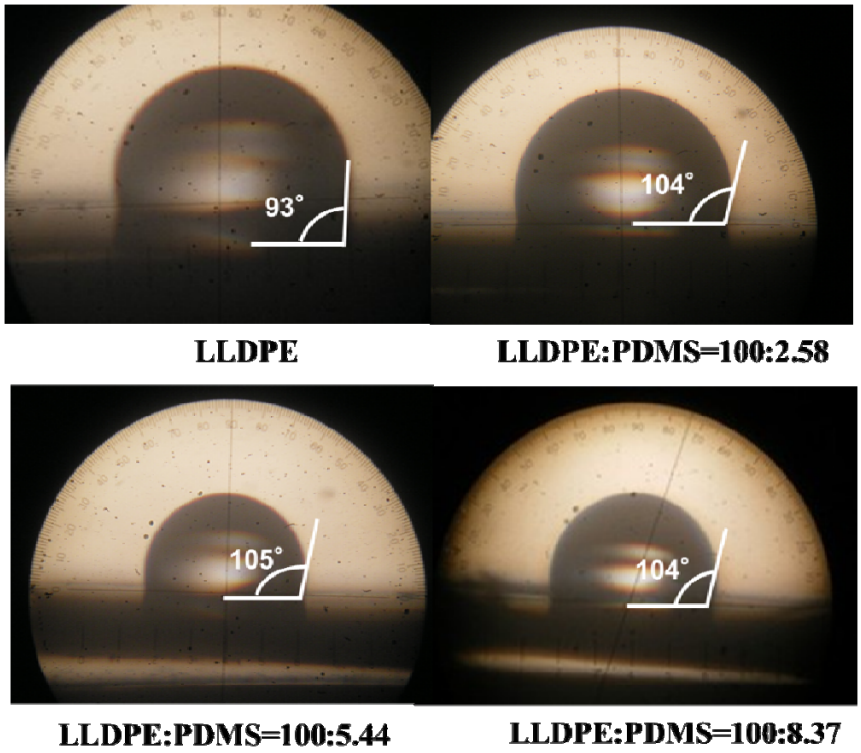

Figure 6-9 Pictures of static contact angle measurements of the surface of LLDPE and LLDPE/PDMS composites.

Table 6-1 Results of static contact angle measurements of LLDPE, PDMS and LLDPE/PDMS composites.

Sample	Run1	Run2	Run3	Average
LLDPE	95	94	94	94
PDMS	——	——	——	117 [25]
LLDPE:PDMS=100:2.58	104	102	105	104
LLDPE:PDMS=100:5.44	105	105	105	105
LLDPE:PDMS=100:8.37	104	101	106	105

hydrophobicity of LLDPE has been improved. It should be noted that the hydrophobicity of LLDPE has been improved greatly when the mass gain of PDMS generated in the surface of LLDPE is small (2.58 wt%).

6.3.3 Microstructure and mechanical properties of LLDPE/PDMS composite

6.3.3.1. Characterization of LLDPE/PDMS composite

Figure 6-10 shows WXRD patterns of the original LLDPE, LLDPE treated with $scCO_2$, and LLDPE/PDMS composites, which exhibit characteristic peaks of the (110) and (200) planes. The angular positions of the diffraction peaks of crystalline LLDPE are almost identical in original LLDPE, LLDPE treated with $scCO_2$, and LLDPE/PDMS composites, indicating that the crystal forms do not change upon $scCO_2$ treatment or addition of PDMS. However, the amorphous region of the LLDPE/PDMS composite increases as the mass gain of PDMS increases, which indicates that the overall crystallinity decreases as the mass gain of PDMS increases (Figure 6-11). The reduction in sample crystallinity is caused by dilution as a result of formation of PDMS in the amorphous regions of LLDPE and the

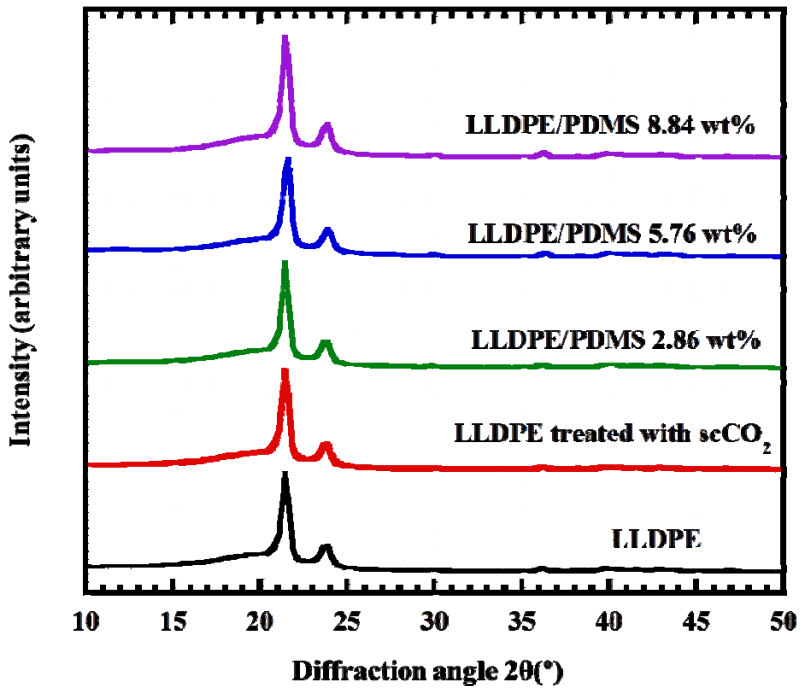

Figure 6-10 WAXD patterns of original LLDPE, LLDPE treated with $scCO_2$ and LLDPE/PDMS composites.

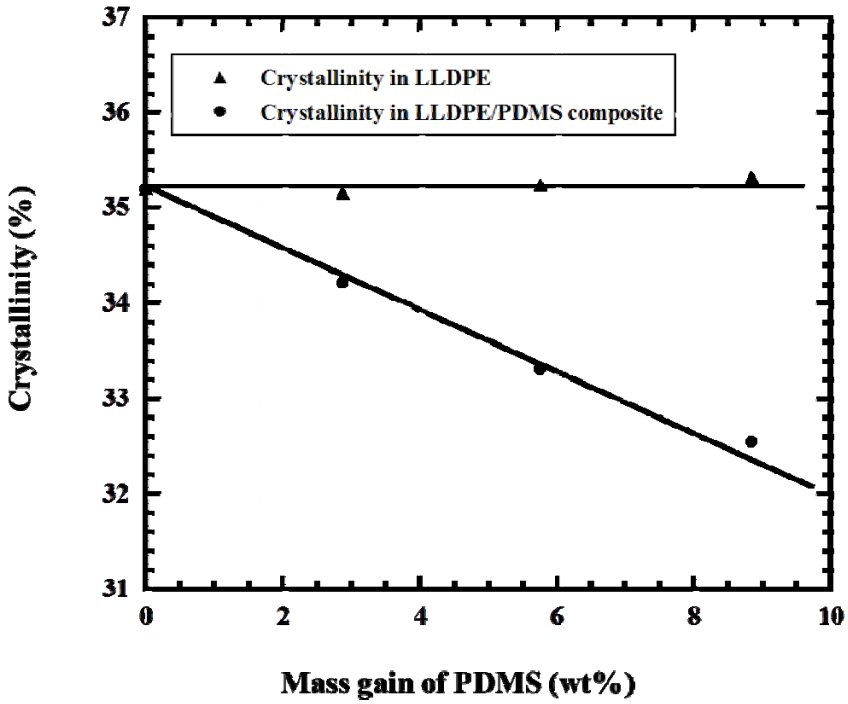

Figure 6-11 Relationship between crystallinity and mass gain of PDMS.

resultant increase in the size of these regions. The percentage crystallinity in LLDPE, X_{LLDPE}, was calculated as follows:

$$X_{LLDPE}\ (\%) = \frac{X_{LLDPE/PDMS}}{W_{LLDPE}} \qquad (6\text{-}1)$$

where X_{LLDPE} is the crystallinity of LLDPE/PDMS composite that is assumed to be dependent only on the crystalline regions of LLDPE, $X_{LLDPE/PDMS}$ is the crystallinity of the entire LLDPE/PDMS composite, and W_{LLDPE} is the weight fraction of LLDPE. X_{LLDPE} does not change although $X_{LLDPE/PDMS}$ decreases as the mass gain of PDMS increases. The total amount of crystalline LLDPE remains unchanged. These results indicate that D4 polymerizes solely within the amorphous regions of LLDPE.

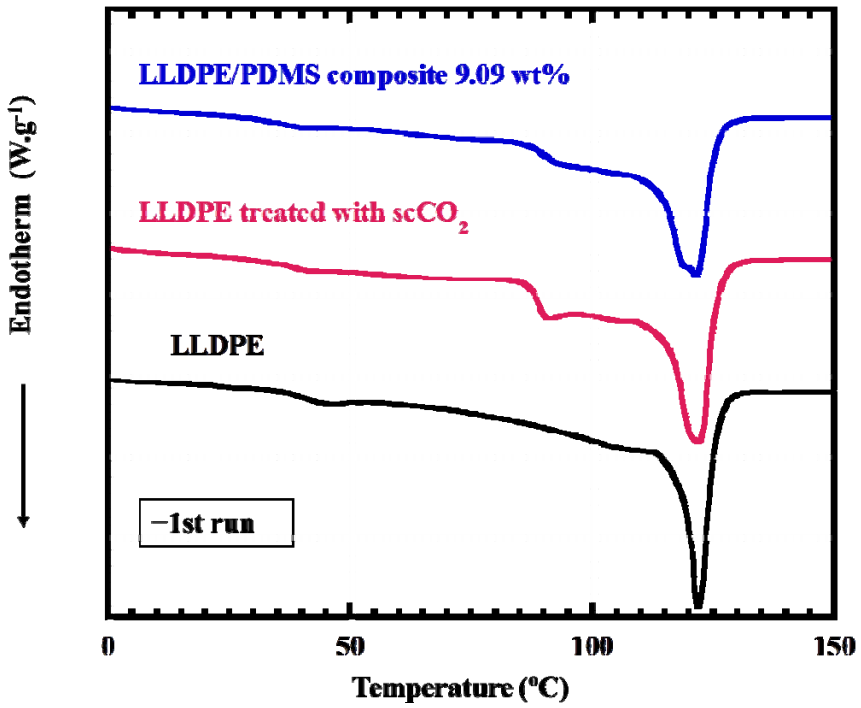

Figure 6-12 DSC thermograms of LLDPE, LLDPE treated with $scCO_2$,and LLDPE/PDMS composite (mass gain: 9.09 wt%).

Figure 6-12 shows DSC thermograms of the original LLDPE, LLDPE treated with $scCO_2$, and LLDPE/PDMS composite with a mass gain of 9.09 wt%. The DSC thermogram of LLDPE treated with $scCO_2$ changed without increasing the degree of crystallinity compared with the original LLDPE. This result implies that the swelling of $scCO_2$ at a treatment temperature of 80 °C produces the same effect as isothermal crystallization [26]. In the LLDPE/PDMS composite, a strong LLDPE melting endotherm was observed. The melting endotherm reveals that the composite does not affect the crystalline region of the LLDPE substrate. The degree of crystallinity of the original LLDPE and LLDPE/PDMS composite was found to be 35.2 and 32.5 wt%, respectively. The reduction in sample crystallinity is entirely because of dilution by the addition of PDMS to the amorphous LLDPE regions. The total amount of crystalline region of LLDPE remained unchanged. In addition, it was found that the DSC traces of the LLDPE treated with $scCO_2$ and LLDPE/PDMS composite exhibited a second low T_m endothermic peak as well as from the main crystalline melting peak. This means that small crystals were present in the LLDPE treated with $scCO_2$ and LLDPE/PDMS composite.

6.3.3.2 Microstructural analysis of the LLDPE/PDMS composite

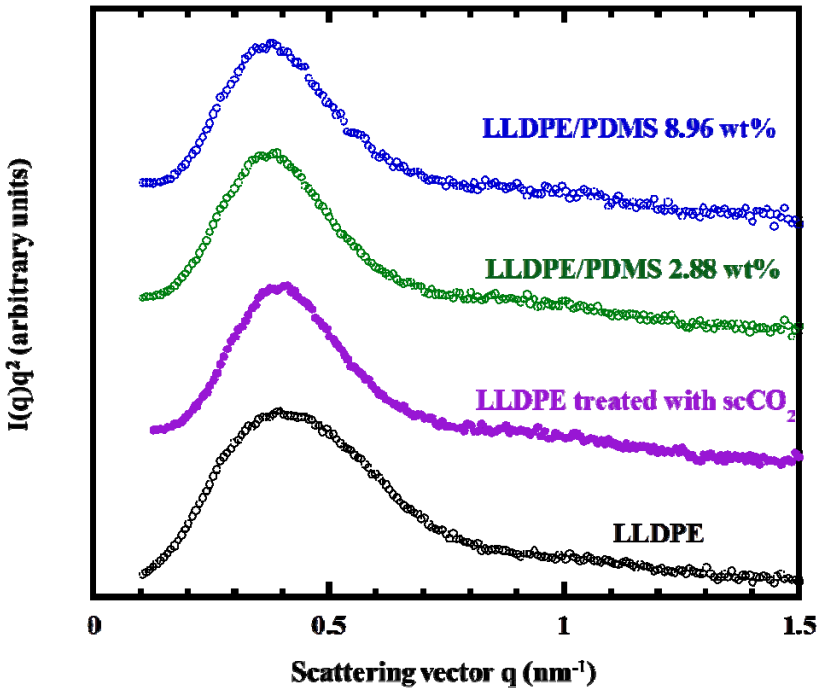

Figure 6-13 Lorentz-corrected SAXS plofiles of original LLDPE, LLDPE treated with $scCO_2$, and LLDPE/PDMS composites.

The effect of formation of PDMS in the amorphous regions of the LLDPE substrate on its microstructure was investigated by SAXS. Figure 6-13 shows the Lorentz-corrected SAXS profiles of original LLDPE, LLDPE treated with $scCO_2$, and LLDPE/PDMS composites. In the spectrum of original LLDPE, the scattering vector q of the peak top was 0.397 nm^{-1} (calculated using a Bragg spacing of 15.8 nm). This peak was caused by the long period of the lamellar structure [27,28]. The positions of the peak in the LLDPE treated with $scCO_2$ was the same as that in the original LLDPE. However, the peak of the LLDPE treated with $scCO_2$ was sharper. This implies that a small crystal of LLDPE grew,

which is consistent with the DSC results. In the LLDPE/PDMS composite, the peak from long period shifted slightly toward lower q. This change was not observed for the CO_2-treated LLDPE. The extent of this change depended on the mass gain of PDMS. This result is consistent with the generation of small-angle scattering from extensive disruption of the crystalline lamellar upon incorporation of PDMS into the polymer composites. The results of DSC and WAXD measurements indicate that the total amount of crystalline region of LLDPE and the crystal structure of LLDPE do not change. Therefore, these SAXS measurements indicate that PDMS formed in the amorphous regions between the crystalline lamellar of LLDPE, and that LLDPE and PDMS were blended at the nanometer level.

6.3.3.3 Mechanical properties

The dynamic viscoelastic behavior of LLDPE and the LLDPE/PDMS composites is represented as a function of temperature in Figure 6-14. At a lower temperature than the glass transition temperature of PDMS ($T_{g,\mathrm{PDMS}}$) at ~123 °C [29], the storage modulus of the LLDPE/PDMS composite was larger than that of LLDPE. Furthermore, at temperatures

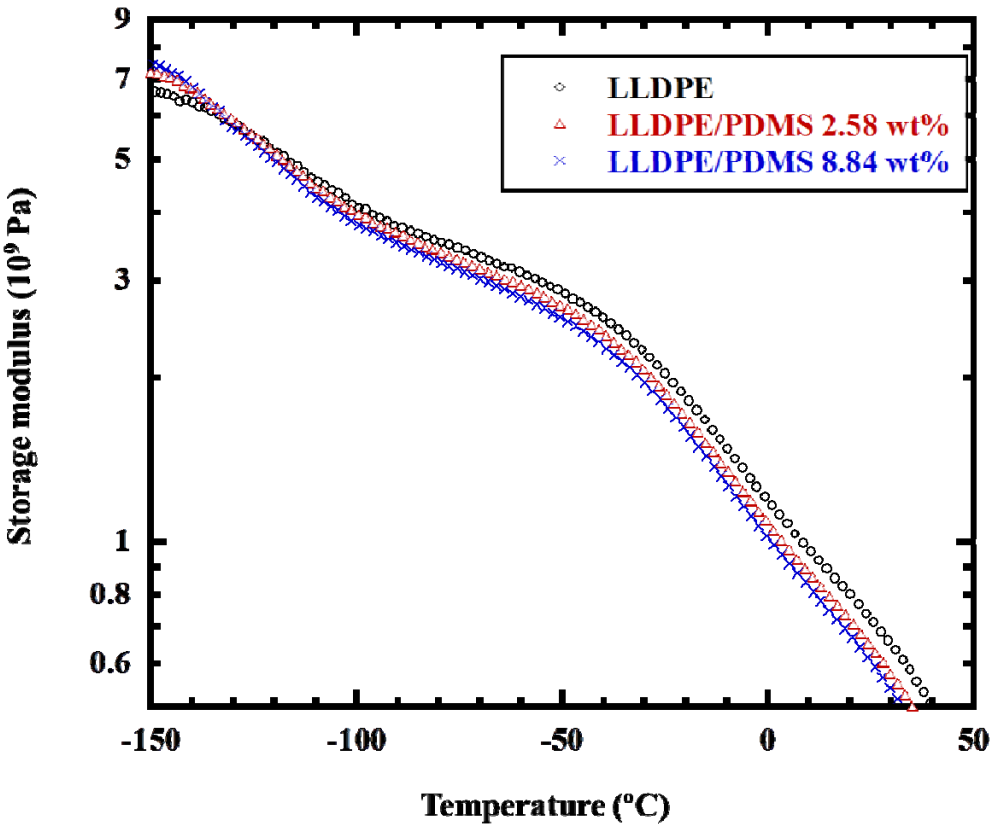

Figure 6-14 Temperature dispersion curves of the storage modulus (E') for original LLDPE and LLDPE/PDMS composites.

Table 6-2 Results of tensile tests at 20 ºC.

Sample name	Young's modulus (MPa)	Fracture stress (MPa)	Fracture strain (%)
LLDPE	130	9.0	922
LLDPE/PDMS (5.76 wt%)	70	7.6	836
LLDPE /PDMS (8.84 wt%)	57	5.6	738

higher than $T_{g,PDMS}$, the storage modulus of the LLDPE/PDMS composite was smaller than that of LLDPE. This change in the storage modulus of the LLDPE/PDMS composite depends on the mass gain. This occurs because, at temperatures lower than $T_{g,PDMS}$, the chain mobility of the amorphous regions of LLDPE is retarded by the glassy PDMS that is generated in the amorphous regions. The decreased mobility of the amorphous LLDPE chains increases the storage modulus of the LLDPE/PDMS composite so that is larger than that of LLDPE. Above $T_{g,PDMS}$, the amorphous regions of the LLDPE/PDMS composite increase more than that of LLDPE because of the micro-Brownian motion of PDMS.

Table 6-2 lists the results of tensile testing at 20 °C above $T_{g,PDMS}$. Because the amorphous regions of the LLDPE/PDMS composite increase more than that of PE because of the micro-Brownian motion of PDMS at 20 °C, the Young's modulus, fracture stress and strain of the LLDPE/PDMS composite decrease as the mass gain of PDMS increases. This is consistent with the results of DVA. Therefore, the nanometer-sized PDMS generated in the amorphous regions significantly affects the mechanical properties of the LLDPE/PDMS composite, which can be controlled through the mass gain of PDMS.

6.4 Conclusion

We have succeeded in obtaining a LLDPE/PDMS composite by in situ cationic polymerization using $scCO_2$. PDMS formed in the amorphous regions between the crystalline lamellar of LLDPE, which did not affect its crystallinity. LLDPE and PDMS were blended at the nanometer level. Further, the depth to which PDMS was excited in the LLDPE substrate was analyzed by XPS, IR and SEM-EDX, in order to control the structure of the LLDPE/PDMS polymer composite by varying the polymerization time. The hydrophobicity of LLDPE has been improved. Surface modification of LLDPE could be realized. The presence of PDMS in the amorphous regions significantly affects the viscoelasticity and mechanical properties of the LLDPE/PDMS composite. The storage modulus of the LLDPE/PDMS composite changes at $T_{g,\mathrm{PDMS}}$. Below $T_{g,\mathrm{PDMS}}$, the chain mobility of the amorphous regions of LLDPE is retarded by the glassy PDMS, and the storage modulus of the LLDPE/PDMS composite is larger than that of LLDPE. Above $T_{g,\mathrm{PDMS}}$, the amorphous regions of the LLDPE/PDMS composite increase more than that of LLDPE because of the micro-Brownian motion of PDMS, so the storage modulus of the LLDPE/PDMS composite is smaller than that of LLDPE. Mechanical properties such as Young's modulus, tensile strength and elongation at break of the LLDPE/PDMS composite can be controlled by the mass gain of PDMS.

6.5 References

[1] Akiyama, S., Inoue, T. & Nishi, T. *Polymer blend* 56-59, (CMC Publishing Co., Ltd., Japan, 1981).

[2] J. Riffle, I. Yilgor, A. Banthia, G. Wilkes, J. McGrath, *Organic Coatings Applied Polymer Science Proceedings* 1981, **46**, 397.

[3] I. Yilgor, Jr WP. Steckle, E. Yilgor, R. Freelin, J. Riffle, *Journal of Polymer Science, Part A Polymer Chemistry* 1989, **27,** 3673.

[4] S. Garin, L. Lecamp, B. Youssef, C. Bunel, *Eur. Polym. J.* 1999, **35**, 473.

[5] S. Hou, Y. Chung, C. Chan, P. Kuo, *Polymer* 2000, **41,** 3263.

[6] R. Qi, Y. Wang, J. Li, C. Zhao, S. Zhu, *Journal of Membrane Science* 2006, **280**, 545.

[7] C. Luo, F. Meng, A. Francis, *Microelectronics Journal* 2006, **37**, 1036.

[8] R. Lehmann, J. Miller, G. Kozerski, *Chemosphere* 2000, **41**, 743.

[9] B. Jo, L. Van, M. Linda, K. Motsegood, D. Beebe, *Journal of microelectromechanical Systems* 2000, **9**, 76.

[10] K. Polmanteer, H. Chapman, M. Lutz, *Rubber Chem. Technol.* 1985, **58**, 965.

[11] A. Chalykh, N. Avdeyev, *Polymer Science U.S.S.R.* 1985, **27**, 2769.

[12] M. Huglin, I. Idris, Eur. Polym. J. 1985, 21, 9.

[13] Z. Bayraktar, E. Kiran, *J. Supercrit. Fluid* 2008, 44, 48.

[14] X. Yang, C. Yao, *J. Appl. Polym. Sci.* 2007, **106**, 3600.

[15] J. Zhang, A. Busby, C. Roberts, X. Chen, M. Davies, S. Tendler, S. M. Howdle, *Macromolecules* 2002, 35, 8869.

[16] Z. Bayraktar, K. Erdpgan, *J. Appl. Polyme. Sci.* 2000, **75**, 1397.

[17] Y. Xiong, E. Kiran, *Polymer* 1995, **36**, 4817.

[18] C. F. Kirby, M. A. McHugh, *Chem. Rev.* 1999, **99**, 565.

[19] Y. Sato, K. Fujiwara, T. Takikawa, Sumarno, S. Takishima, H. Masuoka, *Fluid Phase Equilib.* 1999, **162**, 261.

[20] L. R. Berens, G. S. Huvard, R. W. Korsmeyer, F. W. Kunig, *J. Appl. Polym. Sci.* 1992, **46**, 231.

[21] D. Li, Z. Liu, B. Han, L. Song, G. Yang, T. Jiang, *Polymer* 2002, **43**, 5363.

[22] D. Li, B. Han, Z. Liu, *Macromol. Chem. Phys.* 2001, **202**, 2187.

[23] L. N. Nikitin, E. E. Said-Galiyev, R. A. Vinokur, A. R. Khokholov, M. O. Gallyamov, K. Schaumburg, *Macromolecules* 2002, **35**, 934.

[24] J. R. Royer, J. M. DeSimone, S. A. Khan, *Macromolecules* 1999, **32**, 8965.

[25] J. Seo, L. P. Lee, *Sensors and Actuators B* 2006, **119**, 192.

[26] P. Schouterden, G. Groeninckx, B. Heijden, F. Jansen, *Polymer* 1987, **28**, 2099.

[27] A. J. Ryan, W. Bras, G. R. Mant, G. E. Derbyshire, *Polymer* 1994, **35**, 4537.

[28] A. J. Ryan, J. L. Stanford, W. Bras, T. M. W. Nye, *Polymer* 1997, **38**, 759.

[29] A. Tiwari, A. K. Nema, C. K. Das, S. K. Nema, *Thermochimica Acta* 2004, **417**, 133.

Chapter 7

Concluding Remarks

Concluding Remarks

The purpose of this thesis work is to prepare novel nanocomposites and control their bulk and surface properties. In the new preparation method for nanocomposites using supercritical carbon dioxide ($scCO_2$), three kinds of novel semicrystalline/amorphous polymer nanocomposites were obtained by changing the kind of polyolefins and blending polymers. Also, the relationship among the experimental parameters (initial pressure and polymerization time), constituent contents of polymer composites (mass gain of amorphous polymer), and properties (microstructure, physical properties, and surface properties) was studied to control material characteristics.

In **Chapter 3,** a composite comprised of isotactic polypropylene (iPP) and poly(methyl methacrylate) (PMMA) was prepared by in situ radical polymerization of methyl methacrylate (MMA) using $scCO_2$. The connection of initial pressure, mass gain of PMMA, and microstructure and mechanical properties was created. The mass gain initially increased in correlation with the initial pressure, reaching a maximum of 109 wt% when the initial pressure of CO_2 was about 9 MPa, and then decreased with further increases in the initial pressure. iPP and PMMA were blended at the nanometer scale. PMMA did not affect the crystallinity, the enthalpy of melting the iPP crystal, nor the top temperature of the iPP crystal melting, but it did reduce the starting temperature at which the iPP crystal started melting. The mechanical properties of the composites: storage modulus, yield stress,

fracture stress and strain, were determined to depend on the mass gain of PMMA.

In **Chapter 4**, the thermal stability of iPP/PMMA composites was evaluated. When the iPP/PMMA composites were annealed at 140 °C, although iPP crystal grew, the nano-structure ~~can be~~ remained. When the iPP/PMMA composites were annealed at 190 °C, PMMA migrated by diffusion from the amorphous region of iPP, then macroscopic domain structure was formed, and the nanostructure could not be remain.

In **Chapter 5**, the linear low-density polyethylene (LLDPE)/PMMA polymer nanometer-dispersed and having pseudo-interpenetrating networks (pseudo-IPNs) were prepared using $scCO_2$. As in the case of iPP/PMMA composite, the connection of initial pressure, mass gain of PMMA, and microstructure and mechanical properties was created. The mass gain initially increased in correlation with the initial pressure, reaching a maximum of 450 wt% when the initial pressure of CO_2 was about 7 MPa, and then decreased with further increases in the initial pressure. The pseudo-IPNs were formed by the complicated entanglement of the amorphous chain of LLDPE and PMMA chains through controlling the mass gain of PMMA. LLDPE and PMMA were blended at the nanometer level. They were also somewhat thermodynamically miscible. The structure of LLDPE/PMMA composite with a high mass gain was not easily broken when annealed at temperatures higher than crystal melting temperature of LLDPE ($T_{m,LLDPE}$). High storage moduli remained at temperatures beyond the LLDPE melting transition. Further, the extent

of the storage modulus can be controlled through controlling the mass gain of PMMA.

In **Chapter 6**, a composite comprising LLDPE and polydimethylsiloxane (PDMS) was prepared by in situ cationic polymerization of octamethylcyclotetrasiloxane (D4) using $scCO_2$. The connection of polymerization time, mass gain of PDMS, and microstructure, mechanical properties, and surface properties was created. LLDPE and PDMS were blended at the nanometer level. The depth that PDMS exists in LLDPE can be controlled by adjusting the mass gain of PMMA. The hydrophobicity of LLDPE had been improved from 94º to 105º by incorporating PDMS. Also, as the same as iPP/PMMA and LLDPE/PMMA, the microstructure and mechanical properties depend on the mass gain of PMMA.

When these three polymer nanocomposites were compared, they showed similar microstructure because of the similar preparation mechanism, that is, the monomer and initiator were dissolved in $scCO_2$ and impregnated into the amorphous interlamellar regions of semicrystalline polymer substrate. After reaching the polymerization temperature, the monomer polymerized within the amorphous interlamellar regions of semicrystalline polymer substrate. The polymerization of monomer led to the imbalance of the partition coefficient of monomer within and outside of the semicrystalline polymer substrate. The monomer outside of the semicrystalline polymer substrate thus permeated into the amorphous regions of the semicrystalline polymer substrate, and the

polymerization reaction was continuous. As a result, the semicrystalline polymer and amorphous polymer were effectively blended at the nanometer level.

However, these three polymer nanocomposites showed some differences in mechanical properties such as the formation of pseudo-IPNs. Pseudo-IPNs can be formed in LLDPE/PMMA nanocomposites with high mass gain of PMMA, and can not be formed in iPP/PMMA and LLDPE/PDMS nanocomposites. The most fundamental reason is the difference in mass gain maximum of amorphous polymer that can be reached. The mass gain maximum of PMMA was 450 wt% in LLDPE/PMMA, and was 109wt% in iPP/PMMA. The mass gain maximum of PDMS was only 9 wt%. It is considered that a larger mass gain will broaden the mechanical property changes. To increase the mass gain maximum, the experimental parameters such as the amount of monomer and initiator, initial pressure, polymerization time and temperature, impregnating time and temperature, should be considered once again.

When compared with other researches in the area of semicrystalline/amorphous polymer nanocomposites prepared in $scCO_2$ in the literature, the novelty of this research work can be concluded to lie in: (1) Three kinds of novel nanocomposites, iPP/PMMA, LLDPE/PMMA and LLDPE/PDMS, were prepared for the first time. (2) The changes in crystal melting temperature of semicrystalline polymer substrate after combining amorphous polymer were found for the first time. (3) Thermal stability of

semicrystalline/amorphous polymer nanocomposite was studied anew. (4) Pseudo-IPNs have never been prepared before using $scCO_2$.

In situ polymerization using $scCO_2$, as one of polymer blend preparation methods, has been used to prepare dozens of new nanocomposites that couldn't be obtained by conventional methods. The laboratory where the author belonged also prepared six kinds of semicrystalline/amorphous polymer nanocomposites using this method. In the opinion of the author, there remain two major questions to be answered in this area. One is the reason why the amorphous polymer generated in the interlamellar regions of semicrystalline polymer is of high molecular weight. The other is the further research about thermal stability. The former will help to further understand the in situ polymerization mechanism using $scCO_2$. The latter will make the semicrystalline/amorphous polymer nanocomposite prepared using $scCO_2$ can be used in practical production. The author expects these two problems can be solved in the future research.

Appendix

A. Abbreviation

Supercritical carbon dioxide	**$scCO_2$**
Isotactic polypropylene	**iPP**
Linear low-density polyethylene	**LLDPE**
Methyl methacrylate	**MMA**
Poly(methyl methacrylate)	**PMMA**
Octamethylcyclotetrasiloxane	**D4**
Polydimethylsiloxane	**PDMS**
Interpenetrating polymer networks	**IPNs**
Transmission electron microscopy	**TEM**
Atomic force microscopy	**AFM**
Small-angle X-ray scattering	**SAXS**
Wide-angle X-ray diffraction	**WXRD**
Differential scanning calorimetry	**DSC**
Dynamic viscoelastic analysis	**DVA**
X-ray photoelectron spectroscopy	**XPS**
Attenuated total reflection Fourier-transform infrared spectroscopy	**ATR-FTIR**
Scanning electron microscope-energy dispersive X-ray	**SEM-EDX**

B. List of Publications

1. Rui Zhu, Ryota Usui, Toru Hoshi, Yoshio Muroga, Toshiki Hagiwara, Shoichiro Yano, and Takashi Sawaguchi

   Preparation of isotactic polypropylene/polydimethylsiloxane composite using supercritical carbon dioxide

   Report of Research Institute of Science and Technology, Nihon University **2009**, 55, 36–37.

2. Rui Zhu, Toru Hoshi, Daisuke Sasaki, Ryota Usui, Toshiki Hagiwara, Shoichiro Yano, and Takashi Sawaguchi

   Surface properties and depth analysis of polyethylene/polydimethylsiloxane composite prepared by using supercritical carbon dioxide

   Polymer Journal **2010**, 42, 562–566

3. Rui Zhu, Toru Hoshi, Toshiki Hagiwara, Shoichiro Yano, and Takashi Sawaguchi

   Preparation of isotactic polypropylene/polydimethylsiloxane composite by *in situ* polymerization of octamethylcyclotetrasiloxane using supercritical carbon dioxide

   Journal of Research Institute of Science and Technology, Nihon University **2011**, 124, 7–12.

4. Toru Hoshi, Rui Zhu, and Takashi Sawaguchi

Development of novel polymer nanocomposite using supercritical carbon dioxide

Material Science and Technology **2011**, 48, 21–25.

5. Rui Zhu, Toru Hoshi, Yoshihiro Chishima, Yoshio Muroga, Toshiki Hagiwara, Shoichiro Yano, and Takashi Sawaguchi

Microstructure and mechanical properties of polypropylene/poly(methyl methacrylate) nanocomposite prepared using supercritical carbon dioxide

Macromolecules **2011**, 44, 6103–6112.

6. Rui Zhu, Toru Hoshi, Yoshio Muroga, Toshiki Hagiwara, Shoichiro Yano, and Takashi Sawaguchi

Preparation of nanometer dispersed semicrystalline/amorphous polymer pseudo-interpenetrating network using supercritical carbon dioxide as a swelling agent

Chemistry Letters **2012**, 41, No.9, 996–998.

7. Rui Zhu, Toru Hoshi, Yoshio Muroga, Toshiki Hagiwara, Shoichiro Yano, and Takashi Sawaguchi

Microstructure and mechanical properties of a polyethylene/polydimethylsiloxane

composite prepared using supercritical carbon dioxide

Journal of Applied Polymer Science **2013**, 127, 3388–3394.

8. Takashi Sawaguchi, Rui Zhu, and Toru Hoshi

In-situ polymerization of MMA in supercritical carbon dioxide

Organic synthensis in new solvent. Eds. S&T Publishing: Tokyo, **2013**, 155–169.

9. Tsuyoshi Tadano, Rui Zhu, Yoshio Muroga, Toru Hoshi, Daisuke Sasaki, Shoichiro Yano, and Takashi Sawaguchi

A New Mechanism for the Silica Nanoparticle Dispersion-Agglomeration Transition in a Poly(methyl methacrylate)/Silica Hybrid Suspension

Polymer Journal, in press.

10. Tsuyoshi Tadano, Rui Zhu, Yoshio Muroga, Toru Hoshi, Daisuke Sasaki, Shoichiro Yano, and Takashi Sawaguchi

Molecular Weight Dependence of SiO_2 Nanoparticle Agglomeration Behavior in Monodisperse PMMA/SiO_2 Hybrid Suspension

Chemistry Letters, in press.

11. Tsuyoshi Tadano, Rui Zhu, Yoshio Muroga, Toru Hoshi, Daisuke Sasaki, Shoichiro

Yano, and Takashi Sawaguchi

Feature of Novel Transparent Poly(methyl methacrylate)/Nano-Silica Particle Hybrid Film Prepared on Basis of Entanglement-Agglomeration Transition Mechanism

Submitted to Macromolecules.

C. List of Presentations

1. Rui Zhu, Ryota Usui, Toru Hoshi, Yoshio Muroga, Toshiki Hagiwara, Shoichiro Yano, and Takashi Sawaguchi

   Preparation of isotactic polypropylene/polydimethylsiloxane composite using supercritical carbon dioxide

   Joint Symposium between College of Science and Technology, Nihon University and University of Minnesota

   Sep. 19, **2008**, Nihon University, Tokyo, Japan (Oral presentation)

2. Rui Zhu, Ryota Usui, Toru Hoshi, Yoshio Muroga, Toshiki Hagiwara, Shoichiro Yano, and Takashi Sawaguchi

   Surface hydrophobizing of isotactic polypropylene by cationic polymerization of polydimethylsiloxane using supercritical carbon dioxide

   The 89th CSJ Spring Conference

   Mar. 27 – 31, **2009**, Nihon University, Chiba, Japan (Poster presentation)

3. Rui Zhu, Ryota Usui, Toru Hoshi, Yoshio Muroga, Toshiki Hagiwara, Shoichiro Yano, and Takashi Sawaguchi

Surface hydrophobicity of polyethylene by cationic polymerization of polydimethylsiloxane using supercritical carbon dioxide

The 58th SPSJ Symposium on Macromolecules

Sep. 16 – 18, **2009**, Kumamoto University, Kumamoto, Japan (Poster presentation)

4**.** Rui Zhu, Ryota Usui,Toru Hoshi,Toshiki Hagiwara, Shoichiro Yano, and Takashi Sawaguchi

Surface modification of polyolefins by incompatible polymers using supercritical carbon dioxide

The 53rd CST Academic Meeting of Nihon University

Nov. 28, **2009**, Nihon University, Tokyo, Japan (Oral presentation)

5. Rui Zhu, Toru Hoshi, Daisuke Sasaki, Toshiki Hagiwara, and Takashi Sawaguchi

Surface hydrophobicity of polyethylene by cationic polymerization of octamethylcylotetrasiloxane using supercritical carbon dioxide

The 75th SCEJ Annual Meeting

Mar. 18 – 20, **2010**, Kagoshima University, Kagoshima, Japan (Oral presentation)

6. Rui Zhu, Ryota Usui, Toru Hoshi, Yoshio Muroga, Toshiki Hagiwara, and Takashi

Sawaguchi

Preparation of isotactic polypropylene/poly(methyl methacrylate) composite using supercritical carbon dioxide and its thermal stability

The 59th SPSJ Annual Meeting

May. 26 – 28, **2010**, Pacifico Yokohama, Yokohama, Japan (Poster presentation)

7. Rui Zhu, Ryota Usui, Toru Hoshi, Yoshio Muroga, Toshiki Hagiwara, and Takashi Sawaguchi

Preparation and thermal stability of isotactic polypropylene/poly(methyl methacrylate) composite using supercritical carbon dioxide

The 42nd SCEJ Autumn Meeting

Sep. 6 – 8, **2010**, Doshisha University, Kyoto, Japan (Oral presentation)

8. Rui Zhu, Toru Hoshi, Toshiki Hagiwara, Yoshio Muroga, Shoichiro Yano, Takashi Sawaguchi

Microstructure and mechanical properties of isotactic polypropylene/ploy (methyl methacrylate) nanocomposite prepared using supercritical carbon dioxide

The 54th CST Academic Meeting of Nihon University

Nov. 27, **2010**, Nihon University, Tokyo, Japan (Oral presentation)

9. Rui Zhu, Toru Hoshi, Yoshio Muroga, Toshiki Hagiwara, Shoichiro Yano, and Takashi Sawaguchi

Microstructure and physical properties of isotactic polypropylene/poly (methyl methacrylate) nanocomposite prepared using supercritical carbon dioxide

The 60th SPSJ Annual Meeting

May. 25 – 27, **2011**, Osaka International Convention Center, Osaka, Japan (Poster presentation)

10. Rui Zhu, Kazaya Ssto, Junichi Uchida, Toru Hoshi, Yoshio Muroga, Toshiki Hagiwara, and Takashi Sawaguchi

Thermal stability of isotactic polypropylene/poly(methyl methacrylate) composite prepared by supercritical carbon dioxide

The 60th SPSJ Symposium on Macromolecules

Sep. 28 – 30, **2011**, Okayama University, Okayama, Japan (Poster presentation)

11. Rui Zhu, Kazaya Ssto, Junichi Uchida, Toru Hoshi, Yoshio Muroga, Toshiki Hagiwara, and Takashi Sawaguchi

Preparation of polyolefin/poly(methyl methacrylate) pseudo-iPNs by complicated

entanglement in supercritical carbon dioxide

The 55th CST Academic Meeting of Nihon University

Nov. 26, **2011**, Nihon University, Tokyo, Japan (Oral presentation)

12. Rui Zhu, Toru Hoshi, Yoshio Muroga, Toshiki Hagiwara, Shoichiro Yano, and Takashi Sawaguchi

Preparation of isotactic polypropylene/poly(methyl methacrylate) composite using supercritical carbon dioxide

The 9th SPSJ International Polymer Conference

Dec. 11 – 14, **2012**, Kobe International Convention Center, Kobe, Japan (Poster presentation)

13. Rui Zhu, Toru Hoshi, Yoshio Muroga, Toshiki Hagiwara, and Takashi Sawaguchi

Annealing effect on microstructure and physical properties of iPP/PMMA composite prepared using supercritical carbon dioxide

The 62nd SPSJ Symposium on Macromolecules

Sep. 11 – 13, **2013**, Kanazawa University, Kanazawa, Japan (Poster presentation)

Acknowledgment

The present doctorial dissertation is the compilation of the works carried out at Department of Materials and Applied Chemistry, Graduate School of Science and Technology, Nihon University from Apr. 2011 to Mar. 2014.

First and foremost, I would like to express the deepest gratitude and great respect to Professor Dr. Takashi Sawaguchi for giving me valuable advice and granting a favor to me. Also, I would like to thank my excellent supervisors, Assistant Professor Dr. Toru Hoshi and Associate Professor Dr. Toshiki Hagiwara. Especially, Assistant Professor Dr. Hoshi gave me valuable discussions and ingoing suggestions that helped me advance my thesis.

I would like to express great thanks to Professor Dr. Hiizu Iwamura, Professor Dr. Masahiro Kakugo, and Professor Dr. Shigeru Shimizu for reviewing my thesis and their precious advice.

I would like to express great thanks to Professor Dr. Shoichiro Yano, Associate Professor Dr. Yoshio Muroga, and Dr. Daisuke Sasaki, for their helpful advice and discussion.

I would like to thank all members of Sawaguchi laboratory, Mr. Ryota Usui, Mr. Hibiki Shimamoto, Mr. Kazuya Sato, Ms. Xia Huang, Mr. Junichi Uchida, Mr. Koji Kobayashi, Mr. Shota Suzuki, and Mr. Yusuke Nakanishi. I spent a happy and exciting student life

thanks to everybody.

I would like to express my deepest gratefulness to my family. Especially, my father and mother. Finally, I would like to be grateful to my wife Ning Gao for her great heartfelt support.

September 2013

Rui Zhu

Department of Materials and Applied Chemistry,

Nihon University